

# **Quantum chemical investigations on adsorption processes at oxide surfaces**

Zur Erlangung des akademischen Grades eines

**DOKTORS DER NATURWISSENSCHAFTEN**

(Dr. rer. nat.)

Fakultät für Chemie und Biowissenschaften  
Karlsruher Institut für Technologie (KIT) - Universitätsbereich

genehmigte

**DISSERTATION**

von

Qiang Li

aus

Jiangsu, China

Dekan:	Prof. Dr. Willem Klopper
Referent:	PD Dr. Karin Fink
Korreferent:	Prof. Dr. Christof Wöll
Tag der mündlichen Prüfung:	23. Oktober 2015



# Contents

<b>1</b>	<b>Introduction</b>	<b>1</b>
<b>2</b>	<b>Theoretical background</b>	<b>5</b>
2.1	Density Functional Theory	6
2.1.1	The Hohenberg-Kohn Theorem	6
2.1.2	Kohn-Sham Method	7
2.1.3	Spin density functional theory	8
2.1.4	Local-Density Approximation (LDA)	9
2.1.5	Gradient Corrected and Hybrid Functionals	10
2.2	Periodic Calculations and Supercell Approach	11
2.2.1	Bloch theorem	11
2.2.2	Plane waves and Pseudopotential	12
2.2.3	Supercell Approach	15
2.2.4	On-site Correction (DFT+U)	16
2.2.5	Density of state (DOS)	17
2.3	Embedded cluster method	18
2.3.1	Periodic Fast Multipole Method (PEECM )	19
2.3.2	Evjen Procedure	20
<b>3</b>	<b>Adsorption of formic acid on the nonpolar ZnO (10-10) surface</b>	<b>22</b>
3.1	Introduction	22
3.2	Computational details	25
3.2.1	Periodic calculations	25
3.2.2	Embedded cluster calculations	27
3.3	Results and Discussion	28
3.3.1	Results of the PBC calculations	28
3.3.2	Comparison with the experimental data	31
3.3.3	Comparison of embedded cluster and plane wave calculations for the adsorption of formic acid on ZnO	33
3.4	Conclusion	42
<b>4</b>	<b>NO Adsorption on rutile TiO<sub>2</sub>(110) surface: role of oxygen vacancies</b>	<b>44</b>
4.1	Introduction	44
4.2	Computational details	46
4.2.1	Calculations with Periodic boundary condition (PBC)	46
4.2.2	Embedded Cluster calculations	47
4.2.3	Band gap and on-site correction	48
4.3	Results and discussion	49
4.3.1	Defect free surface	49
4.3.2	Modeling of oxygen vacancies	50
4.3.3	NO adsorption on the perfect surface	53
4.3.4	NO adsorption at the Vo site	54
4.3.5	NO adsorption at the Ti(5c) site	55

4.3.6	NO stretching frequency	59
4.4	Conclusion	60
<b>5</b>	<b>Applications on materials with magnetic centers</b>	<b>62</b>
5.1	CO adsorption on the Fe-terminated $\alpha$ -Fe <sub>2</sub> O <sub>3</sub> (0001) surface	62
5.1.1	Introduction	62
5.1.2	Computational details	63
5.1.3	Results and Discussion	64
5.1.4	Conclusion	71
5.2	Magnetism of inverse spinel copper ferrite: influence of Li intercalation	72
5.2.1	Introduction	72
5.2.2	Models and Methods	73
5.2.3	Results and Discussion	77
5.2.4	Conclusion	82
5.3	Dispersion Correction in MOCl(M=Fe,Bi) systems	83
5.3.1	Introduction	83
5.3.2	Theory and computational methods	83
5.3.3	Results and Discussion	84
<b>6</b>	<b>Summary</b>	<b>90</b>
<b>7</b>	<b>Bibliography</b>	<b>93</b>
<b>8</b>	<b>COPYRIGHT PERMISSIONS</b>	<b>104</b>
<b>9</b>	<b>ACKNOWLEDGEMENTS</b>	<b>106</b>

# 1 Introduction

Transition metal oxides are technologically important materials with applications in different fields. In particular in the field of catalysis, large progress has been made in understanding the fundamental processes in the last years [1]. The industrial production of methanol from syngas ( $\text{CO}/\text{CO}_2/\text{H}_2$ ) at low temperature, instead of at high temperature and high pressure, uses mainly copper/zinc oxide based catalysts [2], such as  $\text{Cu}/\text{ZnO}/\text{Al}_2\text{O}_3$  or  $\text{Cu}/\text{ZnO}/\text{Cr}_2\text{O}_3$ . A further important application of catalysis is the elimination of air contaminants, including carbon monoxide and nitrogen monoxide from car emissions [3, 4]. The oxidation of carbon or nitrogen monoxide to dioxides by transition metal oxides such as  $\text{Fe}_2\text{O}_3$  is economically feasible compared with noble metals, platinum and gold for example [5-7]. In fact, selective oxidation, ammoxidation, and selective dehydrogenation probably constitute the most important catalytic applications of transition metal oxides. Some transition metal oxides can also serve as semiconductor photo-catalysts [8]. These materials use the energy of electromagnetic radiation to promote the excitation of electrons to the conduction band where they can diffuse to the surface and participate in reduction reactions. For example, the  $\text{Au}/\text{TiO}_2$  catalysts [9], easily prepared in situ from different Au precursors and  $\text{TiO}_2$ , generate  $\text{H}_2$  from  $\text{H}_2\text{O}/\text{alcohol}$  mixtures.

Transition metal oxide materials also have applications in solar energy conversion with dye-sensitized solar cells (DSSCs). An anode of a DSSC is composed of a porous layer of wide band gap oxides (mostly  $\text{TiO}_2$  and  $\text{ZnO}$ ), covered with dye molecules that absorb sunlight. Formic acid ( $\text{HCOOH}$ ) on  $\text{ZnO}$  serves as a model system for the dye-surface contact by carboxylate groups in Grätzel-cells [10-12].

The interaction of the transition metal oxide surfaces with the chemical adsorbates is a key reaction in all of the technical applications discussed above. In this respect, not only the clean surfaces but also defects, e.g. oxygen vacancies which are common in reducible metal oxides, are of importance for the afore mentioned applications. Different types of such oxygen vacancies are known. In F-centers, the vacancy site can

be filled with 2 ( $F^0$  center), 1 ( $F^{1+}$  center) or 0 ( $F^{2+}$  center) electrons. They are directly or indirectly responsible for many of the material properties, such as optical absorption and luminescence spectra, reactivity of photo-catalysis, and conductivity [13-15]. However, the mechanisms of catalysis and solar cells are not always clear. A better understanding of surface chemistry, which deals with bonding and reaction of an adsorbate with the surface and the influence of the surface on the bonding and the reaction between adsorbates, is required.

Transition metal oxide materials are also used in rechargeable batteries. For the most common Lithium-ion batteries, spinel ferrites are commercially attractive and have gained importance due to their high specific capacities [16]. Spinel oxides retain capacity for a large number of cycles due to their robust host structure and show high lithium diffusion rates due to the presence of a three dimensional network of interstitial sites [17, 18]. An interesting feature is that the transition metal centers of these materials can change their oxidation state and magnetic properties during cycling. Thus a reversible control over bulk magnetism via electrochemical processes is proposed with spinel iron oxide, maghemite [19]. The increasing energy demands require the development of new kinds of rechargeable batteries. Recently, rechargeable chloride ion batteries based on chloride ion transfer have been proposed [20-22]. Metal oxychlorides such as  $FeOCl$  and  $BiOCl$  are used as cathode materials for chloride ion batteries, because they show higher stability and lower volumetric changes than metal chlorides during cycling. The structures and properties of the transition metal oxides or related materials can be determined by modern computational approaches, and provide guidance for design of experiments.

In this thesis, quantum chemical calculations have been performed on some of the key processes of the technologically relevant applications mentioned above. The investigations can contribute to a better understanding of the physical basics. In this context, the general features of both the bulk and the surface of the transition metal oxide materials are of interest.

The thesis is organized as follows: In chapter 2, the theoretical background of quantum chemical calculations on bulk solids and surfaces by plane wave calculations with

periodic boundary conditions as well as with embedded cluster calculations is discussed. Furthermore, the basics of density functional theory (DFT) is given, which is the method mainly used throughout this thesis.

In chapter 3, the adsorption of formic acid on the ZnO(10-10) surface is discussed. Based on the combination of DFT calculations with experimental IR data, it was possible to assign two different adsorption geometries. Additionally, the applicability of the two approaches for the calculations of vibrational frequencies is analyzed. The convergence of the results with different parameters of the methods was investigated.

In Chapter 4, the influence of oxygen vacancies on the adsorption of NO on the rutile TiO<sub>2</sub>(110) surface is investigated. For the surface with bridging oxygen vacancies, the electronic structure, in particular the localization of the excess electrons, is still under discussion. For four different distributions of the two excess electrons the influence on the adsorption properties of NO such as adsorption energies and vibrational frequencies is investigated.

Chapter 5 contains three applications of plane wave calculations on materials with magnetic centers. For bulk iron oxide, the adsorption of CO on the Fe-terminated  $\alpha$ -Fe<sub>2</sub>O<sub>3</sub>(0001) surface is investigated. The anti-ferromagnetic ground state is taken into account by spin polarized DFT. In the second application, the influence of reversible Li-intercalation in CuFe<sub>2</sub>O<sub>4</sub> on the magnetic properties of the material is calculated. The exchange coupling constants between the magnetic centers are obtained within the broken symmetry approach for the pure and Li-intercalated compound. Thus the reduction of the total magnetic moments is explained. The third application concerns weak interactions between chloride layers of MOCl (M=Fe, Bi) materials, which are used as cathode material in chloride based rechargeable batteries. The influence of dispersion corrections (DFT+D2) on geometry and electronic structures are discussed. In addition, an electrode reaction process  $FeOCl + e^- \rightleftharpoons FeO + Cl^-$  is simulated with a 2x1x2 super cell.

A summary is given in chapter 6.





## 2 Theoretical background

Nowadays, two main approaches exist for a computational treatment of bulk properties, surfaces and point defects of periodic systems. The first one imposes periodic boundary conditions (PBC) and, to reduce the interactions between adsorbents on the surface or neighboring defects, usually larger supercells are needed. However, the computational demand significantly increases especially when density functional theory (DFT) is applied with inclusion of Fock exchange. Moreover, periodic calculations with wave function-based post-Hartree–Fock methods are still computationally prohibitive, except for the simplest systems. For example, equilibrium geometry, formation energy, and bulk modulus of two molecular bulk crystals,  $\text{NH}_3$  and  $\text{CO}_2$ , have been investigated at the periodic post-Hartree–Fock correlated level with the CRYSCOR code [23, 24].

An alternative approach relies on embedded cluster models for calculations on defects in ionic crystals and on their surfaces. In embedding schemes the entire extended system is divided into a local region and an environmental region. The local region is described by a quantum mechanical (QM) method, whereas the electrostatic potential of the surrounding is usually described by point charges. For the QM part, standard quantum chemical calculations can be carried out using any method such as DFT including Fock exchange, Møller–Plesset theory and coupled cluster, taking into account only the additional contributions of the external electrostatic potential in the one-electron part of the Hamiltonian. The challenging task of electrostatic embedding schemes is the calculation of the Coulomb potential for infinitely large periodic arrays of PCs. Because of the long-range nature of the Coulomb interactions it is generally impossible to reproduce the Madelung potential by finite arrays of PCs.

Details of these two models will be discussed in the following, together with electronic structure methods used throughout the thesis.

## 2.1 Density Functional Theory

Density functional theory is nowadays the most widely used method for describing medium and large systems [25-27], because of its low computational demands combined with a feasible accuracy. The basic idea is that for systems with a non-degenerate ground state, the ground state energy, wave function, and all other electronic properties are uniquely determined by the ground state electron probability density  $\rho_0(x, y, z)$ , a function of only three variables. The statement was proven by Hohenberg and Kohn in 1964 [28]. Fundamental aspects of DFT are described in the following.

### 2.1.1 The Hohenberg-Kohn Theorem

We start from the electronic Hamiltonian in atomic units:

$$\hat{H} = -\frac{1}{2} \sum_{i=1}^n \nabla_i^2 + \sum_{i=1}^n V_{ext}(\mathbf{r}_i) + \sum_j \sum_{i>j} \frac{1}{r_{ij}} \quad (2.1.1)$$

$V_{ext}$  is called external potential acting on electron  $i$ , since it is produced by charges outside of the system of electrons. The first theorem from Hohenberg-Kohn states that the total energy of a many electron system in an external potential  $V_{ext}(\mathbf{r})$  is a unique functional of the electron density  $\rho(\mathbf{r})$ ,

$$E_0 = \int \rho_0(\mathbf{r}) V_{ext}(\mathbf{r}) dr + \hat{T}[\rho_0] + \hat{V}_{ee}[\rho_0] = \int \rho_0(\mathbf{r}) V_{ext}(\mathbf{r}) dr + F[\rho_0] \quad (2.1.2)$$

A second theorem proven by Hohenberg and Kohn is that the true ground state electron density has a lower energy relative to all trial densities  $\rho_{tr}(\mathbf{r})$ .

$$\int \rho_{tr}(\mathbf{r}) V_{ext}(\mathbf{r}) dr + F[\rho_{tr}] \geq E_0[\rho_0] \quad (2.1.3)$$

Although the Hohenberg-Kohn theorems are of great theoretical value, they do not provide a practical way to calculate  $E_0$  from  $\rho_0$ , because the functional  $F[\rho_0]$  is unknown.

## 2.1.2 Kohn-Sham Method

In 1965, Kohn and Sham [29] developed, with the introduction of atomic orbitals, a formalism that is the foundation for the current application of DFT in the computational chemistry field, a practical method for finding  $\rho_0$  and for finding  $E_0$  from  $\rho_0$ . The central premise in the Kohn-Sham approach is that the kinetic energy functional of a system can be split into two parts: one part that can be calculated exactly and that considers electrons as non-interacting particles and another part, which is a small correction term accounting for electron-electron interaction. Following the Kohn-Sham formalism, within an orbital formulation, the electronic energy of the ground state of a system comprising  $n$  electrons and  $N$  nuclei can be written as:

$$E[\rho] = - \sum_{\alpha=1}^N Z_{\alpha} \int \frac{\rho(\mathbf{r}_1)}{r_{1\alpha}} d\mathbf{r}_1 - \frac{1}{2} \sum_{i=1}^n \langle \Psi_i^{KS}(1) | \nabla_1^2 | \Psi_i^{KS}(1) \rangle \quad (2.1.4)$$

$$+ \frac{1}{2} \int \int \frac{\rho(\mathbf{r}_1)\rho(\mathbf{r}_2)}{r_{12}} d\mathbf{r}_1 d\mathbf{r}_2 + E_{xc}[\rho]$$

The first term represents the nuclear-electron interactions, the second term accounts for the kinetic energy of the noninteracting electrons, and the third term corresponds to the Coulombic repulsions between the total charge distributions at  $\mathbf{r}_1$  and  $\mathbf{r}_2$ . Finally, the fourth term, known as the exchange correlation term, represents the correction to the kinetic energy arising from the interacting nature of the electrons, and all non-classic corrections to the electron-electron repulsion energy. The key to accurate KS DFT calculation of molecular properties is to get a good approximation to  $E_{xc}$ .

The ground state electron density can be written as a function of one-electron orbitals (the Kohn-Sham orbitals), given by:

$$\rho = \sum_{i=1}^n |\Psi_i^{KS}|^2 \quad (2.1.5)$$

The Kohn-Sham orbitals are found as follows. The Hohenberg-Kohn variation theorem (2.1.2) tells us that we can find the ground state energy by varying  $\rho$  so as to minimize the functional  $E_v(\rho)$ . Equivalently, instead of  $\rho$ , we can vary the KS orbitals, which determine the  $\rho$  by (2.1.5).

$$\left[ -\frac{1}{2}\nabla_1^2 - \sum_{\alpha} \frac{Z_{\alpha}}{r_{1\alpha}} + \int \frac{\rho(\mathbf{r}_2)}{r_{12}} d\mathbf{r}_2 + V_{xc}(1) \right] \Psi_i^{KS}(1) = \varepsilon_i^{KS} \Psi_i^{KS}(1) \quad (2.1.6)$$

The exchange correlation potential  $V_{xc}$  is found as the functional derivative of the exchange correlation energy  $E_{xc}$ :

$$V_{xc}(\mathbf{r}) \equiv \frac{\delta E_{xc}[\rho(\mathbf{r})]}{\delta \rho(\mathbf{r})} \quad (2.1.7)$$

Once  $E_{xc}$  is known,  $V_{xc}$  can be readily obtained.

### 2.1.3 Spin density functional theory

A framework for the description of spin coupling is provided by spin density functional theory (SDFT) [30, 31]. If we deal with collinear spin polarization, the electron density  $n$  has now two fundamental variables, a spin up  $n_{\uparrow}$  and spin down density  $n_{\downarrow}$ . In order to reproduce both of these in the non-interacting system one must apply two effective potentials,  $v_{s,\uparrow}(\mathbf{r})$  and  $v_{s,\downarrow}(\mathbf{r})$ . The charge density  $n(\mathbf{r})$  and spin magnetization density can be calculated from the fundamental variables  $n_{\uparrow}$  and  $n_{\downarrow}$ :

$$n(\mathbf{r}) = n_{\uparrow}(\mathbf{r}) + n_{\downarrow}(\mathbf{r}) \quad 2.1.8$$

$$m(\mathbf{r}) = \mu_0(n_{\uparrow}(\mathbf{r}) - n_{\downarrow}(\mathbf{r})) \quad 2.1.9$$

where  $\mu_0 = q\hbar/2mc$  is the Bohr magneton. More generally, the Hohenberg Kohn theorem of SDFT states that the ground-state wave function and all ground-state observables are unique functionals of  $n$  and  $m$  or, equivalently, of  $n_{\uparrow}$  and  $n_{\downarrow}$ .

The Kohn-Sham equations from (2.1.6) can be rewritten as:

$$\begin{aligned} \left[ -\frac{1}{2}\nabla_r^2 + \int \frac{n(\mathbf{r}')}{|\mathbf{r} - \mathbf{r}'|} d\mathbf{r}' + V_{ext}^{\sigma}(\mathbf{r}) + V_{xc}^{\sigma}(\mathbf{r}) \right] \Psi_{\sigma,i}^{KS}(\mathbf{r}) \\ = \varepsilon_{\sigma,i}^{KS} \Psi_{\sigma,i}^{KS}(\mathbf{r}) \end{aligned} \quad 2.1.10$$

where  $\sigma$  denotes the spin index. The exchange correlation hole can be decomposed into an exchange and correlation part, with the exchange hole only applying parallel spin alignments, whereas correlation hole appears for both parallel and anti-parallel spin alignments. The exchange correlation potential  $V_{xc}^{\sigma}(\mathbf{r})$ , which is defined by the functional derivative of the exchange correlation energy as

$$V_{xc}^\sigma(\mathbf{r}) \equiv \frac{\delta E_{xc}[n_\sigma(\mathbf{r})]}{\delta n_\sigma(\mathbf{r})} \quad 2.1.11$$

can have different values for the two spin directions even without an external magnetic field.

In the presence of an internal magnetic field  $\mathbf{B}_{xc}$  (i.e., in spin-polarized systems) we obtain  $V_{xc,\uparrow} - V_{xc,\downarrow} = \mu_0 \mathbf{B}_{xc}$ . This field is the origin of, e.g., ferromagnetism in transition metals. Spin-polarized magnetism only appears if the energy gain by flipping an electron spin is higher than the energy loss by the additional kinetic energy the electron takes.

The spin density functional theory discussed above is exact in principle, but as we mentioned before, the unknown part from DFT is the functionals of the exchange correlation part,  $E_{xc}$  and  $V_{xc}^\sigma$ .

#### 2.1.4 Local-Density Approximation (LDA)

In the uniform electron gas, electrons move on a positive background charge distribution. This defines the Local Density Approximation (LDA) with  $E_{xc}$  given as:

$$E_{xc}^{LDA}[\rho] = \int \rho(\mathbf{r}) \varepsilon_{xc}(\rho) d\mathbf{r} \quad (2.1.12)$$

where the integral is over the entire space, and  $\varepsilon_{xc}(\rho)$  is the exchange-correlation energy per particle of a uniform electron gas of density  $\rho(\mathbf{r})$ .

One can show that  $\varepsilon_{xc}$  can be split into exchange and correlation parts:

$$\varepsilon_{xc}(\rho) = \varepsilon_x(\rho) + \varepsilon_c(\rho) \quad (2.1.13)$$

The exchange portion is generally expressed as:

$$\varepsilon_x(\rho) = -\frac{3}{4} \left( \frac{3}{\pi} \right)^{\frac{1}{3}} (\rho(\mathbf{r}))^{\frac{1}{3}} \quad (2.1.14)$$

As for the correlation contribution, no such explicit expression is known. Instead, one uses analytical expressions typically derived from highly accurate simulations of a homogeneous electron gas. For example, Vosko, Wilk, and Nusair (VWN) [32] calculated the correlation part and the results have been expressed as a very complicated

function  $\varepsilon_c^{VWN}$  of  $\rho$ .

### 2.1.5 Gradient Corrected and Hybrid Functionals

Typical molecular systems are generally very different from a homogeneous electron gas. To improve upon this limitation in the LDA/LSDA approach, information pertaining to the gradient of the charge density ( $\nabla\rho(\mathbf{r})$ ) is supplemented to the density ( $\rho(\mathbf{r})$ ) at a particular point  $\mathbf{r}$ . Such an approximation is known either as Gradient Corrected (GCA) or Generalized Gradient Approximation (GGA). In general, GGA functionals are constructed with a correction added to the original LDA/LSDA term:

$$E_{xc}^{GGA}[\rho] = \int f(\rho(\mathbf{r}), \nabla\rho(\mathbf{r})) d\mathbf{r} \quad (2.1.15)$$

Approximate gradient correlated exchange and correlation energy functionals are developed using theoretical considerations as a guide such as the known behavior of the true (but unknown) functionals  $E_x$  and  $E_c$  in various limiting situations, together with empirical parameters in [33]. In the thesis, we use mostly the PW91 [34] and PBE [35] functionals for our GGA calculations.

In general, exchange contributions are significantly larger than correlation effects; thus, an accurate expression for the exchange energy is mandatory for a meaningful exchange correlation functional. For this purpose, an exact Hartree-Fock exchange contribution can be incorporate into the DFT functional, obtaining a so-called hybrid functional, which is widely used. For example, the most popular B3LYP [36] hybrid functional is defined by:

$$E_{xc}^{B3LYP} = (1 - a_0 - a_x)E_x^{LSDA} + a_0E_x^{HF} + a_xE_x^{B88} + (1 - a_c)E_c^{VWN} + a_cE_c^{LYP} \quad (2.1.16)$$

which incorporates exact HF exchange, exchange and correlation (Vosko Wilk Nusair, VWN) terms derived from LSDA, and the Becke exchange and LYP correlation terms. The parameter values  $a_0 = 0.20$ ,  $a_x = 0.72$ , and  $a_c = 0.81$  were chosen to give good fits to experimental molecular atomization energies.

## 2.2 Periodic Calculations and Supercell Approach

Throughout this thesis, we will be interested in periodic systems, built from a basic unit cell that is periodically repeated in three directions of space to infinity. On first glance, such calculations seem to be impossible because a wave function has to be calculated for a very large number of electrons in the system, extending over the entire solid, such that the basis functions necessary to expand them will be nearly infinite. However, by taking advantage of the periodicity, only the particles contained in one unit cell have to be treated explicitly.

### 2.2.1 Bloch theorem

For a system where the nuclei are arranged in a periodic structure, the equation

$$V(\mathbf{r} + \mathbf{R}) = V(\mathbf{r}) \quad (2.2.1)$$

holds, where  $\mathbf{R}$  is a lattice vector. According to Bloch's theorem [37], a wave function of such a periodic system can be written as:

$$\psi_{nk}(\mathbf{r}) = e^{i\mathbf{k}\cdot\mathbf{r}} \mu_{nk}(\mathbf{r}) \quad (2.2.2)$$

where  $n$  is the "band index" and  $\mathbf{k}$  is a wave vector confined to the first Brillouin zone of the reciprocal lattice.  $\mu_{nk}$  is translationally invariant, i.e.

$$\mu_{nk}(\mathbf{r} + \mathbf{R}) = \mu_{nk}(\mathbf{r}) \quad (2.2.3)$$

In the one dimensional case, with the application of Bloch's theorem, one can confine a linear chain to a circle as illustrated in Figure 2.1. The physical meaning of Bloch's theorem is that the wave functions at positions  $\mathbf{r}$  and  $\mathbf{r} + \mathbf{R}$  are the same except for the phase factor  $e^{i\mathbf{k}\cdot\mathbf{r}}$ , and more importantly that the electron density has the same periodicity as the potential. Hence it is sufficient to consider the orbitals and their eigenvalues only in the first Brillouin-zone. Using periodic boundary conditions leads to a Hermitian eigenvalue equation over the Wigner-Seitz cell in the crystal. For a fixed  $\mathbf{k}$ , there will be an infinite number of solutions with raising energy values.

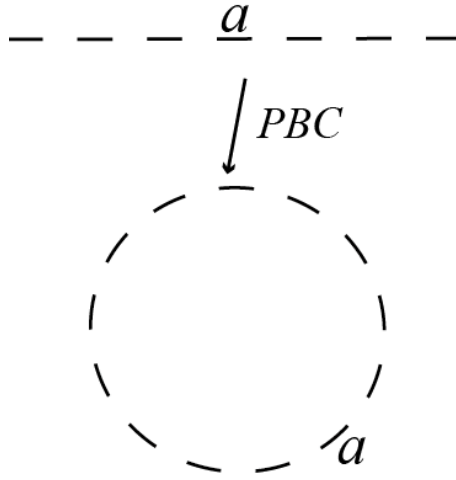


**Figure 2.1** Illustrative schemes for periodic boundary condition in the one-dimensional case.

## 2.2.2 Plane waves and Pseudopotential

It is convenient to choose plane waves as basis functions, since the plane wave function  $e^{iGr}$  for any reciprocal vector  $G$  is itself a cell-periodic function.

$$\mu_{nk}(\mathbf{r}) = \frac{1}{\sqrt{\Omega}} \sum_{\mathbf{G}} C_{Gnk} e^{iGr} \quad (2.2.4)$$

Then (2.2.2) becomes,

$$\psi_{nk}(\mathbf{r}) = \frac{1}{\sqrt{\Omega}} \sum_{\mathbf{G}} C_{Gnk} e^{i(k+\mathbf{G})r} \quad (2.2.5)$$

where  $\Omega$  is the volume of the cell. The kinetic energy operator is diagonal in a plane wave representation. Similarly, the potential is diagonal in real space. The use of Fast Fourier Transforms (FFT) to switch between these representations provides a large saving in computational cost.

The main disadvantage of a plane wave basis set is its inefficiency. In principle the expansion in plane waves includes a summation over an infinite number of  $G$  vectors. In practice, however, this is done by introducing a kinetic energy cut-off, often referred to as the plane wave cut-off, defined as:



$$\frac{|k + \mathbf{G}|^2}{2} < E_{cutoff} \quad (2.2.6)$$

Another approximation is based on the assumption that only the valence electrons have significant effect on the physical and chemical properties of a system. In the frozen-core approximation, one uses this fact and sets the orbitals of the core-electrons equal to those of the isolated atom. Only the valence electron orbitals are updated during the self-consistent iterations. However, valence orbitals have rapid oscillations near atomic nuclei due to the requirement of orthogonality with core orbitals. To treat the rapid variation of the valence orbitals in the core region, a large number of plane waves are needed for convergence. One solution is the use of a pseudopotential [38, 39], in which the interactions of the valence electrons with the nuclei and the core-electrons are described by an effective, much weaker potential. The resulting pseudo-orbitals are smooth inside the core region and are equal to the real orbitals outside the core region. The graphical representation of the behavior of a wave function and potential is depicted in Figure 2.2.

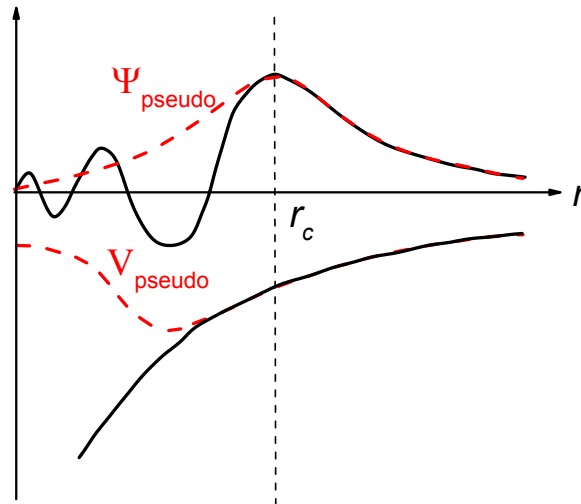


**Figure 2.2** Comparison of a wavefunction in the Coulomb potential of the nucleus (blue) to the one in the pseudopotential (red). The curves coincide above a certain cutoff radius (core radius)

$r_c$ .

Pseudopotentials can be constructed using many different schemes. Common used ones include norm-conserving pseudopotentials (NCPP) [40], ultra-soft pseudopotentials (USPP) [41], and the projected augmented waves (PAW) method [42, 43], which we use in this thesis. The PAW is based on a transformation of the pseudo wave function to the all-electron wave function by introduction of linear transformation operator  $\hat{T}$  within some spherical augmentation region:

$$|\psi_k\rangle = \hat{T}|\tilde{\psi}_k\rangle = |\tilde{\psi}_k\rangle + \sum_a (|\phi_a\rangle - |\tilde{\phi}_a\rangle) \langle \tilde{P}_a | \tilde{\psi}_k \rangle \quad (2.2.7)$$

where  $|\phi_a\rangle$  are all-electron partial waves, and  $|\tilde{\phi}_a\rangle$  stands for pseudo partial waves; projector functions are orthogonal to pseudo partial waves,  $\langle \tilde{P}_i | \tilde{\phi}_j \rangle = \delta_{ij}$ . Thus, the wave function is decomposed as the sum of the smooth wave function and sum over atoms (index a). At each atom we have “1-center all electron” minus “1-center pseudo”. The difference is non-zero only within some spherical augmentation region. Outside the augmentation regions, the pseudo partial waves are equal to the all-electron partial waves. The all electron partial waves, which are calculated once as solutions of the radial part of the Schrödinger equation for the isolated atoms, ensures that the nodal structure of the wave function is physically correct near the nucleus. Like the orbitals, also all other quantities, e.g. the electron density and the total energy, can be transformed between the all electron and the pseudopotential representation.

The plane-wave expansion has to be truncated with care, as a too small energy cut-off will lead to sizable errors in the computed physical quantities while a too large energy cut-off will become computationally prohibitive. To obtain a reasonable convergence for a given system, both the plane wave cutoff  $E_{\text{cutoff}}$  and the number of k-points included in the calculations should be tested. In practice only a few k-points of the first Brillouin zone are included and the actual number required for convergence of the total energy depends on both the size and the type of the system under study. Several methods exist for generating the k-points in the first Brillouin zone, the most common one being the Monkhorst-Pack scheme [44].

### 2.2.3 Supercell Approach

The atomic arrangement in perfect crystals is described by a periodically repeated unit cell in all three dimensions and one can employ Bloch's theorem to obtain bulk properties. For oxide surfaces that we are interested in, however, perfect periodicity is absent, the system is only periodic in two dimensions. To deal with this, one uses a crystal slab with two surfaces and a finite number of layers. Assuming the surface is normal to the  $z$  direction, to recover three-dimensional periodicity, the slab is now repeated in the  $z$  direction by adding a sufficiently large vacuum region. The vacuum region must be large enough to separate both surfaces of the slab and to avoid any interactions of opposing surfaces or adsorbates. Moreover, the slab has to be thick enough to accurately model bulk states and any surface relaxations. For oxide surfaces, four or more layers are already sufficient to achieve convergence. A supercell is then constructed based on a slab configuration, an illustrative example of ZnO can be seen in Figure 2.3. The size of the supercell has to be chosen such that it either corresponds to known experimental coverages or is large enough to exclude any lateral interactions between adsorbates.

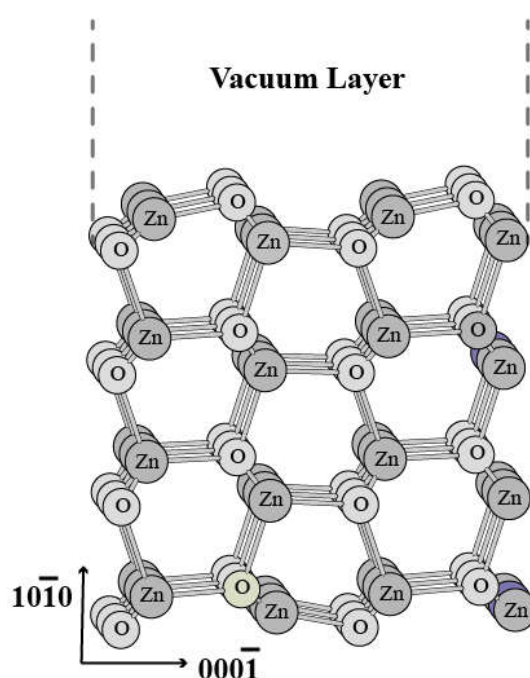


**Figure 2.3** Supercell approach: A slab with a finite number of layers and a sufficiently large vacuum region are periodically repeated to model an oxide surface

Supercells cannot only be used to study surface, but are also convenient to simulate defects in crystals with a periodically repeated fictitious supercell. The form and the size of the supercell depend on the physical system being studied. The study of point defects requires that a defect does not interact with its periodic replica in order to accurately simulate a truly isolated defect. Even finite systems (molecules, clusters) can be studied with supercells using  $\Gamma$ -point approximation. Enough empty space between the periodic replicas of the finite system must be left so that the interactions between them are weak.

#### 2.2.4 On-site Correction (DFT+U)

The true exchange correlation term  $E_{xc}$  of DFT contains a self-interaction correction that cancels the self-interaction energy present in  $\frac{1}{2} \int \int \frac{\rho(r_1)\rho(r_2)}{r_{12}} d\mathbf{r}_1 d\mathbf{r}_2$  exactly. Currently used functionals, however, cannot fully compensate this effect, which leads to the so called self-interaction error. In molecular systems, commonly used functionals give incorrect potential curves at large internuclear distances for symmetrical radical ions such as  $H_2^+$ ,  $He_2^+$  and  $F_2^+$  and overestimate the intermolecular interaction in some charge transfer complexes, due to the self-interaction error [45]. In solids or other periodic systems, self-interaction is the reason for the well-known “band gap problem”[46], in which DFT in the LDA/GGA fails to correctly predict the energy gaps between occupied and unoccupied states. An example is given in Table 4.1 from chapter 4, where the PBE functional underestimates the band gap of rutile  $TiO_2$  by  $\sim 1.3$  eV. Since the Hartree-Fock (HF) method is free of self-interaction, the error in LDA/GGA can be reduced by incorporating a certain percentage of Hartree-Fock exchange, which is done for hybrid functionals (chapter 2.1.5). However, these hybrid functionals are very time consuming with large super cells, which are needed for simulating surfaces and defects.

As a remedy, the DFT+U approximation (i.e. LDA+U or GGA+U) has been proposed for the treatment of strongly correlated d-d or f-f interactions in transitional metal systems, based on the model Hamiltonian:

$$\hat{H} = \frac{\bar{U}}{2} \sum_{m,m',\sigma} \hat{n}_{m,\sigma} \hat{n}_{m',-\sigma} + \frac{\bar{U} - \bar{J}}{2} \sum_{m \neq m',\sigma} \hat{n}_{m,\sigma} \hat{n}_{m',\sigma} \quad (2.2.8)$$

where the summation is performed over projections of the orbital momentum ( $m, m' = -2, -1, \dots, 2$  in the case of d electrons) and  $\bar{U}$  and  $\bar{J}$  are the spherically averaged matrix elements of the screened Coulomb electron-electron interaction. In many occasions, a more simple expression of the Hubbard correction ( $E_{Hub}$ )

$$E_{Hub} = \frac{(U - J)}{2} \sum_{\sigma} \left[ \left( \sum_m \hat{n}_{m,m}^{\sigma} \right) - \left( \sum_{m,m'} \hat{n}_{m,m'}^{\sigma} \hat{n}_{m',m}^{\sigma} \right) \right] \quad (2.2.9)$$

introduced by Dudarev et al. [47], is adopted and implemented.

This can be understood as adding a penalty functional to the LDA/GGA total energy expression that biases the on-site occupancy matrix towards idempotency, i.e.,  $\hat{n}_{\sigma} = \hat{n}_{\sigma} \hat{n}_{\sigma}$ . In Dudarev's approach the parameters U and J do not enter separately, since only the difference (U-J) is meaningful. In the LDA+U method, the electrons are divided into two classes: delocalized s, p electrons which are well described by LDA (GGA) and localized d or f electrons.

### 2.2.5 Density of state (DOS)

An important quantity for many purposes is the density of states (DOS), which gives the number of electronic states (i.e., the orbitals) that have a particular energy.

$$n(E) = \sum_{i=1}^{\infty} \delta(E - \epsilon_i) \quad (2.2.10)$$

where the sum extends over all eigenstates of the Kohn-Sham Hamiltonian.

In practice, a finite number of eigenstates is considered, and we take two smearing approaches to get a continuous distribution appropriate for a bulk material. The first one is Methfessel-Paxton smearing [48] for semiconductors or insulators with the tetrahedron method (ISM EAR=-5 for VASP inputs). This method gives a good account for the electronic DOS and recommend by VASP manual. The second method is Gaussian smearing [49] (ISM EAR=0 keyword in combination with a small

SIGMA=0.05 for VASP inputs), which we use, if the cell is too large or only a single K-point.

In order to study the interaction of orbitals with each other that cannot be clearly assigned to atoms by total density of states (TDOS) as defined by (2.2.10), the projected density of states (PDOS) is defined as:

$$n_{\alpha}(E) = \sum_{i=1}^{\infty} |\langle \phi_{\alpha} | \varphi_i \rangle|^2 \delta(E - \epsilon_i) \quad (2.2.11)$$

where  $\phi_{\alpha}$  is a properly chosen localized function. In a plane wave basis, the wave function is usually truncated to a sphere around an atom and then projected on the respective atomic s, p, and d orbitals.

### 2.3 Embedded cluster method

With periodic boundary conditions, many interesting physical systems, oxide surfaces and defects as we mentioned in 2.2.3, have to be treated by large supercells. An alternative, very often used approach for modeling the surfaces and defects, is embedded clusters (EC) [50-52]. Instead of building up a large super cell, only a finite cluster size is required to be treated quantum mechanically, such that the procedure can be easily applied at any level of theory.

For the embedding cluster calculations, the total system is split into three parts: the inner ( I ) part, which is a fully quantum mechanically treated cluster; an intermediate ( II ) layer, where cations are replaced by effective core potentials (ECPs) and anions by ECPs or simply by point charges and finally an outer ( III ) part, where the environment of the cluster is described by a periodic array of point charges, representing cationic and anionic sites of a perfect ionic crystal. The "isolating" outer ECP shell surrounding the actual QM part is necessary in order to prevent artificial polarization of the electron density by cations which would otherwise be in a direct contact with the QM boundary [53, 54]; An illustrative example of ZnO can be seen in Figure 2.4.

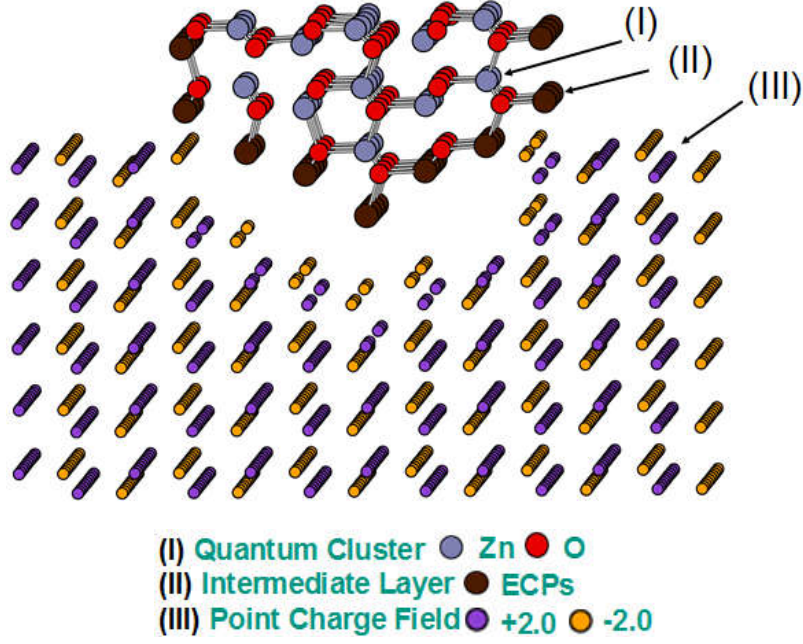


*Figure 2.4 embedded cluster approach with ZnO example.*

The challenging task of electrostatic embedding schemes is the calculation of the Coulomb potential for infinitely large periodic arrays of PCs. Because of the long-range nature of the Coulomb interactions it is generally impossible to reproduce the Madelung potential by finite arrays of PCs. Several different approaches have been developed to include the Madelung potential in embedded cluster schemes. Here, we apply two different approaches. a) periodic electrostatic embedded cluster method (PEECM) [54] based on the periodic fast multipole method (PFMM) [55, 56]. b) a point charge field with dipole and quadrupole moments elimination by the Evjen type approximation [57, 58].

### 2.3.1 Periodic Fast Multipole Method (PEECM)

To account for electrostatic interactions between the point charges and quantum cluster part, an additional term is included in the Fork matrix (or Kohn–Sham matrix):

$$F_{\mu\nu}^{emb} = - \sum_L^{lattice} \sum_j^{UC} q_j \int \frac{\mu(r - R_\mu) v(r - R_\mu) \delta(r' - R_j + \mathbf{L})}{|r - r'|} d_r d_{r'} \quad (2.3.1)$$

where  $\mathbf{L}$  represents a lattice vector in direct space and  $j$  is the index over point charges with charge of  $q$  at position  $R_j - \mathbf{L}$  outside the QM cluster. Gaussian basis functions  $\mu$

and  $v$  are defined at positions  $R_\mu$  and  $R_j$  which belong to the QM cluster. For total energy, a  $J^{emb}$  term is added as well:

$$J^{emb} = \sum_{\mu\nu}^{cluster} D_{\mu\nu} F_{\mu\nu}^{emb} + \sum_L^{lattice} \sum_j^{UC} \sum_a^{cluster} \frac{q_j Z_a}{|R_a - R_j + L|} \quad (2.3.2)$$

Elements  $D_{\mu\nu}$  of the density matrix are used together with appropriate Fock matrix elements  $F_{\mu\nu}^{emb}$  to calculate the Coulomb interaction energy between the electron density of the QM part and the lattice of PCs.

The PFMM scheme calculates the electrostatic interaction efficiently by dividing the point charges in the surrounding of the QM cluster into a near-field (NF) and far-field (FF) parts. The radius of the NF is given by the well-separateness criterion [59]:

$$D \geq (WS + 1)L \quad (2.3.3)$$

where we usually have a default WS value of 3 [59]. It is chosen large enough to ensure rapid convergence of the multipole approximation used for the FF interactions. The terms  $F_{\mu\nu}^{NF}$  and  $J^{NF}$  are calculated as direct sums of Coulomb interactions over all  $L \in$  NF. The calculation of the remaining interactions between the QM cluster and the PC in the FF part employs multipole expansions [55, 56].

The computational cost of the PEECM scheme part is negligible compare to a total DFT calculation and the quantum cluster can have large sizes. For a QM cluster with over 8000 basis functions, the total CPU time spent on the embedding part does not exceed 30 s on a single CPU [54].

### 2.3.2 Evjen Procedure

For calculating electrostatic interactions with a periodic system, one of the simplest methods was introduced by Evjen [57]. The method eliminates the dipole moment of the unit cell by distributing the corner and face atoms over all equivalent symmetry points, such that rapid convergence is guaranteed. Later works [58, 60, 61] extended this method by adding artificial fractional charges at the borders of the unit cell in order to eliminate lowest multipole moments. As illustrated in Figure 2.5, two fractional



charges are added to cancel the dipole moment on x direction. With the extension of the unit cell to a large point charge field, we notice here that the fractional charges at all inner boundaries are cancelled, only left two fractional charges at the outermost borders. The virtue of this construction is that low multipole moments are zero or small irrespective of the size of the PC field and that the Madelung energy as well as the electrostatic potential above the surface converge quite rapidly.

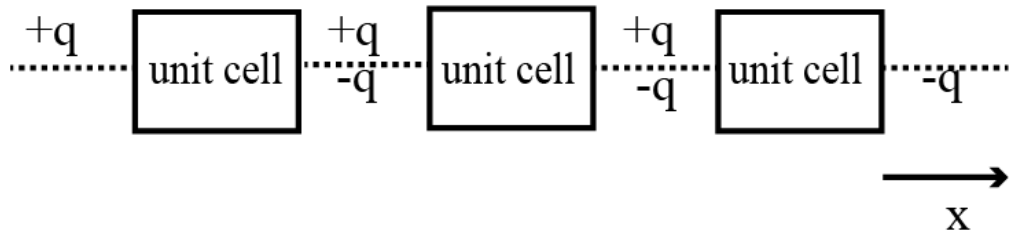


**Figure 2.5** Distributions of fractional point charges, which can annihilate the dipole of a unit cell.

### 3 Adsorption of formic acid on the nonpolar ZnO (10-10) surface

#### 3.1 Introduction

The adsorption of molecules on zinc oxide surfaces has been extensively studied because of the importance of surface reactions at ZnO surfaces in a wide range of industrial applications, such as heterogeneous catalysis [62, 63] and dye-sensitized solar cells (DSSCs) [64]. The adsorption of formic acid (HCOOH) on ZnO surfaces is of particular importance in the latter field. Surface-bound HCOO\* and HCOOH\* are proposed to be important intermediate species of methanol production from syngas (CO/CO<sub>2</sub>/H<sub>2</sub>). Furthermore, formic acid (HCOOH) on ZnO can serve as a model system for solar cells (Grätzel-cell) [10-12], in which carboxylate groups are often responsible for the dye-surface contact.

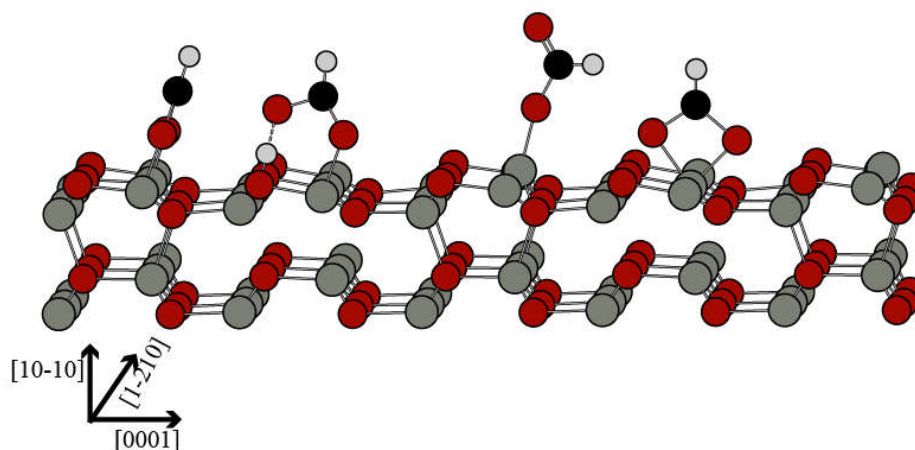


**Figure 3.1** Ball-stick model of potential adsorption configurations of dissociated formic acid on ZnO(10-10). From left to right, structure I is a bidentate, structure II a quasi-bidentate, structure III a monodentate, structure IV a chelate.

In previous work a number of different possible formate structures have been proposed to result from the dissociative adsorption of formic acid on ZnO(10-10) surfaces. Structural models of the proposed structures are shown in Figure 3.1, which is

furthermore used to define the terminology used throughout this chapter.

The bidentate formate (structure I), where the oxygen atoms of the acid are bound to the Zn atoms along the [11-20]-direction, is the structure which has been proposed in most of the previous theoretical studies on metal oxides [65, 66] and in particular on ZnO [67-69]. The quasi-bidentate formate along the [0001]-axis (Figure 3.1, structure II), occasionally also referred to as unidentate, has been favored in the theoretical studies by Persson et al. [68, 69]. Here, the formate is bound via the carbonyl oxygen to a zinc atom of the surface and via the hydrogen of the hydroxyl group to an oxygen at the surface of the substrate.

The monodentate, where the formate is bound via the oxygen to a zinc atom of the surface, could exist as cis- or trans-isomer (Figure 3.1, structure III) [70, 71]. In the Hartree-Fock (HF) calculations of Nakatsuji et al. this structure was found to be unstable [67]. The formate could also exist as a chelate, where both oxygen atoms of the acid are bound to one Zn atom (Figure 3.1, structure IV). (Here we use the chemical description of a chelate which is different from the description of Crook et al., where this configuration is referred to as bidentate [70].) The chelate could be oriented along the [11-20]- or the [0001]-direction. Another possible bidentate could be bound over an oxygen vacancy along the [0001]-direction. This geometry was found as one of the stable configurations for formic acid on anatase-TiO<sub>2</sub> (101) [72].

On the basis of Near-Edge-X-ray-Absorption Fine Structure (NEXAFS) spectroscopy, it has been proposed that HCOOH deprotonates yielding a formate species with a nearly upright standing geometry on the ZnO (10-10) surface [73]. On the basis of this data, Davis et al. proposed the presence of a chelate species with its molecular plane oriented along the [0001] direction. In another experimental study, Crook et al. investigated the formic acid adsorption on the ZnO (10-10) surface at room temperature with High Resolution Electron Energy Loss Spectroscopy (HREELS). They observed vibrations at 1040, 1363, 1573 and 2895 cm<sup>-1</sup>, which were assigned to  $\pi(\text{CH})$ ,  $\nu_{\text{sym}}(\text{OCO})$ ,  $\nu_{\text{asym}}(\text{OCO})$  and  $\nu(\text{CH})$ -modes, respectively [70]. Similar results were obtained with perdeuterated formic acid (DCOOD), namely vibrations at 1330, 1580 and 2154 cm<sup>-1</sup>, which were assigned to  $\nu_{\text{sym}}(\text{OCO})$ ,  $\nu_{\text{asym}}(\text{OCO})$  and  $\nu(\text{CD})$ -modes of DCOO species,

respectively [70]. Previous infrared spectroscopy measurements of the adsorption of formic acid on ZnO powder particles showed rather broad bands assigned to the asymmetric carboxylate stretching vibration at  $1589\text{ cm}^{-1}$  and the symmetric at  $1350\text{ cm}^{-1}$ . From comparison with vibrational frequencies calculated with density functional theory (DFT/B3LYP) for a  $\text{Zn}_{10}\text{O}_{10}$  cluster, they concluded a bidentate species [74]. However, for the hybrid functionals the sizes of clusters which can be treated is rather limited.

Embedded cluster calculations using a wave-function based approach in connection with Møller-Plesset second order perturbation theory (MP2) were performed on a  $\text{Zn}_4\text{O}_4$  cluster by Nakatsuji et al. and revealed a bidentate as well as a quasi-bidentate formate species [67] with almost identical binding energies of 79 kcal/mol. In their calculations, the chelate configuration of the formate was found to be unstable. For the free formic acid molecule two conformations exist: cis-formic acid, where both protons are on the same side, and trans-formic acid where the protons are on opposite sides. Whereas for the free molecule the cis-form is the most stable conformation, for adsorbed formic acid the trans-conformation was found to be favored, because the proton is closer to the oxygen atom of the substrate and can form a hydrogen bond [67]. Periodic Hartree-Fock calculations reported by Persson et al. revealed that a tilted bidentate is more stable than the quasi-bidentate [68]. Later Persson et al. also investigated a chelate configuration which was in comparison to the other structures only weakly bound to the surface (30 kcal/mol) [69]. Labat et al. [75] compared and discussed bidentate and quasi-bidentate adsorption modes of formic acid on the ZnO surface by periodic DFT calculations with hybrid functionals. To summarize, we can underline that all calculations reported so far revealed dissociative adsorption forming a formate species with a strong bond between adsorbate and surface.

In this chapter, we report on PBC calculations for adsorption geometries and the corresponding IR spectra starting from the structures reported in literature. The results are discussed in the context of reflection adsorption (IRRAS) measurements of the group of Prof. Wöll (Institut für Funktionale Grenzflächen (IFG), KIT). Parts of the text, figures and tables are directly taken from ref. [76]. The work has been extended

by a study on the convergence of the results of the PBC calculations with respect to k-point grid and cutoff energy. Furthermore, it was investigated how well the adsorption of formic acid on ZnO can be described by an EC approach, how the results converge with cluster size and basis set, and how they depend on the quantum chemical method.

## 3.2 Computational details

### 3.2.1 Periodic calculations

All PBC calculations were performed with the Vienna ab initio Simulation Package (VASP) [77-79]. The generalized gradient approximation with the functional described by Perdew and Wang [34] (GGA-PW91) was used for all calculations. The projector-augmented wave (PAW) method [42, 43] is applied to describe the wavefunctions in the core regions, while the valence wavefunctions are expanded as linear combination of plane-waves with a cutoff energy of 400 eV. In the geometry optimizations of the wurtzite cell of ZnO, the total energy was converged to  $10^{-5}$  eV and the Hellmann-Feynman force on each relaxed atom was less than  $1 \text{ meV}\text{\AA}^{-1}$ . The equilibrium lattice constants ( $a = 3.285 \text{ \AA}$ ,  $c = 5.297 \text{ \AA}$  and the internal parameter  $u = 0.3793$ ) are similar to PBE results ( $a = 3.282 \text{ \AA}$ ,  $c = 5.291 \text{ \AA}$ ,  $u = 0.3792$ ) [80] and agree well with the experimental values ( $a = 3.2496 \text{ \AA}$ ,  $c = 5.2042 \text{ \AA}$  and  $u = 0.3819$ ) [81].

Based on the optimized bulk cell and lattice constants, the surface calculations were performed using a slab model, consisting of 8 layers of Zn-O, followed by a vacuum layer with a width of  $10 \text{ \AA}$ . The positions of all atoms besides the oxygen atoms of the deepest layer (Figure 3.2) were optimized, until the Hellmann-Feynman forces converged to  $0.01 \text{ eV \AA}^{-1}$ . During optimization, surface Zn atoms of the uppermost layer move downwards; the distance between Zn and O atoms of the surface layer is  $0.35 \text{ \AA}$  and agrees well with experimental data ( $0.4 \text{ \AA}$ ) [82]. To prevent lateral interactions between formic acid molecules on the surface, a supercell with a size of  $3 \times 2$  (96 atoms) was used in the calculations. The Brillouin zone was sampled with a

(3×3×1) Monkhorst-Pack [44] mesh of k-points for the supercell calculations. With help of density-functional perturbation theory (DFPT) or linear response (LR) theory [83, 84], vibrational spectra could be determined as well as the tensor of the Born effective charges [85], which is used to obtain the intensities of the vibrations [86]. Because frequency calculations are very time-consuming, only the first layer of Zn-O was involved. In selected cases test calculations were carried out where a second layer of ZnO was considered. In all cases the differences in the calculated frequencies were below 2 cm<sup>-1</sup>.

The binding energies ( $E_{BE}$ ) of the adsorbate to the surfaces were calculated by using:

$$E_{BE} = E_{(HCOOH/ZnO)} - (E_{HCOOH} + E_{ZnO}).$$

Here,  $E_{(HCOOH/ZnO)}$  denotes the total energy of the respective HCOOH/ZnO adsorbate configuration,  $E_{ZnO}$  is the total energy of the clean ZnO surface, and  $E_{HCOOH}$  is the total energy of the HCOOH molecule with trans-configuration, which was obtained in a 10Å x 10Åx10Å sized cell using  $\Gamma$ -point approximation.

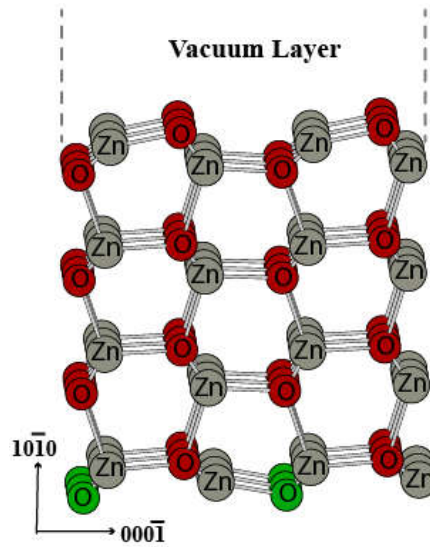


**Figure 3.2** Supercell model for surface calculations. The bottom O layer (green balls) was kept fixed.

### 3.2.2 Embedded cluster calculations

The structures obtained for the slab model of the surface have been obtained in ref 18. They serve as starting point for all further calculations. While the calculations have been performed with the PW91 functional [34] in ref. 18, the calculations have been repeated with the PBE functional [35] which is available in the VASP code [77-79] as well as in the TURBOMOLE program package [87-89]. The latter was used for all embedded cluster calculations. In the cluster calculations, four different quantum clusters,  $Zn_5O_{15}$ ,  $Zn_9O_{19}$ ,  $Zn_{36}O_{58}$ ,  $Zn_{90}O_{139}$ , were investigated (see Figure 3. 5). The clusters are embedded in point charge fields based on the nominal charges. The positive point charges next to quantum cluster were equipped by large core (28e-)  $Zn^{2+}$  pseudopotential [90] to account for the Pauli repulsion of the zinc cations. If not mentioned elsewhere, all calculations were carried out with a def2-SVP basis set [91] for the quantum clusters and a def2-TZVP basis set [92, 93] for the adsorbed formic acid molecule. We evaluated the binding energies with different quantum chemical methods, i.e. HF-SCF, PBE, B3LYP [36] and MP2 [93, 94] at the equilibrium structure optimized at the PBE level. For the MP2 calculations, we also increased the basis set to def2-TZVP. In order to account for the basis set superposition error the counterpoise correction of Boys and Bernardi [95] was applied. In the first step, the BSSE correction to the total energy of the optimized structure is obtained. Therefore the system is cut into two parts, on the one hand, the ZnO cluster in the structure it took in the optimization of the full system, on the other hand, the proton and the formate group which belong originally to the formic acid molecule (FA). For both parts, the total energies were calculated with ( $E_{FA(ZnO)}$  and  $E_{ZnO(FA)}$ ) and without ( $E_{FA}$  and  $E_{ZnO}$ ) the basis set (ghost basis) of the other part. The binding energy  $E_{BE}$  is then calculated from difference of the BSSE corrected total energy and the sum of the energies of the ZnO cluster in the structure it takes without the adsorbed formic acid molecule  $E_{ZnO}^{free}$  and the energy of a formic acid molecule in gas phase  $E_{FA}^{gasphase}$ .

$$E_{FA@ZnO}^{CP} = E_{FA@ZnO} - (E_{FA(ZnO)} - E_{FA}) - (E_{ZnO(FA)} - E_{ZnO})$$

$$E_{BE} = E_{FA@ZnO}^{CP} - E_{ZnO}^{free} - E_{FA}^{gasphase}$$

For the comparison of the different quantum clusters, we kept the atomic positions of the quantum cluster fixed, only the atoms of the formic acid on the surface were optimized. Structural relaxation of ZnO upon adsorption was only taken into account for the  $Zn_{36}O_{58}$  cluster, which was tested to be sufficient for the calculation of the binding energies. The outermost oxygen layer which is directly coordinated to ECPs was fixed, all other atoms of the cluster were allowed to relax. Based on the optimized structures, we computed the hessian matrix and dipole gradients by numerical differentiation of the gradients, to obtain normal modes and harmonic frequencies as well as zero point vibrational energies.

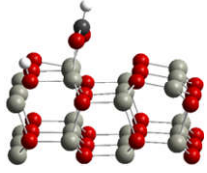
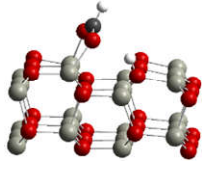
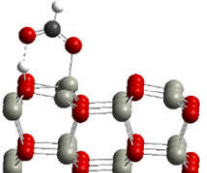
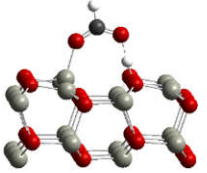
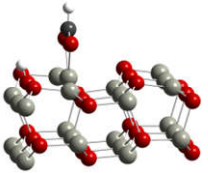
### **3.3 Results and Discussion**

#### **3.3.1 Results of the PBC calculations**

In order to gain further insight into adsorption geometries and the corresponding IR spectra, DFT calculations were performed starting from the structures reported in literature [67-69, 74, 75]. Several possible configurations were considered and minimum energy structures located. The optimized structures and their relative energies  $\Delta E$  with respect to the lowest minimum are given in Table 3.1 and Table 3.2, respectively. The lowest energy was found for the bidentate conformation Ia where dissociated formic acid is adsorbed along the [11-20]- direction of the ZnO(100) surface. The bidentate b differs by the position of the hydrogen transferred to the surface. The interaction of the surface hydrogen with the formate influences the adsorption energy by up to 0.2 eV. These changes in  $\Delta E$  are of the same order as for bidentate configurations on the (110) surface of rutile-TiO<sub>2</sub> where changes of around 0.3 eV [66] were observed. The bidentates are tilted to the surface, the tilt angles are 23° and 25° in respect to the surface normal for bidentate a and bidentate b, respectively. These values agree much better with NEXAFS results (23°) [73] than periodic HF calculations (15°) [68]. The second stable configurations regarding the energy are the quasi-bidentates IIa and IIb. They stand upright without any tilt to the surface.



**Table 3.1** Optimized minimum structures and relative energies (kcal/mol) with respect to bidentate a.

bidentate a	bidentate b	quasi-bidentate a	quasi-bidentate b	chelate
				
$\Delta E = 0.00$	$\Delta E = 4.54$	$\Delta E = 7.97$	$\Delta E = 11.13$	$\Delta E = 14.97$

**Table 3.2** Binding energies with different configurations and methods.

Structure	Adsorption Energy (kcal/mol)		
	Nakatsuji et al (a)	Persson et al.(b)	This work
Bidentate a (Ia)	-79.8	-52.4 (-45.5)(c)	-42.91
Bidentate b (Ib)			-38.37
Quasi-bidentate a (IIa)	-79.6	-40.7	-34.94
Quasi-bidentate b (IIb)		-46.1	-31.78

a) HF cluster calculations [67] b) Periodic HF calculations with one formic acid molecule per  $2 \times 1$  ZnO surface cell, corresponding to a surface coverage of 1/4 monolayer [68, 69].

In the case of the quasi-bidentate configuration along the [0001] direction (Figure 3.1, structure II), the dissociated hydrogen is transferred from the formic acid to a surface oxygen in such a way that it still can form a hydrogen bond to one oxygen of the formate while the other formate oxygen binds directly to a surface Zn atom. The former can either bind to the Zn and the OH group of a surface ZnO dimer with a distance of 2.00 Å ( $\Delta E=7.97$  kcal/mol) or form a bridge between two surface dimers. In the latter case, the Zn-O distances of the Zn adsorption site and the OH group amounts to 3.43 Å and it is with  $\Delta E=11.13$  kcal/mol less stable. In Table 2 the binding energies with respect to the energy of a formic acid molecule and the ZnO(10-10) surface of the different bidentate and quasi-bidentate conformations are compared with the HF calculations of Persson et al. [68] and Nakatsuji et al. [67]. Both, the bidentate and the quasi-bidentate adsorption geometries are stable with respect to desorption. The HF cluster calculations

of Nakatsuji show significantly stronger binding energies, while our results are on the same order as the values obtained by Persson. For the two quasi-bidentates the opposite energetic order was observed. The origin might be the neglect of dynamic correlation in the HF calculations. Additionally, a chelate configuration (Figure 3.1, structure IV) with both oxygen atoms connected to one Zn atom was investigated. It oriented along the [11-20] direction during the structure optimization. It has a relative energy of  $\Delta E=14.97$  kcal/mol compared to the bidentate Ia. However, a negative force constant was observed in the frequency calculations indicating a saddle point.

For all four structures (bidentate and quasi-bidentate) the vibrational frequencies and their intensities have been calculated. The results are shown in Figure 3.3. The lines represent the peak positions of the vibrational frequencies in the range from  $1300\text{ cm}^{-1}$  to  $1700\text{ cm}^{-1}$ . The height of the lines refers to the intensities. The assignment of the vibrations is indicated for all peaks and observed by analysis of the normal coordinates. Furthermore, the frequency splitting of the symmetric and asymmetric carboxylate stretching vibrations  $\Delta(\nu_{as}-\nu_s)$  are given. For structures Ia, Ib, and IIa the carboxylate frequencies are rather similar and the splitting amounts to  $250\text{ cm}^{-1}$ . Only for structure IIb  $\Delta(\nu_{as}-\nu_s) = 198\text{ cm}^{-1}$  is significantly smaller.

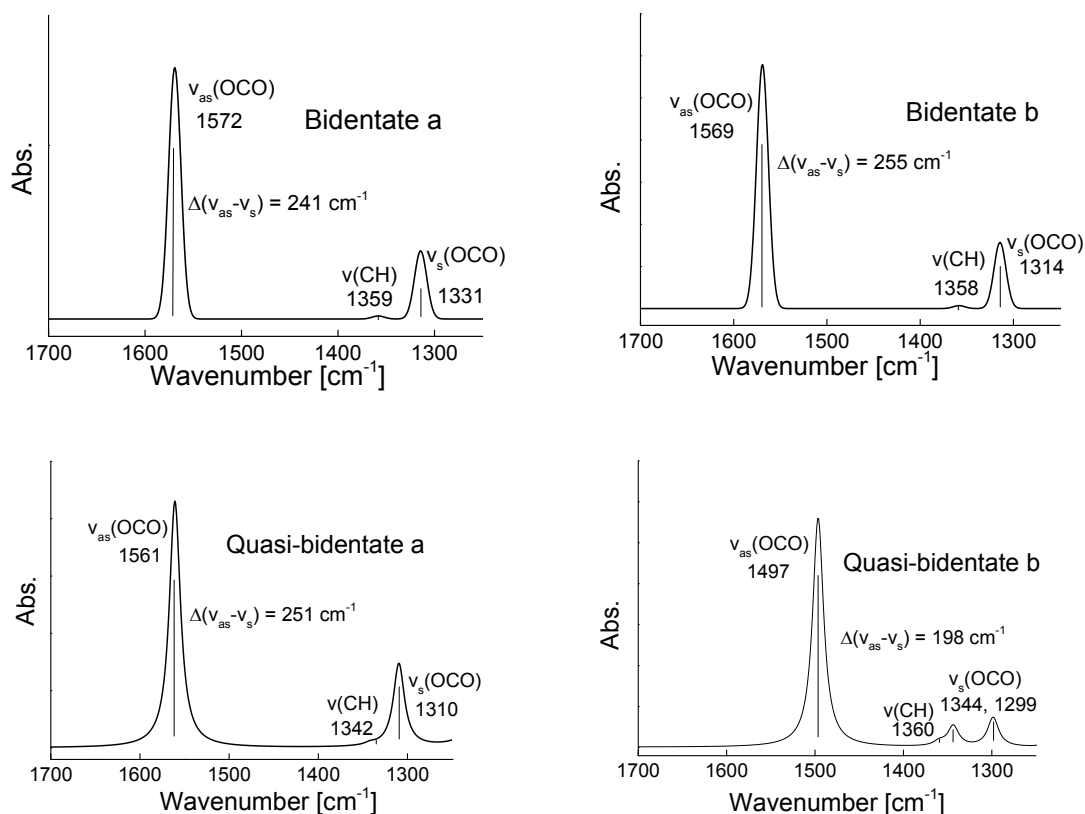


**Figure 3.3** Simulated IR spectra of the four optimized minimum structures

### 3.3.2 Comparison with the experimental data

In the following, we will show that the presence of structure I and structure II together can explain the experimental data.

From infrared reflection absorption spectroscopy (IRRAS) measurements (Table 3.3), formation of formate species on ZnO(10-10) cannot be described by only one adsorption geometry. Consider a formate adsorbs on the surface along [1-210] direction, the  $\nu_{as}(\text{OCO})$  vibration should for an incident beam along [0001] be visible with s-polarized light ( $1570\text{ cm}^{-1}$ ) and the  $\nu_s(\text{OCO})$  vibration with  $p_{n,z}$ -polarized light ( $1373\text{ cm}^{-1}$ ), because of the directions of the transition dipole moments (TDM) (Figure 3.4). However, the positive band seen for  $\nu_{as}(\text{OCO})$  with p-polarized light ( $1573\text{ cm}^{-1}$ ) cannot be assigned to this species.

Therefore the quasi-bidentate structure which is close in energy is additionally considered. For the quasi-bidentate the TDM of  $\nu_{as}(\text{OCO})$  is oriented along the [0001]-

direction (Figure 3.4) and can therefore couple to the  $p_{t,x}$ -component for the light incident along the [0001]-azimuth leading to a positive band. Thus the presence of the two species is fully consistent with the signs of the asymmetric and symmetric stretching bands observed in the experimental data.

**Table 3.3** Assignment of the experimental carboxylate vibrations in dependence of the incident radiation, the polarization and the orientation of the adsorption configuration.

	$\nu_{as}(\text{OCO}) [\text{cm}^{-1}]$		$\nu_s(\text{OCO}) [\text{cm}^{-1}]$	
	$p_{t,x}$	$s$	$p_{n,z}$	
<b>Bidentate</b>	1573		1374	Beam along [1-210]
<b>along [1-210]</b>		1570	1373	Beam along [0001]
<b>Quasi-</b>		1577	1374	Beam along [1-210]
<b>Bidentate along</b>	1589		1373	Beam along [0001]
<b>[0001]</b>				

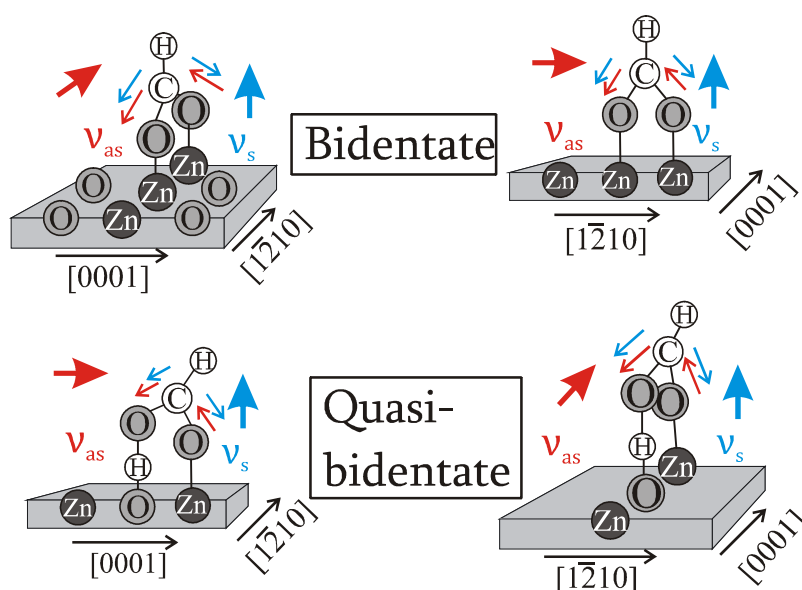


**Figure 3.4** Sketch of the possible adsorption geometries, the quasi-bidentate and the bidentate. Red small arrows show the direction of the asymmetric stretching vibration, the big red arrow indicates the orientation of transition dipole moment (TDM). Blue small arrows show the direction of the symmetric stretching vibration, the blue arrow indicates the orientation of TDM.

Because of the different binding modes, one would expect the frequencies of the  $\nu_s(\text{OCO})$  and  $\nu_{as}(\text{OCO})$  vibrations of the two different formate species to be slightly different. In the DFT calculations, however, the carboxylate frequencies of the bidentate and the quasi-bidentate structures were found to be rather similar (see Figure 3.3). The

wavenumber splitting of the calculated signal amounts to  $\Delta = 241 \text{ cm}^{-1}$  for the most stable configuration of the bidentate and  $\Delta = 251 \text{ cm}^{-1}$  for the quasi-bidentate, respectively. This is slightly higher than the experimental values of  $\Delta = 199 \text{ cm}^{-1}$  [1-210] ( $197 \text{ cm}^{-1}$  [0001]) for the bidentate and  $\Delta = 203 \text{ cm}^{-1}$  [1-210] ( $216 \text{ cm}^{-1}$  [0001]) for the quasi-bidentate. However, the value of the splitting is still characteristic for a bidentate formate [96, 97]. The calculations as well as the experimental data show a larger wavenumber splitting for the quasi-bidentate than for the bidentate, which could be explained by the additional interaction with the proton which is bound to the surface. The calculations indicate that the positions of the hydrogen on the surface have a great influence on the splitting. The effect is more pronounced for  $\nu_s$  (OCO) compared to  $\nu_{as}$  (OCO). For example, the difference of  $\nu_{as}$  (OCO) for bidentate (a) and (b) is negligible, however, for  $\nu_s$  (OCO) it is  $17 \text{ cm}^{-1}$ . To investigate the influence of the H position on the IR spectra, we put the hydrogen as far away from the formate as it was possible within the chosen supercell and obtained  $1571 \text{ cm}^{-1}$  and  $1333 \text{ cm}^{-1}$  for  $\nu_{as}$  (OCO) and  $\nu_s$  (OCO), respectively. The differences are within  $2 \text{ cm}^{-1}$  compared to bidentate *a*, however, a blueshift of  $19 \text{ cm}^{-1}$  is observed for bidentate *b*, which has an enhanced interaction between the surface OH species and the formate.

### **3.3.3 Comparison of embedded cluster and plane wave calculations for the adsorption of formic acid on ZnO**

The aim of this part is to examine the performance of different approaches, e.g. plane wave calculations with periodic boundary conditions and embedding cluster methods. We checked the convergence of structural parameters as well as vibrational frequencies with different parameters influencing the results of the calculations. For the calculations with the periodic boundary conditions these are the size of the unit cell, the cut off energy of the plane waves and the number of k-points and the degrees of freedom considered in the numerical frequency calculations. For the embedded cluster approach it is the size of the quantum cluster, the details of the embedding scheme, and the basis sets for the different atoms. A further aspect in the embedded cluster calculations is how much the choice of the electronic structure method influences the calculated binding

energies. For this purpose we compared the binding energy of FA adsorption on ZnO (10-10) obtained by HF-SCF, DFT with gradient corrected PBE functional, the hybrid functional B3LYP, and the wavefunction based MP2 method.

### 3.3.3.1 Embedding schemes for ZnO

In the embedded cluster calculations, the total system is split into three parts: a fully quantum mechanically treated inner quantum cluster, effective core potentials to avoid artifacts due to an unphysical attraction of electrons by bare positive point charges, and a finite array of point charges to simulate the Madelung field. Several different approaches have been developed to include the Madelung potential in embedded cluster schemes. Here, we apply two different approaches. a) the periodic electrostatic embedded cluster method (PEECM) [54]. The method divides the point charges in the surrounding of QM cluster into a near-field (NF) and far-field (FF) parts, Coulomb interaction within NF region is include and FF region employs multipole expansions(PFMM) [55, 56]. b) a point charge filed extended from unit cell by Evjen procedure [57]. The method originally eliminates the dipole moment of the unit cell by distributing the corner and face atoms over all equivalent symmetry points, thus rapid convergence is guaranteed. Later works [50, 51, 58] extended this method by adding artificial fractional charges at the borders of the unit cell in order to eliminate lowest multipole moments. With the extension of the unit cell to a large point charge field, the fractional charges at all inner boundaries are cancelled, only fractional charges at the outmost borders left. The total number of point charges was about 57440.

In the first step, we investigated how the two different embedding schemes and the size of the quantum cluster influence the binding energies. Therefore we constructed a point charge field with ideal bulk structure. The structure is described by the lattice constants of the hexagonal unit cell,  $a=3.250$  and  $c=5.207$ . The charges at the Zn and O positions were set to  $+2.0$  and  $-2.0$ . Given the surface situation, the point charge array is a two-dimensional slab with a finite thickness. The interaction of the ZnO cluster with a molecule on the surface is expected to converge quickly with the number of layers in the point charge slab. Stodt and Haettig [53] tested the convergence of adsorption

energy of  $N_2$  on the  $TiO_2$  surface with number of layers in the point charge slab at HF/SVP level, already with three layers the result is converged within 0.1 kJ/mol. The binding energy in our case does not change between six and eight layers. We chose eight layers for all calculations to make sure we are on the safe side.

We used four different clusters for testing the embedding schemes, see Fig 3.5. The positions of the clusters were kept fixed, however, the structures of the adsorbed molecule was optimized at PBE level. The binding energies for all clusters obtained with the two different embedding schemes are listed in Table 3.4. The two embedding schemes, PEECM and PCF, always yielded rather similar results. With extension of the cluster size, the binding energy (without counterpoise correction) is decreasing significantly. Though the counterpoise correction is quite large, in particular for the small clusters, the BSSE corrected binding energies are less sensitive to cluster size. The results for the  $Zn_{36}$  and  $Zn_{90}$  cluster are in reasonable agreement and therefore, all further cluster calculations are performed for the  $Zn_{36}$  cluster.

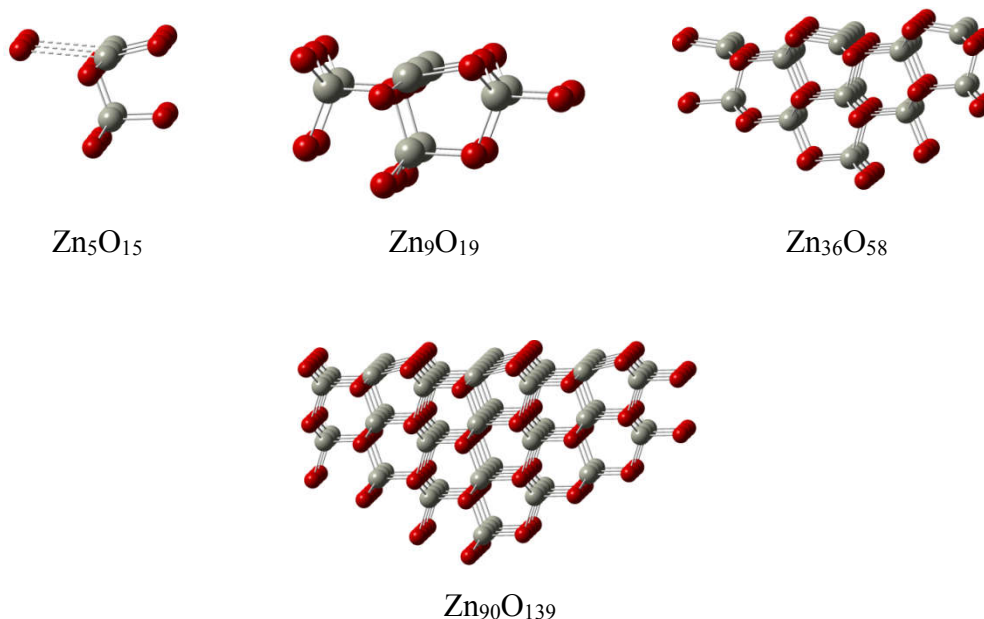


**Figure 3.5** Structure of the four quantum clusters  $Zn_5O_{15}$ ,  $Zn_9O_{19}$ ,  $Zn_{36}O_{58}$ , and  $Zn_{90}O_{139}$

**Table 3.4** Cluster size convergence study with PEECM and PCF schemes. All energies are given in kcal/mol.

Cluster size	PEECM			PCF		
	$E_{BE}$	BSSE	$E_{BE}(CP)$	$E_{BE}$	BSSE	$E_{BE}(CP)$
Zn5	-52.96	-34.64	-18.32	-53.28	-35.02	-18.26
Zn9	-41.23	-26.17	-15.06	-41.60	-26.23	-15.37
Zn36	-37.90	-17.63	-20.27	-38.15	-17.63	-20.52
Zn90	-35.39	-15.94	-19.45	-35.71	-16.00	-19.71

### 3.3.3.2 Convergence of the plane wave calculations

The unit cell for the plane wave calculation was chosen in the same way as in section 3.2.1, i.e. a hexagonal unit cell with  $a = 3.282 \text{ \AA}$ ,  $c = 5.291 \text{ \AA}$ . The starting configurations for the (10-10) surface unit cells with increasing number of surface layers were cleaved from the bulk optimized ZnO wurtzite structure, and a vacuum layer of  $10 \text{ \AA}$  inserted in the z direction (Figure 3.2). In order to determine which size of surface cell is required to reach convergence for the binding energy of formic acid, super cells of different sizes were constructed. The corresponding binding energies are



listed in Table 3.5. In these calculations, only the topmost three atomic layers are relaxed and the gamma point approximation was applied. With respect to the number of ZnO layers convergence was reached with 6 layers. In the further calculations 8 layers are used for staying consistent with the embedded cluster calculations. The difference in the binding energies between the 3x2 and 4x2 supercells is within 1 kcal/mol. Similar accuracy was obtained by Gao et al. [98] for the binding energies of a urea molecule on a ZnO surface. Thus, a 3x2x8 super cell containing 96 atoms is used in all further calculations. In the super cell calculations, structure relaxation was taken into account for all atoms except the bottom oxygen layer. With the optimized structures, the influence of the cutoff energy and the number of k-points was investigated. Only single point calculations were performed for optimized FA@ZnO and super cell of ZnO, with variables of cutoff energy and K-points respectively. As seen in Table 3.6, with a large super cell, k-points have a negligible effect on binding energy, as well as cutoff energy larger than 350 eV.

**Table 3.5** Binding energies of HCOOH on ZnO (1010) surface with different super cell size with Gamma approximation, cutoff 400 eV

Cluster size	3x2x4	3x2x6	3x2x8	3x2x10	2x2x8	3x2x8	4x2x8	4x3x8
BE	-66.53	-41.89	-42.47	-42.65	-43.39	-42.47	-41.94	-41.44

**Table 3.6** Binding energies of HCOOH on ZnO (1010) surface with the changes of cutoff energy (in eV), and k-points settings, single point calculations based on optimized structures

Cutoff energy	350	375	400	425	450	475	500
BE	-42.88	-42.81	-42.65	-42.72	-42.73	-42.54	-42.62

K-points	1x1x1	2x2x1	3x3x1	4x4x1	5x5x1
BE	-42.47	-41.66	-41.61	-41.62	-41.62

### 3.3.3.3 Structural relaxation of the surface

For the ZnO (10-10) surface, the atoms are arranged in rows comprising anion–cation dimers. While all bulk atoms have a tetrahedral coordination of the other atom type, the surface atoms are only threefold coordinated by one surface atom and two next layer atoms. The surface reconstruction has been investigated by several experimental and theoretical methods. A summary can be found in Table 1 of ref. [99]. All studies found an inward relaxation of the surface atoms. However, for the size of this relaxation significant differences were observed. Early LEED studies [82, 100] showed movements of the Zn and O surface atoms inwards by up to  $-0.45 \pm 0.1$  Å and  $-0.05 \pm 0.1$  Å, respectively, while Jedrecy et al. [101] determined from grazing incidence XRD that the Zn atoms only change by  $-0.06 \pm 0.02$  Å and the O atom by  $-0.12 \pm 0.06$  Å, indicating that Zn may sit a bit higher on the surface. In our plane wave calculation, the surface Zn atoms relaxed inwards by  $-0.36$  Å, while the O atoms move up by  $0.01$  Å, resulting in a buckling of the surface layer and tilting of the Zn–O bond by  $11.10^\circ$  with respect to the surface plane. The ZnO bond length shortens by  $0.12$  Å to  $1.87$  Å. These changes are generally consistent with the majority of the previous theoretical work [99, 102], which indicates a buckling of the surface atoms and shortening of the Zn–O surface bond. For the second layer, the deviation from bulk positions is within  $0.1$  Å, and the surface relaxation has only a negligible effect on third and further layers.

For the generation of the embedded cluster models used in the further cluster calculations, we fixed the surface Zn and O positions to an inward relaxation of  $-0.4$  Å and  $-0.1$  Å, respectively. The starting structure of the quantum clusters as well as the positions of the embedding point charges and ECPs were obtained as cut-outs from the relaxed surface structure. We then optimized the positions of inner atoms of the quantum cluster at PBE level. Only the positions of those atoms which are directly coordinated to an ECP were fixed, all other atoms of the cluster are allowed to relax. Similar to the results of the plane wave calculations a surface Zn atom buckling in z-direction of  $-0.30$  Å and  $-0.32$  Å was observed for PEECM and PCF schemes respectively.

### 3.3.3.4 Comparison of the binding energies

Starting from the relaxed surface structure, the adsorption geometries of the bidentate and quasi-bidentate structures were optimized using DFT and the PBE functional. The binding energy of bidentate on the relaxed surface of the Zn<sub>36</sub> cluster amounts to -39.80 kcal/mol and -39.54 kcal/mol for PEECM and PCF schemes, respectively. Compared to the unrelaxed cluster the binding energy increased by ~20 kcal/mol. To study the influence of the DFT functional and of dynamic correlation on the binding energy, we compared different methods. The results are listed in Table 3.7. Again, the BSSE plays an important role for the binding energies. The strongest effect is observed for MP2 and amounts to 28.17 kcal/mol. When the basis set is increased to def2-TZVP, the BSSE correction is significantly decreased.

All methods yielded larger binding energies for the bidentate structure compared to the quasi-bidentate. Comparing the same method, the plane wave calculations and the embedded cluster approach agree within a few kcal/mol. Compared to HF-SCF, the binding energy drops with other methods, ~15.5 kcal/mol for PBE, ~12.2 kcal/mol for B3LYP, and ~11.5 kcal/mol for MP2. To account for the larger basis set demands for correlated wave function methods, we replaced the SVP basis set at the inner part of the quantum cluster by TZVP for the bidentate configuration. The MP2 result for the adsorption energy on the relaxed Ti<sub>36</sub> cluster with TZVP basis set is -45.06 kcal/mol, which is very close to the SVP result. This means that the SVP basis set is sufficient for the description of the adsorption process on cluster surfaces. The differences between the DFT functionals are rather small. The change is 1.3 kcal/mol between PBE and B3LYP for the bidentate structure and 1.2 kcal/mol for the quasi-bidentate structure, which gives a relative energy difference of 0.1 kcal/mol. Nakatusji et al. [8] computed binding energies of almost ~-80 kcal/mol for both structures by a very limited Zn<sub>40</sub> cluster at MP2 level with double-zeta quality basis set, which is not large enough for describing the system. However, we assume that the biggest part of the difference is caused by surface relaxation and BSSE.

Another non-negligible contribution to the binding energy comes from the change of

the zero-point vibrational energy (ZPVE) upon adsorption. For the optimized structures, we obtained zero point vibrational energy of 1.76 and 1.42 kcal/mol for the bidentate and quasi-bidentate from the harmonic frequencies.

**Table 3.7** Binding energies with different configurations and methods.

	Bidentate			Quasi-bidentate		
	$E_{BE}$	BSSE	$E_{BE}(CP)$	$E_{BE}$	BSSE	$E_{BE}(CP)$
HF	-67.28	-12.24	-55.04	-49.13	-8.66	-40.47
PBE	-58.90	-19.36	-39.54	-46.87	-13.43	-33.44
MP2	-71.72	-28.17	-43.55	-56.35	-21.34	-35.01
B3LYP	-60.30	-17.44	-42.86	-47.13	-12.24	-34.89
MP2(TZVP)	-53.53	-8.47	-45.06			
PBE(PBC)			-41.61			-33.74
PW91(PBC) <sub>13</sub>			-42.91			-34.94
HF(PBC) <sup>11</sup>			-52.4			-40.7
MP2(Zn <sub>4</sub> O <sub>4</sub> ) <sup>8</sup>	-79.8			-79.6		

### 3.3.3.5 Structures and Frequencies

To identify the accuracy of the different approaches, harmonic frequencies of formic acid and formate anion were calculated based on equilibrium structures with localized basis sets and plane waves, the latter restrained in a 10\*10\*10 Å cell. The results are listed in Table 3.8. We noted that the calculated frequencies from localized Gaussian basis sets are size dependent, and only a def2-TZVP basis set is sufficient for describing the neutral FA molecule and a large def2-QZVP basis set is needed to approach the experimental data for the formate anion. The  $\nu_{as}(OCO)$  vibration mode still differs by as much as 24  $cm^{-1}$  between the def2-QZVP, and the def2-TZVP result. For the Plane waves calculations a cutoff energy of 400 eV was large enough in all calculations.

**Table 3.8** calculated and experimental vibrational frequencies of FA and Formate anion by localized basis sets and plane waves with different cutoff energies.

	Localized basis sets			Plane waves			Exp. [103, 104]
	SVP	TZVP	QZVP	300	400	500	
<b>HCOOH</b>							
O-H str.	3589	3583	3600	3473	3601	3607	3570
C-H str.	2955	2965	2962	2928	2981	2968	2943
C=O str.	1814	1765	1760	1719	1759	1758	1770
C-O str.	1114	1079	1076	1071	1071	1072	1105
<b>HCOO<sup>-</sup></b>							
C-H str.	2268	2415	2439	2449	2478	2457	2449
V <sub>as</sub> (OCO)	1761	1648	1624	1570	1616	1610	1622
V <sub>s</sub> (OCO)	1328	1299	1293	1266	1295	1297	1309
Δ(v <sub>as</sub> -v <sub>s</sub> )	433	349	331	304	321	313	313

Results for the structures and the vibrational frequencies of the two adsorption structures (bidentate and quasibidentate) on ZnO(10-10) are summarized in Table 3.9 and Table 3.10, respectively.

The geometry parameters obtained by PBC and EC approaches are rather similar. However, the splitting number between v<sub>s</sub>(OCO) and v<sub>as</sub>(OCO) with PBC and EC schemes for bidentate structure differs by up to ~30 cm<sup>-1</sup>. While the results for the symmetric mode are very similar there are deviations in the asymmetric mode. We ascribe the difference to the basis sets insufficiency (only the def2-SVP basis set was used in the cluster calculations)). Another disagreement between the two approaches can be observed in the C-H bending mode; however, the intensities of this vibration are negligible. The hybrid functional calculation agrees well with the PBE results. Within the PEECM scheme the difference in the splitting is 5 cm<sup>-1</sup> for bidentate structure. When a scaling factor of 0.9679 [105] was applied for B3LYP, the splitting decreased by ~10 cm<sup>-1</sup>.

**Table 3.9** Comparison of geometry parameters of bidentate and quasi-bidentate with different embedding schemes at PBE level.

	Bidentate			Quasi-bidentate		
	Zn-O	O <sub>sur</sub> H...O	∠OCO	Zn-O	O <sub>sur</sub> H...O	∠OCO
PEECM	1.96/2.01	2.62	128.9	1.96	1.48	127.9
PCF	1.97/2.01	2.73	129.3	1.97	1.51	128.2
PBC	1.98/2.02	2.82	129.0	1.96	1.52	127.6

**Table 3.10** Calculated vibrational frequencies (cm<sup>-1</sup>) and intensities (%) by different approaches with experimental values.

	Bidentate				Exp.	Quasi-bidentate			
	PEECM	PCF	PBC	B3LYP <sup>1</sup>		PEECM	PCF	PBC	Exp.
V <sub>s</sub> (OCO)	1334	1335	1326	1384(1340) <sup>2</sup>	1374	1326	1321	1310	1373
Intensity	(22.5)	(29.8)	(23.9)	(30.4)		(6.5)	(8.1)	(7.5)	
V <sub>ben</sub> (CH)	1376	1385	1351	1429(1383)		1366	1348	1341	
Intensity	(2.7)	(2.6)	(1.4)	(5.6)		(0.6)	(0.4)	(0.1)	
V <sub>as</sub> (OCO)	1607	1615	1572	1650(1597)	1573	1571	1570	1562	1589
Intensity	(80.8)	(89.9)	(100)	(100)		(19.4)	(20.6)	(22.8)	
Δ(v <sub>as</sub> -v <sub>s</sub> )	273	280	246	266(257)	199	245	249	250	216

<sup>1</sup>with PEECM scheme; <sup>2</sup>with scaling factor of 0.9679.

### 3.4 Conclusion

In this chapter, the results of theoretical calculations on the adsorption of formic acid on ZnO (10-10) are used to assign different adsorption sites by comparison of the experimental IRRAS data and the calculations. According to the analysis of the frequencies, formic acid adsorbs in a dissociated form, i.e. as formate anion accompanied by a surface OH group on the mixed-terminated ZnO (10-10) surface. Adsorption is possible in two different orientations, which are perpendicular to each other. The bidentate structure which is oriented along the [11-20] direction is most

stable based on the DFT calculations. A quasi-bidentate, oriented along [0001], is found at slightly higher energies. If these two orthogonal orientations are considered, the intensities in the IRRA spectra are comprehensible.

Furthermore, the applicability of plane wave calculations and embedded cluster calculations for the adsorption of formic acid on ZnO (10-10) was investigated. While the structural parameters and binding energies obtained with the embedded cluster calculations with an SVP basis set and the plane wave calculations are rather similar, the deviations in the calculated frequencies can be of the order of  $50 \text{ cm}^{-1}$ . The agreement of PBC and EC calculations became much better when the basis set in the EC calculations was increased. If one aims for higher level binding energies than those obtained at DFT level, a systematic approach is to perform an optimization of the surface structure with PBC first. Surface relaxation can then be considered for the construction of the embedding either by a point charge field with compensation of multipole moments or with PEECM. The adsorption geometries and local structure relaxations are reasonably described in the EC calculation. Here, hybrid functionals or MP2 calculations are easily affordable.

## 4 NO Adsorption on rutile $\text{TiO}_2(110)$ surface: role of oxygen vacancies

### 4.1 Introduction

The adsorption of molecules on rutile  $\text{TiO}_2(110)$  surface has attracted much attention for various surface related applications such as catalysis, solar cells, and sensor technology [106, 107]. Oxygen vacancies ( $\text{O}_v$ ) are common in reducible metal oxides and alter the geometric and electronic structure as well as well as chemical properties of the system [108]. For example, the CO-stretching frequency in the vicinity of an oxygen vacancy differs by  $10\text{cm}^{-1}$  from the one measured for the adsorption on perfect parts of the surface [109]. In principle, removal of a neutral surface oxygen leads to two remaining electrons in the oxide. The so-called F-center, a vacancy site filled with 2 ( $\text{F}^0$ ), 1 ( $\text{F}^{1+}$ ) or 0 ( $\text{F}^{2+}$ ) electrons, is directly or indirectly responsible for many of the material's properties, such as optical adsorption and luminescence spectra, photocatalysis reactivity, and conductivity [13-15]. Scheme of rutile  $\text{TiO}_2(110)$  surface and a bridge oxygen vacancy site is illustrated in Figure 4.1.

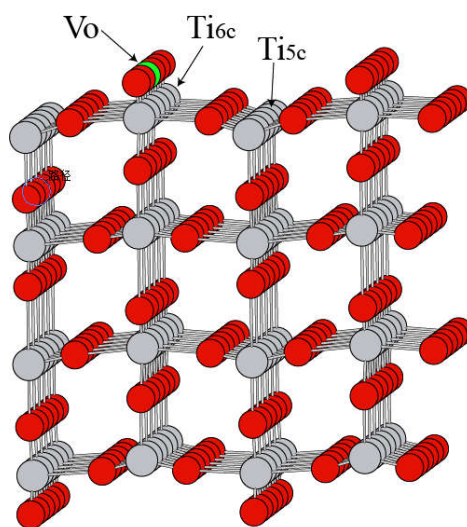


**Figure 4.1**  $\text{TiO}_2$  rutile (110) surface and a bridge oxygen vacancy



The description of bridge oxygen vacancies at rutile  $\text{TiO}_2$  (110) surface is not yet fully satisfactory. It is well known that density functional theory (DFT) methodologies [28, 29] using the local spin density approximation (LSDA) and in the generalized gradient approximation (GGA) have deficiency on electron localized systems, because of Coulombic self-interaction error, which stabilize solutions with delocalization of spin density [110]. With an oxygen vacancy on surface, the defect state could go over conduction band by normal DFT calculations and lead to delocalization of unpaired electrons across several Ti sites with no appreciable formation of distinct  $\text{Ti}^{3+}$  centers [111]. Two common methods to overcome this problem are hybrid exchange-correlation functionals, which is very expensive in supercell approach within periodic boundary conditions (PBC), and on-site correlation (DFT+U) method [47, 112], which is U value dependent. Hybrid functional calculations [113, 114] showed it was possible to localize the electrons to form  $\text{Ti}^{3+}$  centers with one at a five-coordinated surface site and the other adjacent to the  $\text{O}_v$ , or both at the neighbors of  $\text{O}_v$  [115]. Defect states is found to be near 1 eV below conduction band, agrees to experiments. DFT+U approach adds little computational efforts and gives similar results with hybrid functionals with the “precise” U value. Chretien et al. [116] found out unpaired electrons stay delocalized after optimization procedure if the U value is less than 2 eV; Similarly, Morgan et al. [111] pointed out for U larger than 4.2 eV, the calculations allows the recovery of the experimentally observed gap state.

Another issue addressed in literatures from both experiment and theory is different solutions of localization positions [116-119]. Employing certain localization procedures, different localizations of possible  $\text{Ti}^{3+}$  pairs within the first three layers have been compared by DFT+U [116, 119] and hybrid functionals [120]. The conclusions agree to that polarons [118, 121], an excess electron can be trapped by a local lattice distortion around a Ti ion, migrate near the surface region with low migration energy barriers. However, the localization on the two Ti ions adjacent to the oxygen vacancy is extremely unfavorable. A molecule dynamic study [122] also performed on the distribution of UPEs, and over 65% localize on the subsurface layer. We are more interested in the influence of adsorption properties such as adsorption

energies and vibrational frequencies by different excess electron localizations. Chretien et al. [116] examined the adsorption of an Au atom on a defective surface with bridge oxygen vacancy. The Au atom is electrophilic and takes electrons from the surface, and the binding energies change as much 0.7 eV with different localization solutions. Nitric oxide (NO) is chosen here because of widely technological applications, such as NO gas sensor and pollution control [123], and also because of the unpaired  $\pi_p^*$  electron on NO may have interactions with excess electrons on the surface. In turn, the coupling interactions may provide useful information for locating the excess electrons on the surface. The chemisorption properties of NO on the oxidized (defective free) surface have been investigated using both experimental and theoretical methods, including large super cell approach and embedding cluster approach [124-128]. The reductive (defective) surface is also investigated by Sorescu et al. [129] with normal GGA functional, however, the localization of  $Ti^{3+}$  centers is not considered.

In this section, four localized  $Ti^{3+}$  pairs, namely  $Ti_{6c^*}$  pairs,  $Ti_{6c5c}$  pairs,  $Ti_{5c}$  pairs and  $Ti_{sub5c}$  pairs, have been considered by periodic boundary condition calculations and embedding cluster calculations. The influence of oxygen vacancies on the adsorption of NO on the rutile  $TiO_2$  (110) surface is investigated. For four different distributions of the two excess electrons the influence on the adsorption properties of NO such as adsorption energies and vibrational frequencies is investigated.

## **4.2 Computational details**

### **4.2.1 Calculations with Periodic boundary condition (PBC)**

The first part of the calculations was performed with the Vienna ab initio Simulation Package (VASP) [77-79]. The PBE functional was used in all calculations. The projector-augmented wave (PAW) method [42] is applied to describe the wavefunctions in the core regions, while the valence wavefunctions are expanded as linear combination of plane-waves with a cutoff energy of 550 eV. In the geometry optimizations of the bulk cell of  $TiO_2$ , the total energy was converged to  $10^{-5}$  eV and

the Hellmann-Feynman force on each relaxed atom was less than  $1 \text{ meV}\text{\AA}^{-1}$ . The on-site correction has been applied to the 3d electron of Ti atoms by the approach due to Dudarev et al. [47], with the  $U_{\text{eff}}$  value set to 4.2 eV [116, 119, 120]. The equilibrium lattice constants ( $a = 3.285 \text{ \AA}$ ,  $c = 5.297 \text{ \AA}$  and the internal parameter  $u = 0.3793$ ) are similar to other theoretical results [120] and agree well with the experimental values ( $a = 3.2496 \text{ \AA}$ ,  $c = 5.2042 \text{ \AA}$  and  $u = 0.3819$ ).

Based on the optimized bulk cell and lattice constants, the surface calculations were performed using a slab model, consisting of four stoichiometric layers (one oxygen row and one Ti-O row), followed by a vacuum layer with a width of  $10 \text{ \AA}$ . The positions of all atoms were optimized, until the Hellmann-Feynman forces converged to  $0.01 \text{ eV}\text{\AA}^{-1}$ . The  $\text{TiO}_2(110)$  surface was modeled by a  $5 \times 2$  supercell (Figure 1). Because of the large unit cell, the  $\Gamma$ -point approximation was used.

Removal of a bridge oxygen atom from the supercell produces an oxygen vacancy concentration of 10% on the surface. Different distributions of the excess electrons were enforced by the scheme proposed by Chretien et al. [116]. To localize the electrons at the targeted sites, we chose two Ti sites and expanded the distance to the neighboring oxygen atoms by  $0.1 \text{ \AA}$ . In this way, the electron repulsion from the neighboring oxygen ions is reduced. This enables localization of the excess electrons on the chosen sites. In the following structure relaxation the excess electrons remain at these sites.

#### 4.2.2 Embedded Cluster calculations

All cluster calculations were carried out using the TURBOMOLE program package [87]. The periodic electrostatic embedded cluster method (PEECM) (see section 2.4) is employed, and the nominal charges of +4.0 for Ti and -2.0 for O were used. The positive point charges closest to the quantum cluster are fixed and have been augmented with large ( $18e^-$ )  $\text{Ti}^{4+}$  core potential [130] to avoid artefacts. To model the  $\text{TiO}_2(110)$  surface, we used a  $\text{Ti}_{25}\text{O}_{81}$  cluster (see Figure 2). The relaxed surface structure was taken from the periodic DFT slab calculations in the previous section. Only small part of the cluster (Figure 2) is reoptimized at B3LYP/def2-SVP level. The structure optimizations on the quantum cluster and the cluster with adsorbed NO

molecule were performed with the def2-SVP [91] basis set and the B3LYP functional [35, 131], which provide good results for binding energies and frequencies for NO adsorption on TiO<sub>2</sub>(001) surface. We calculated the binding (or adsorption) energies according to the expression

$$E_{BE} = -[E_{tot} - (E_{TiO_2} + E_{NO})]$$

Harmonic frequencies were obtained based on the optimized structures. The hessian matrix and dipole gradients by numerical differentiation of the gradients [132]. For comparison with experimental spectra, the vibrational frequencies computed with the B3LYP functional are scaled with a factor of 0.92 [125] to correct for the errors of the method and the harmonic approximation.

### 4.2.3 Band gap and on-site correction

The band gaps, calculated with different methods and models, are listed in Table 4.1. As expected, HF overestimates the band gap by a factor of four, while the band gap is underestimated with the PBE functional. In the VASP calculations PBE yields a band gap of 1.77 eV for PBC calculation, which is below the experimental value of 3.1 eV. The hybrid functionals, HSE and B3LYP, show in the PBC calculations good agreement with the experimental band gap. When applying the Hubbard-U in combination with the PBE functional, the band gap increases, and the result is U dependent. When applying the Hubbard-U, the band gap increases, with increasing U. The band gaps (1.8 eV to 2.5 eV) obtained with a U value in the range from 0 to 6 eV () remains well below its experimental value. However, with U values larger than 4.2 eV, strong localization with the excess electrons from the bridge oxygen vacancy was found. We perform our PBC calculations with U=4.2 eV in the following. The trends for the dependence of the band gap on the different methods are similar in the embedded cluster calculations. However, several additional factors influence the band gap (HOMO-LUMO gap) in the embedded cluster calculations: a) cluster size, small clusters usually give larger band gaps; b) point charges for embedding environment, use of nominal charges of 4.0 for Ti and -2.0 for O yield larger band gaps compared with smaller charges, +3.0 and -1.5 for example [53, 114].

Table 4.1 Calculated band gaps (HOMO-LUMO gaps for EC) of rutile TiO<sub>2</sub> using different methods, the values are given in eV.

	HF	PBE	PBE+U (U=4.2)	HSE (0.2 HF)	B3LYP
PBC	12 [133]	1.77 [115]	2.21 [134]	3.05 [115]	3.4 [113]
EC	11.95	2.10			3.85
Exp.			3.1 [135]		

## 4.3 Results and discussion

### 4.3.1 Defect free surface

In the PBC calculations, the ideal rutile TiO<sub>2</sub> (110) surface is modeled with a 5x2 supercell, and all atomic positions within the supercell allow to relax. According to the PBE+U calculations the following reconstruction of the surface was observed: The oxygen bridge (Ob) – Ti<sub>6c</sub>- sub Ti<sub>6c</sub> rows show an outward displacement of 0.24-0.44-0.39 Å, respectively. The next threefold-coordinated oxygen row also moves 0.32 Å out of the surface. However, the Ti<sub>5c</sub> row stays more or less at the original place with a displacement of only -0.04 Å. The results agree with other theoretical works and LEED data (Table 3 in [107]). Shibuya et al. [120] found some difference between PBE+U and HSE06 (25% HF exchange) with a 4x2 supercell. With HSE06 the overall displacement of the ions is an inward relaxation, whereas with PBE + U it is an outward displacement.

Based on the optimized supercell structure obtained with PBE+U, an embedded cluster model was set up. It consists of a Ti<sub>25</sub>O<sub>81</sub> quantum cluster and an interface layer of 46 titania ECPs. Ionic charges of Ti and O for the embedding have been tested in literatures. Rittner and coworkers [58] found an optimal Ti charge of +2 by comparing binding energies of N<sub>2</sub> on rutile TiO<sub>2</sub> (110) surface between a Ti<sub>9</sub>O<sub>18</sub> cluster and hydrogen saturated cluster of similar composition Ti<sub>9</sub>O<sub>25</sub>H<sub>14</sub>. Stodt et al. [53] studied the convergence of the N-Ti bond distance and the adsorption energy at the HF-SCF/SVP

level with different cluster sizes, and charges of +3.0 for the cations and  $-1.5$  for the anions has been chosen. We apply formal charges of Ti(+4) and O (-1) for our calculations as recommended by Ammal and Heyden [136], since with formal charges the HOMO-LUMO gap agrees better with the band gap in periodic GGA calculations. Only the inner part of the quantum cluster is reoptimized at B3LYP level (see Figure 4.2), thus the cluster approach with B3LYP shows similar results. The relaxed atoms show displacements within  $0.1 \text{ \AA}$  compare to PBE+U results, the two central Ti<sub>6c</sub> atoms of the cluster inward to the bulk by  $-0.05 \text{ \AA}$ .

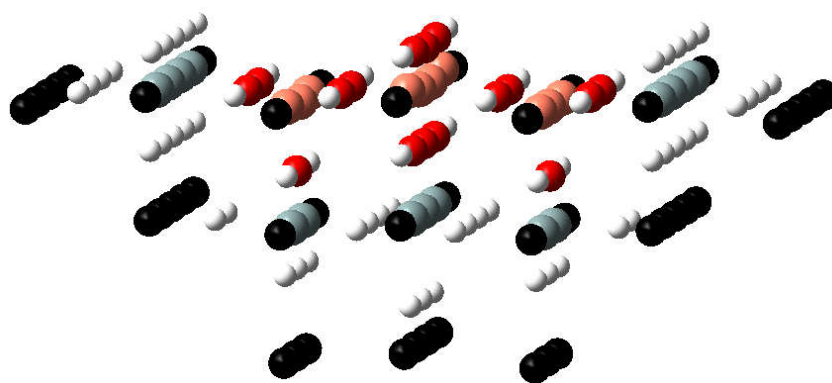


**Figure 4.2** Model for the (110) rutile surface:  $Ti_{25}O_{81}(Ti_{46} \text{ ECP})$  cluster. The geometry is based on the optimized PBE+U structure obtained in the slab calculation. The inner part of the quantum cluster (the Ti atoms shown in pink and the oxygen atoms shown in red) is reoptimized at B3LYP level. The small white and big grey balls represent fixed oxygen and titanium, black ones are the titania ECP at the interface between quantum cluster and embedding.

### 4.3.2 Modeling of oxygen vacancies

For the investigation of the oxygen vacancies one neutral oxygen atom was removed from a bridge position on the surface with two excess electrons of the  $O^{2-}$  ion remaining in the system. In case that the electronic structure is determined with PBE+U ( $U=4.2$ ) without any initial distortion of the geometric structure, the two unpaired electrons are localized in the surface Ti<sub>6c</sub> row at the direct neighbors of the vacancy site. This positions are denoted as Ti<sub>6c\*</sub> in the following. Due to the missing oxygen ion, a local

reconstruction of the vacancy occurs. Compared to the perfect surface, the two  $\text{Ti}_{6c^*}$  ions move down by  $0.13\sim 0.20$  Å and the oxygens below the  $\text{Ti}_{6c^*}$  sites show a displacement of  $0.1$  Å.

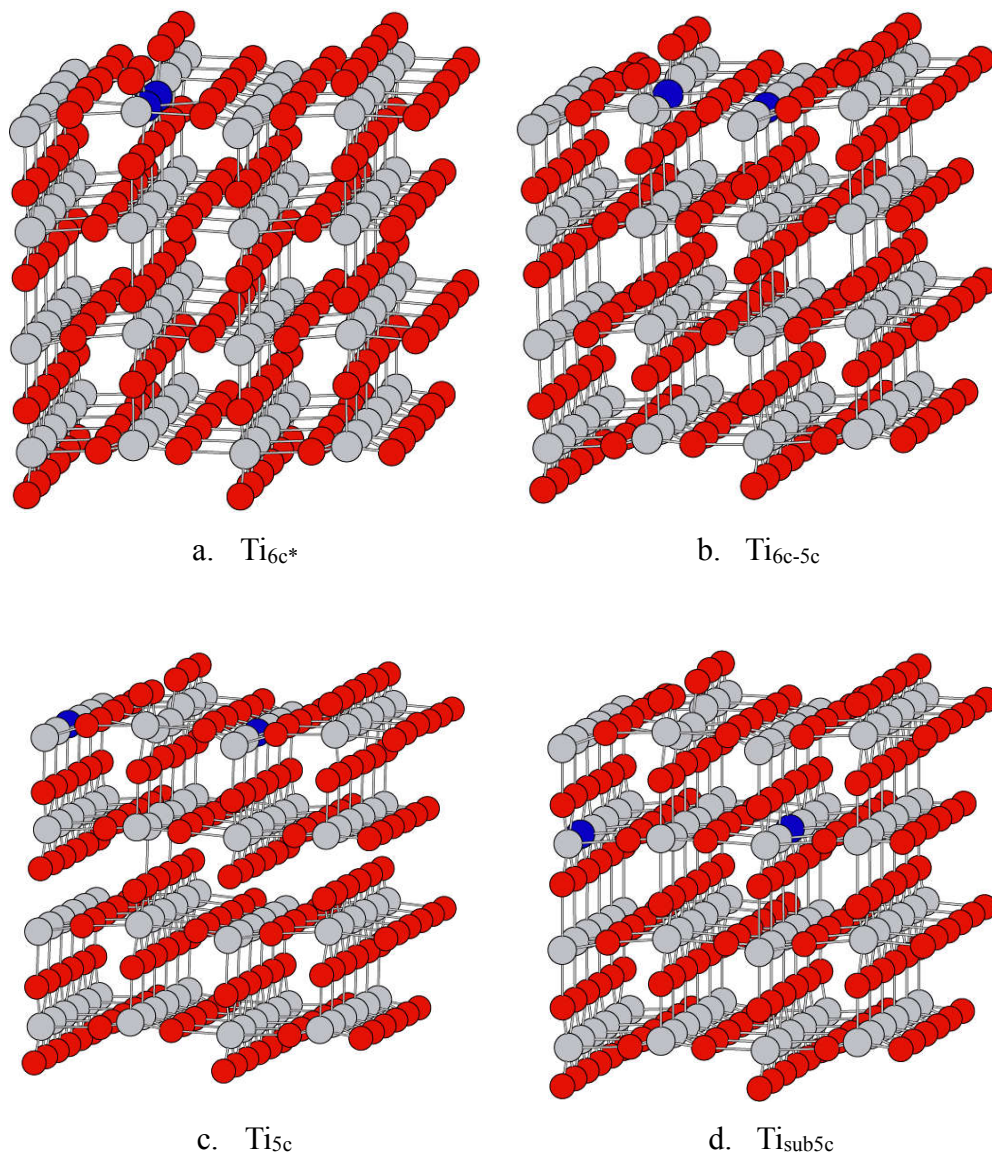


**Figure 4.3** Four different localizations of the  $\text{Ti}^{3+}$  centers, optimized structures at PBE+U level,  $\text{Ti}^{3+}$  are shown in blue, grey and red circles represent Ti and O.

Many other local minima on the potential energy surface of the reduced oxide have been reported in the literature [116, 119, 120, 122]. Besides the  $\text{Ti}_{6c^*}$  localization (Figure 4.3a), we enforced localization of the excess electrons in three other configurations. One is the configuration obtained by Di Valenti et al. [113] and Bredow et al. [114] which is the standard solution for hybrid functionals. In this configuration two unpaired electrons are located at different lattice sites, one is on  $\text{Ti}_{6c^*}$  and the other on the neighbor  $\text{Ti}_{5c}$  row we term this configuration as  $\text{Ti}_{6c5c}$  (Figure 4.3b). The next is the lowest energy configuration obtained by Deskins et al. [119] with DFT+U and Shibuya et al. [120] with DFT+U and hybrid functionals. This configuration corresponds to that two electrons are localized on the subsurface of  $\text{Ti}_{5c}$  rows, which is named as  $\text{Ti}_{\text{sub}5c}$  (Figure 4.3d). The third one is another low energy configuration obtained by Deskins et al. [119], that two  $\text{Ti}^{3+}$  centers stay at surface  $\text{Ti}_{5c}$  rows, termed as  $\text{Ti}_{5c}$  (Figure 4.3c). The creation of  $\text{Ti}^{3+}$  sites lead to local geometry distortions, where the bond lengths between  $\text{Ti}^{3+}$  and neighboring oxygens is extended within a range of 0~ 0.15 Å. As Shibuya et al. [120] pointed out, we also noted in our calculations that if a free electron occupies one of the t2g-type d orbitals of a  $\text{Ti}^{3+}$  center, bond extensions occur only for those bonds which are in the same plane as the occupied d orbital with maximum bond distortions of 0.15 Å (Table 4.2). The other neighboring oxygen atoms are changed by less than 0.01 Å.

**Table 4.2** lattice distortion for the four configurations, unit is in Å.

	Maximum bond distortion	Minimum bond distortion
$\text{Ti}_{6c^*}$	0.09	0.04
$\text{Ti}_{6c-5c}$	0.12	0.02
$\text{Ti}_{5c}$	0.11	0.02
$\text{Ti}_{\text{sub}5c}$	0.15	0.01

The energies of the different localizations of the  $\text{Ti}^{3+}$  centers are summarized in Table 4.3. In the PBE+U calculations, the results agree to other PBC calculations [119, 120,



122]. The localization at subsurface  $\text{Ti}_{5c}$  centers has the lowest energy and the localization on the Ti atoms adjacent to the vacancy is unfavorable in energy. In the next step we compared to embedded cluster calculations. The quantum cluster is shown in Figure 4.2. A limitation for the embedded cluster method is the treatable cluster size and the number of atoms that can be considered in the structure relaxation. For the  $\text{Ti}_{\text{sub}5c}$  structure, we therefore fixed the subsurface Ti atoms and most of the neighboring oxygen atoms based on the structural parameters obtained by the PBE+U calculations. Thus, the energy of  $\text{Ti}_{\text{sub}5c}$  configuration can be expected to be lower. However, assuming that the geometry distortion only has influence on the local region of neighboring oxygen atoms, which means that the relaxed region in Figure 4.2 is large enough for the surface localizations, energy differences between the different solutions are negligible at B3LYP level with the def2-SVP basis set.

**Table 4.3** Relative energies (in eV) with respect to  $\text{Ti}_{6c^*}$  localization with different methods.

	$\text{Ti}_{6c^*}$	$\text{Ti}_{6c-5c}$	$\text{Ti}_{5c}$	$\text{Ti}_{\text{sub}5c}$
PBE+U (PBC)	0.00	-0.28	-0.56	-0.71
Deskins [119]	0.00	-0.68	-1.27	-1.55
B3LYP (EC)	0.00	0.05	-0.09	-0.02

### 4.3.3 NO adsorption on the perfect surface

The binding mechanism of NO on the perfect surface is well established and investigated by quantum chemical calculations. In the NO molecule the singly occupied  $\pi_p^*$  orbital is polarized to the N atom and thus the N-orientation adsorption (N towards the surface) is stronger than the O-orientation adsorption [125, 129]. In the following, only N-orientation will be considered. To distinguish the difference between unpaired electron localization on  $\text{Ti}_{5c}$  site and adsorption  $\text{Ti}_{5c}$  site, we use  $\text{Ti}(5c)$  for later case. The nitrogen atom of NO attaches to the  $\text{Ti}(5c)$  atom of the surface with a distance of 2.56 Å and a tilting angle between NO and the surface, which allows an interaction of the  $\pi_p^*$  orbital of NO and the  $d_{z^2}$  orbital of  $\text{Ti}(5c)$  (Figure 4.4). This is proven by Arndt

et al. [128] by varying the distance coordinate and the polar angle between NO and Ti(5c) using an embedded cluster approach and restricted open shell MP2. Our cluster calculations yield binding energies of 0.39 eV, which agrees well with the calculations of Haettig et al. [125] on a  $\text{Ti}_{40}\text{O}_{80}$  and with experimental value [129]. A detailed comparison of the geometry parameters and binding energies is listed in Table 4.4.

**Table 4.4** Geometry parameters and binding energies with different approaches, comparison with experimental values.

	Ti-N (Å)	N-O (Å)	$\angle\text{TiNO}$ (°)	BE (eV)
B3LYP(EC) [125]	2.49		130	0.36
ROMP2(EC) [128]	3.00		144	0.57
PW91(PBC) [124, 129]	2.46	1.16	127.6	0.35
B3LYP (EC)	2.56	1.14	133.4	0.39
Exp. [124]				0.39

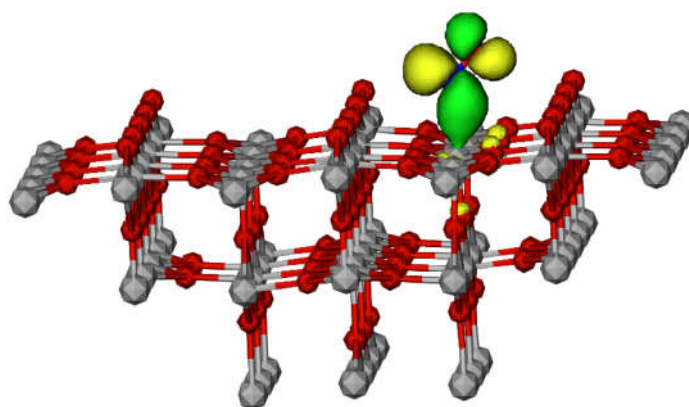


**Figure 4.4** Single occupied  $\pi_p^*$  orbital for NO adsorbed on the rutile  $\text{TiO}_2$  (110) surface. Tilted structure, isovalue was set to 0.04.

#### 4.3.4 NO adsorption at the $\text{V}_\text{o}$ site

In the following, we investigated the adsorption of NO at the oxygen vacancy for different types of localizations of the excess electrons. Still, the N-orientation towards the surface is energetically more favorable than with the O-orientation [129]. We first analyzed the NO adsorption at the oxygen vacancy site with  $\text{Ti}_{6c^*}$  localization. We

noticed a charge transfer process from one of the  $\text{Ti}_{6c^*}$  atoms to the  $\text{NO } \pi_{2py}^*$  orbital and a ground triplet state is formed on the NO molecule. The remaining unpaired electron on the other  $\text{Ti}_{6c^*}$  atom is coupled anti-ferromagnetically with the two electrons on the NO molecule. Then the total system shows a low spin state, which is 0.11 eV more stable than quartet spin state. The calculated bond length of Ti-NO is 1.93 Å with an upright configuration (Figure 4.5), and the adsorption energy is 1.72 eV, agree well with a value of 1.93 Å for bond length and 1.59 eV for the adsorption energy from Sorescu et al. [129]. A charge transfer process is observed for the other three excess electron localizations as well, even for the  $\text{Ti}_{\text{sub}5c}$  localization with fixed volume extension. The explanation is that the orbital hybridization between two  $\text{Ti}_{6c^*}$  atoms and NO lowers the  $\text{NO } 2\pi_p^*$  orbital energy, and then the driving force for electron transfer from the surface to the NO molecule adsorbed on a vacancy site increases. However, the coupling between the one excess electron distributed on the two  $\text{Ti}_{\text{sub}5c}$  atoms with the two unpaired electrons on the NO molecule is weak, because of the long distance, 3.6 Å from a  $\text{Ti}_{5c}$  site and 8.8 Å from a  $\text{Ti}_{\text{sub}5c}$  site. The adsorption energy for NO on the vacancy site with  $\text{Ti}_{\text{sub}5c}$  localization amounts to 1.20 eV, which is ~0.52 eV smaller than for  $\text{Ti}_{6c^*}$  localization with strong electron coupling.

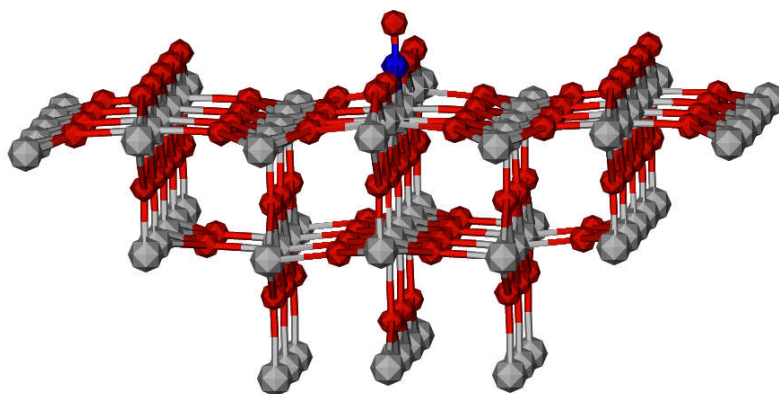
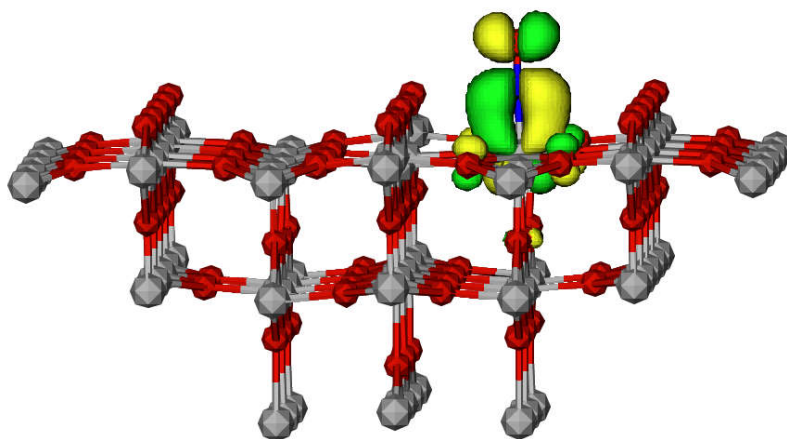


*Figure 4.5 Adsorption structure of NO on bridge oxygen vacancy site.*

### 4.3.5 NO adsorption at the $\text{Ti}(5c)$ site

Sorescu et al. [129] noticed a strong influence on the adsorption properties at  $\text{Ti}(5f)$

sites, adsorption energy increased by about 0.44 eV for a Ti-NO orientation. It is worth noticing that the NO is almost perpendicular to the surface, and spin state changes from triplet state (two unpaired electrons from oxygen vacancy) to a doublet. Similarly, Li et al. [137] found out that the NO adsorption energy increase about 0.2 eV on a hydroxylated surface, because of a transfer of charge from the surface to the molecule. In our cluster calculations, two solutions are found depending on the starting geometry structures. Adsorption structures, binding energies and vibrational frequencies from different excess electron localizations are listed in Table 5. We first analyzed the NO adsorption at Ti(5c) site with  $Ti_{5c}$  localization, because one of the localized  $Ti^{3+}$  center is close to the NO molecule. First, we start with a tilted structure as obtained on the perfect surface, and we obtain a tilted configuration after geometry optimization. The adsorption energies with different excess electron localization are similar to those obtained on the perfect surface (Table 4.5), which means that the excess electrons have no influence on the adsorption properties in the case of NO. Next, we start with an upright structure. After geometry optimization, Ti (5c) moves out of the surface by 0.26 Å, the distance between NO and Ti (5c) thus shortens to 1.93 with an upright configuration of NO on the surface. In the second upright configuration, adsorption energy decreases by about 0.2 eV compared with tilted structure. A charge transfer process is observed with upright structure from  $Ti^{3+}$  center to NO  $2\pi_p^*$  orbital, a  $NO^-$  anion is thus formed on the surface with a triplet state, orbital schemes of two singly occupied  $2\pi_p^*$  orbitals can be seen in Figure 4.6.



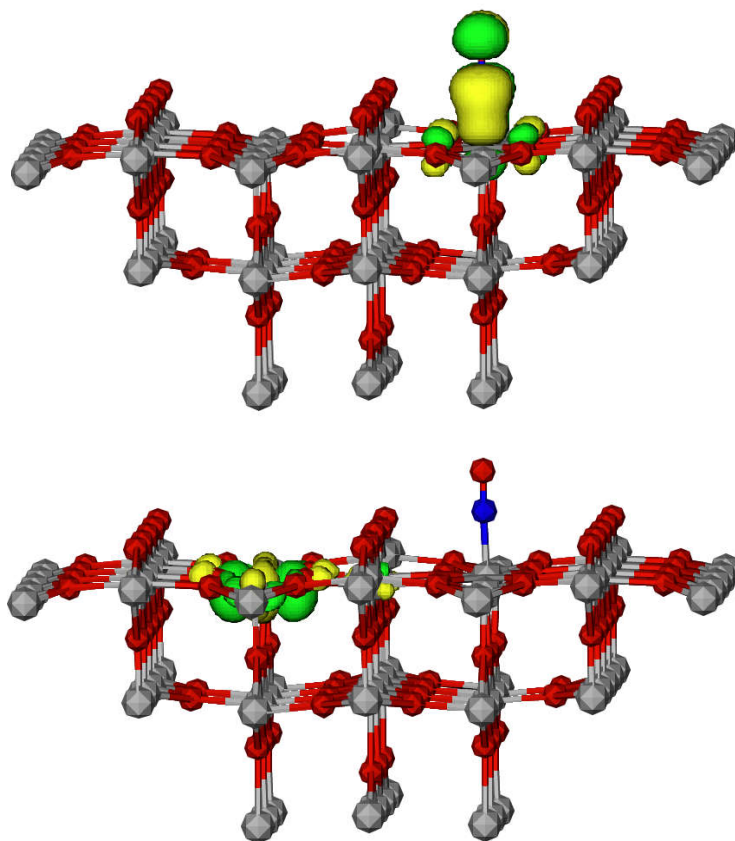


*Figure 4.6 Three singly occupied orbital schemes for NO adsorption on a reduced surface with  $Ti_{5c}$  localization, isovalue is set to 0.04.*

**Table 4.5** NO binding energies (in eV) and stretching frequencies (in  $\text{cm}^{-1}$ ) on the perfect and the defective rutile  $\text{TiO}_2$  (110) surface.

Adsorption site	UPE localization	Adsorption geometry	Binding energy	Freq
Ti(5c)	defective free	tilted	0.39	1897 <sup>1</sup>
Vo	Ti <sub>6c</sub> *	upright	1.72	1461
Vo	Ti <sub>sub5c</sub>	upright	1.20	
Ti(5c)	Ti <sub>6c</sub> *	tilted	0.38	1898
Ti(5c)	Ti <sub>5c</sub>	tilted	0.38	
Ti(5c)	Ti <sub>sub5c</sub>	tilted	0.35	1902
Ti(5c)	Ti <sub>6c</sub> *	upright	0.50	1736
Ti(5c)	Ti <sub>6c5c</sub>	upright	0.50	1736
Ti(5c)	Ti <sub>5c</sub>	upright	0.58	

<sup>1</sup> 1893  $\text{cm}^{-1}$  from Stodt et al. [125] with  $\text{Ti}_{40}\text{O}_{80}$  cluster, 1873  $\text{cm}^{-1}$  from experiments [125, 127].

### 4.3.6 NO stretching frequency

For the optimized structures, the vibrational frequencies of NO have been calculated numerically. The values are listed in Table 4.5. The scaling factor of 0.92 is determined as ratio between the experimental gas phase frequency of an NO molecule and the calculated value obtained at the B3LYP/def2-SVP level in the harmonic approximation [125].

The stretching frequency of NO on the perfect surface is  $1889\text{ cm}^{-1}$  and agrees with calculations for a  $\text{Ti}_{40}\text{O}_{80}$  cluster experimental data [125-127]. On the reduced surface, the NO molecule can strongly bind to a vacancy site and form a  $\text{NO}^-$ . Thus the stretching vibration of  $\text{NO}^-$  shows a blue shift of  $428\text{ cm}^{-1}$  from NO in gas phase. However, this has so far not been observed experimentally. There are two possible explanations. On the one hand, NO can form dimers on the surface; on the other hand, frequencies below  $1700\text{ cm}^{-1}$  are not always considered in the experiments [126, 127]. From ultra-high vacuum Fourier transform infrared spectroscopy (UHV-FTIRS) results [125-127], it was found that three main bands at  $1875$ ,  $1750$  and  $2243\text{ cm}^{-1}$  were observed on both fully oxidized and reduced  $\text{TiO}_2(110)$  surfaces at low NO coverage. The three bands are attributed to the presence of three surface species, NO,  $(\text{NO})_2$  and  $\text{N}_2\text{O}$ , respectively. The only difference is that the negative bands at  $1875$  and  $1750\text{ cm}^{-1}$  observed for oxidized samples became positive for reduced  $\text{TiO}_2(110)$ , whereas the  $\text{N}_2\text{O}$  band at  $2243\text{ cm}^{-1}$  remains negative.

We continued with NO adsorption at the Ti(5c) site on a reduced surface. Two local minima structures were found, and the adsorption energy difference is 0.2 eV. For the first tilted structure, the unpaired electrons are well localized on the Ti atom sites and do not participate in the adsorption process. Accordingly, the frequency does not change much (within  $10\text{ cm}^{-1}$ ). In the upright configuration, one electron is transferred to NO inducing a shift of about  $162\text{ cm}^{-1}$  to  $1736\text{ cm}^{-1}$ , compare to tilted structure.

## 4.4 Conclusion

Four different localized solutions of two excess electrons created by a bridge oxygen vacancy on rutile  $\text{TiO}_2$  (110) surface, namely  $\text{Ti}_{6c^*}$  pairs,  $\text{Ti}_{6c5c}$  pairs,  $\text{Ti}_{5c}$  pairs and  $\text{Ti}_{\text{sub}5c}$  pairs, have been considered by periodic boundary condition calculations and embedded cluster calculations. Our PBE+U ( $U=4.2$  eV) results agree to other super cell calculations with GGA+U and hybrid functionals, the subsurface sites are preferred,  $\text{Ti}_{5c}$  solution is close in energy and sites directly adjacent to the oxygen vacancy are unstable. Our B3LYP calculations with embedded cluster method, on other hand, show that the energy difference between  $\text{Ti}_{5c}$  and  $\text{Ti}_{6c^*}$  is negligible. Therefore, the  $\text{Ti}_{6c^*}$  localizations cannot be rule out.

On a defect free surface, NO prefers to adsorb on the surface at a Ti(5c) site with an N-orientated tilted structure. On a reduced surface, the most active site for NO adsorption is the vacancy site, and the adsorption energy is calculated to be 1.72 eV. The two excess electrons locate at the vacancy site, where one of the electrons is transferred to NO to form a triplet  $\text{NO}^-$  and the other is coupled anti-ferromagnetically with  $\text{NO}^-$ . For this configuration, the NO stretching frequency shows a shift of  $400\text{ cm}^{-1}$  from NO in gas phase. Two local minima structures were found with NO adsorption at the Ti(5c) site. For the first tilted structure, the unpaired electrons are well localized on the Ti atom sites and do not participate in the adsorption process. Accordingly, the adsorption energy and frequency do not change much compared to NO on the defect free surface. In the upright configuration, however, one electron is transferred to NO and the adsorption energy increase 0.2 eV compare to the tilted structure, also the frequency has a blue shift of  $170\text{ cm}^{-1}$ .

The results from NO adsorption on reduced surface show that the coupling interaction between NO radical and excess electrons is either so strong when the NO adsorbs on the vacancy site, that the electronic configuration is completely changed; or so small when NO adsorbs on the Ti(5c) site, that have no influence on the NO. Therefore, NO adsorption cannot be used to obtain information on the localization of the excess



electrons.

## 5 Applications on materials with magnetic centers

### 5.1 CO adsorption on the Fe-terminated $\alpha$ -Fe<sub>2</sub>O<sub>3</sub>(0001) surface

#### 5.1.1 Introduction

Iron oxides are widely used in catalysis due to their availability, low toxicity, and price [6, 138]. Here, we are interested in the adsorption of carbon monoxide (CO) on the (0001) surface of hematite,  $\alpha$ -Fe<sub>2</sub>O<sub>3</sub>, because CO plays an important role in catalytic reactions on both metal and metal oxide surfaces. For example, the oxidation of CO to carbon dioxide (CO<sub>2</sub>) is a good solution to solve such serious environmental problem [139, 140].

In  $\alpha$ -Fe<sub>2</sub>O<sub>3</sub>, the Fe centers are in the oxidation state +3, they have a 3d<sup>5</sup> occupation and are in a distorted octahedral environment. They are in a high spin configuration with a local spin of  $S=5/2$ . The experimentally measured magnetic moments are  $\sim 4.6$ - $4.9 \mu_B$  per atom [141, 142]. Below the Neel temperature,  $T_N=955$  K [143],  $\alpha$ -Fe<sub>2</sub>O<sub>3</sub> is an anti-ferromagnetic insulator showing weak ferromagnetism above the Morin temperature,  $T_M=260$  K, due to a slight canting of the two sublattice magnetizations [144, 145].

The geometric, electronic and magnetic structure of hematite is well investigated by quantum chemical calculations. As discussed for rutile TiO<sub>2</sub>, density functional theory with local density approximation (LDA) and generalized gradient approximation (GGA) underestimates the band gap by 40% (chapter 3). In the case of iron containing systems, FeO for example [146, 147], the system is predicted with DFT as metallic, while it behaves as Mott insulator experimentally. For hematite, DFT gives an energy gap of 0.5 eV and a magnetic moment of  $3.4 \mu_B$  per atom [148] which is too small when compared to experimental value of 2 eV. The LDA/GGA band gap and magnetic moments can be corrected using DFT+U. This method requires an empirical parameter, the Hubbard U. Rollmann et al. [149] concluded that best overall agreement, with respect to experimental photoemission and inverse photoemission spectra of hematite, is achieved for  $U=4$  eV. Dzade et al. [150] suggested a U value of 5 eV, which provides

a good description of the band gap of 2.1 eV and yields a magnetic moment for Fe of  $4.23 \mu_B$  per atom. We apply DFT+U where U is set to be 5 eV for the Fe 3d electrons for the calculations in this section.

In contrast to LDA and GGA calculations, the Hartree-Fock (HF) method significantly overestimates the band gap. Hybrid functionals which contain a fractional amount of exact HF exchange are capable to approximately describe the experimental band gap. The percentage of HF exchange, similar to Hubbard U, can be used as an empirical parameter as well. A screened hybrid functional with 12% exact HF exchange is obtained by Pozun et al. [151] to yield a band gap that is in accordance with experimental observations. However, calculations with periodic boundary condition for large unit cells are rather time consuming when hybrid functionals are applied. Therefore, DFT+U calculations are performed to investigate the adsorption of CO on the (0001) surface of  $\alpha$ -Fe<sub>2</sub>O<sub>3</sub>.

### 5.1.2 Computational details

All calculations are based on spin polarized density-functional theory (DFT) [28-31] and were performed with the Vienna ab initio Simulation Package (VASP) [77-79]. The generalized gradient approximation with the functional described by Perdew, Burke, and Ernzerhof [35, 131] (GGA-PBE) was used. Only the valence orbitals of Fe (3d4s) and O (2s2p) were taken into account. The projector-augmented wave (PAW) method [42, 43] is applied to describe the wavefunctions in the core regions, while the valence wavefunctions are expanded as linear combination of plane-waves with a cutoff energy of 550 eV. The convergence of the total energy with the cutoff energy was checked up to 800 eV. The differences are within 3 meV/atom.

The hexagonal unit cell consists of 12 iron atoms and 18 oxygen atoms (Figure 1). For optimization of ion positions and the unit cell volumes, the Brillouin zone integration is performed using Monkhorst-Pack grids [44]. K-point grids with a 7x7x3 mesh for relaxations and a 14x14x6 mesh for the calculation of densities of states (DOS) were used. Partial electronic densities of state were calculated by projecting the plane-wave components of the orbitals onto their spherical harmonic components within atomic

spheres.

The effect of the on-site Coulomb repulsion of Fe 3d electrons was considered by the Dudarev approach [47, 152] with the effective parameter  $U_{\text{eff}} = 5$  eV. The surface structures were modeled by a 2x2x1 super cell, which contains 48 irons and 72 oxygen atoms, assuming that the interaction between the CO molecules is negligible. A vacuum layer of 17Å was included to avoid interactions between the slabs. All atoms including adsorbates and super cell were allowed to relax until the residual forces on all atoms converged within 0.01 eV/Å. The K-point grid was set to 3x3x1 for super cell integration.

The free CO molecule was simulated in a 10Å x 10Å x 10Å sized cell using  $\Gamma$ -point approximation. All other parameters were chosen identical to the ones as the surface calculations.

### **5.1.3 Results and Discussion**

#### **5.1.3.1 Bulk $\alpha$ -Fe<sub>2</sub>O<sub>3</sub> Structure**

The hematite structure contains iron and oxygen atoms arranged in a trigonal-hexagonal structure with space group R-3c and lattice parameters  $a = b = 5.035$  Å,  $c = 13.747$  Å [153], with six formula units per unit cell. The complete hexagonal unit cell of hematite is shown in Figure 5.1.1, together with the rhombohedral primitive cell. The electronic properties will be the same at each iron site, because all iron atoms have an equivalent octahedral environment. The arrangement of the Fe cations produces pairs of FeO<sub>6</sub> octahedra that share edges with three neighboring octahedra in the same plane and one face with an octahedron in an adjacent plane.

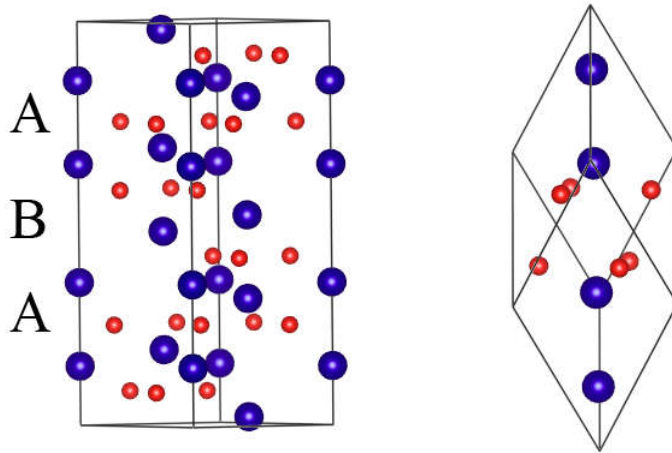


Figure 5.1.1 Schematic illustration of the hexagonal unit cell (left) and the rhombohedral primitive cell (right) of  $\alpha\text{-Fe}_2\text{O}_3$ . Color scheme: Fe = blue and O = red.

From the rhombohedral primitive, we note that there are two types of pairs of Fe atoms. There are two characteristic distances between neighboring Fe ions along the hexagonal axis. According to the definition by Rollmann et al. [149] the shorter Fe-Fe distance is defined as type A and the larger as type B. The arrangement of the oxygen anions and the high-spin ( $d^5$ ) iron cations naturally affects the orientation of the iron atoms' spin magnetic moment and thus the observed bulk magnetic properties of hematite. Detailed differences of energy and magnetic moments between several electronic solutions can be found in ref. [149]. We follow the ground state which found in ref. [149] that type A pairs have opposite magnetic moments, while Fe atoms belonging to type B pairs have equal magnetic moments. Comparison of lattice constants, geometries and magnetic moments between our results and other theoretical works and experiments are listed in Table 5.1.1.

**Table 5.1.1** Structural parameters for  $\alpha$ -Fe<sub>2</sub>O<sub>3</sub> and magnetic moments obtained with different theoretical methods and experiments. Magnetic moments (MM) are in  $\mu_B$ , and distances are in  $\text{Å}$ .

	Reference	a	c	MM	Fe-Fe (A)	Fe-Fe (B)
PBE+U (5 eV)	This study	5.078	13.878	4.23	2.872	4.067
PBE+U(4 eV)	[154]	5.067	13.879	4.14		
PW91+U(4 eV)	[148]	5.067	13.882	4.11	2.896	4.044
HF	[155]	5.112	13.820	4.74	2.877	4.033
LSDA	[156]			3.72		
PW91	[148]	5.007	13.829	3.44	2.929	3.998
PBE	[151, 157]			3.60	2.95	3.99
HSE(12%)	[151]			4.16	2.94	4.00
Exp.	[141, 153, 158]	5.035	13.747	4.6-4.9	2.88	3.98

We obtained a magnetic moment of  $4.23 \mu_B$  for each iron, which is consistent with other DFT+U calculations and higher than common DFT results. This observation is explained by the increasing repulsion on the Fe-sites as the U-value increases, the O 2p and Fe 3d hybridization is substantially reduced by the strong on-site repulsion. Consequently, the lattice parameters get bigger with increasing U-value. However, by increasing the U-value, Canepa et al. [157] observed that the volume of the rhombohedral cell expands beyond the experimental value. If the HF exchange considered in the DFT functional is increased to 50%, the cell volume matches the experimental one. This is also reflected in the bond distances which are decreasing with higher HF exchange.

The total density of states (DOS) calculated for bulk  $\alpha$ -Fe<sub>2</sub>O<sub>3</sub> structure as well as the contributions of the Fe 3d bands and O 2p bands are shown in Figure 5.1.2. The occupied states near the Fermi level are mainly composed of the O 2p states with a small contribution of the Fe 3d states, and the conduction band is dominated by Fe 3d states, suggesting that  $\alpha$ -Fe<sub>2</sub>O<sub>3</sub> is an O 2p - Fe 3d insulator. The gap between the highest states below the Fermi level and the states with the lowest states above the Fermi level is determined to approximately 2.5 eV.

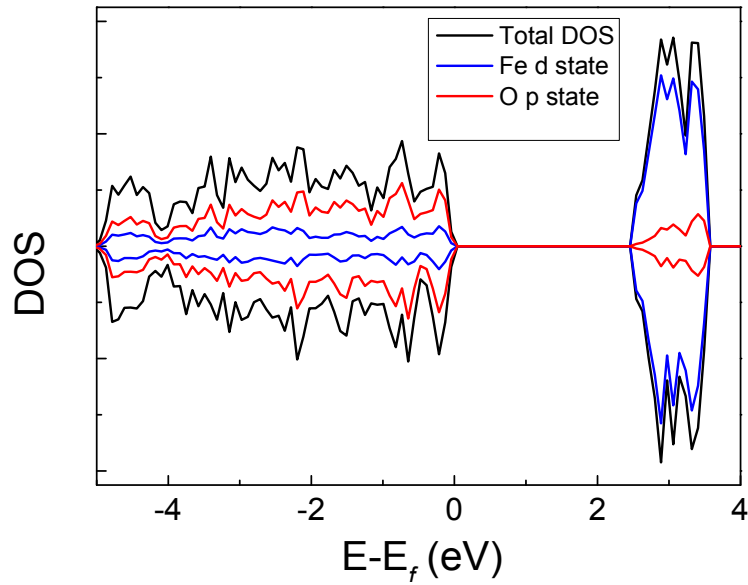


**Figure 5.1.2** Density of states (DOS) of bulk  $\alpha$ -Fe<sub>2</sub>O<sub>3</sub> with PBE+U calculation.

### 5.1.3.2 Model surface

The  $\alpha$ -Fe<sub>2</sub>O<sub>3</sub> (0001) surface, one of the predominant growth surfaces, has been subject to intensive studies, due to its importance in catalysis. Unraveling the relationship between the atomic surface structure and other physical and chemical properties of metal oxides is challenging due to the mixed ionic and covalent bonding often found in metal oxide systems. In the hematite case, three different surface terminations are possible when the crystal is cleaved perpendicular to the (0001) direction. There is a single-Fe-terminated surface, a double-Fe-terminated and an O-terminated surface. Single-Fe-terminated surface is determined to be the most stable one among them when comparing surface energies, oxygen terminated surface is also suggested under condition of high oxygen pressure. [149, 154, 159, 160]. In the meantime, mixed surfaces are also suggested both experimentally and theoretically [161, 162]. In this study, we have considered only the non-polar single Fe-termination where the top and side views are schematically shown in Figure 5.1.3.

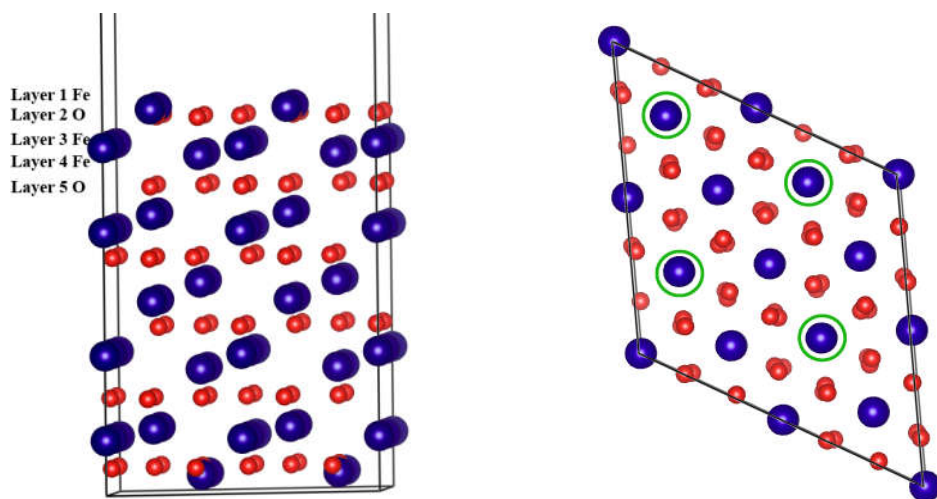


**Figure 5.1.3** Side (left) and top (right) views of the single-Fe-terminated  $\alpha\text{-Fe}_2\text{O}_3$  (0001) surface, terminating irons are marked with green circles in the top view.

The anti-ferromagnetic ordering of bulk hematite is retained at the (0001) surface. The magnetic moments of the surface layer Fe atoms ( $3.97 \mu_B$ ) is substantially reduced compared to the bulk Fe atoms ( $4.23 \mu_B$ ). The change in the coordination of the surface atoms compared to those in the bulk modifies the O 2p and Fe 3d hybridization, which consequently affects the local magnetic moments [150, 154].

As a characteristic of most metal oxide surfaces, strong surface relaxation has also been found for the single-Fe-terminated surface. The largest relaxation effects are the reduction of the Fe-O distance between the two top layers, due to the electrostatic effects characteristic for the surface. In Table 5.1.2, we summarize the optimized interlayer distances compared with previous theoretically predicted and experimentally observed ones.



**Table 5.1.2** Optimized first four interlayer distance ( $\text{\AA}$ ) for the single-Fe-terminated  $\alpha\text{-Fe}_2\text{O}_3(0001)$  surface.

Method	Layer 1-2	Layer 2-3	Layer 3-4	Layer 4-5
	Fe-O	O-Fe	Fe-Fe	Fe-O
PBE+U (bulk)	0.88	0.88	0.56	0.88
PBE+U (5 eV)	0.28(-68%)	0.94(+6.8%)	0.36(-36%)	1.02(+16%)
PW91+U (4 eV)[161]	(-66.6%)	(7.2%)	(-38.0%)	(16.3%)
PBE+U(4 eV)[148]	(-57%)	(+9.6%)	(-40%)	(+17%)
PW91+U [150]	0.40(-52%)	0.91 (+8%)	0.45 (-26%)	1.05 (+23%)
GGA[162]	0.36(-57%)	0.90(+7%)	0.46(-23%)	0.97(+15%)
LEED [163]	0.62(-27.4%)	0.87(+3.6%)	0.55(-8.3%)	0.9(+7.1%)
XPD [164]	0.50(-41%)	1.0(+18%)	0.55(-9%)	1.24(47%)

The surface layer relaxation we obtained in the GGA+U calculations agrees to the values obtained by Kiejna et al. [161], however, it differs from other GGA+U results, especially for the top layer. A possible origin for the differences can be the parameter settings. In particular, the cutoff energy was different in the calculations. Kiejna et al. used 450 eV, Rohrbach et al. [148] and Dzade et al. [150] applied 350 and 400 eV respectively. The results of low-energy electron diffraction (LEED) and XPD studies show only qualitative agreement with the results of GGA and GGA+U studies and differ very much in the magnitude of the relaxations, especially for the first four layer distances. They differ also substantially among themselves which may be related to different samples (single crystal or a thin hematite film) and preparation methods.

### 5.1.3.3 CO Adsorption

In the first step, the structure and vibrational frequencies of a free CO molecule were calculated with VASP and the same settings as will be used in the calculations on the adsorbed molecule. A bond length of 1.14  $\text{\AA}$  was obtained which agrees well with the experimental distance of 1.13  $\text{\AA}$ . For the stretch frequency, 2124  $\text{cm}^{-1}$  was obtained

from GGA+PBE, which has to be compared to the experimental value of  $2143\text{ cm}^{-1}$ . The adsorption of CO on metal surfaces has been investigated in details, see ref [165, 166] and references therein. The adsorption of CO on metal surfaces is described by the donor-acceptor model [167] (or Blyholder model). When CO is adsorbed on a metal surface the CO  $5\sigma$ -orbital is significantly hybridizing with the metal d-electrons. This gives rise to a charge transfer from the CO  $\sigma$  orbital to the metal, but the metal also donates charge back into the antibonding  $2\pi^*$ -CO orbital. The back donation from the substrate into the  $2\pi^*$ -CO orbital weakens the bond within the CO molecule and strengthens the bond to the substrate. The weakening of the CO bond induces a red shift (towards lower wavenumbers) of the vibrational frequency [168]. However, CO adsorption on oxide surfaces (NiO for example) can be different. Pacchioni et al. [169] showed that back-donation is negligible for NiO/CO case.

On the single-Fe-terminated surface, the surface iron atom and the three neighboring oxygen atoms form together with the adsorbed CO molecule a tetrahedral configuration. CO is arranged vertically to the surface plane (Figure 5.1.4). The Fe atom moves upward by  $0.26\text{ \AA}$ . The distance between Fe and C is  $2.20\text{ \AA}$ , and the CO bond length stays at  $1.14\text{ \AA}$ . The binding energy, defined as the energy difference between the energy of super cell with adsorbed CO molecule and the energies of the surface super cell and the separately calculated CO, amounts to  $0.53\text{ eV}$ . The adsorption energy of CO on clean metal oxide surfaces,  $0.16\text{ eV}$  for CO@MgO (001) [170],  $0.51\text{ eV}$  for CO@Al<sub>2</sub>O<sub>3</sub> (0001) [170],  $0.53\text{ eV}$  for CO@ZnO (10-10) [171] and  $0.36\text{ eV}$  for CO@TiO<sub>2</sub> (110) [172], is generally weak.

The calculated frequency of the CO stretching vibration shifts from  $2124\text{ cm}^{-1}$  (exp.  $2143\text{ cm}^{-1}$ ) to  $2144\text{ cm}^{-1}$  (exp.  $2173\text{ cm}^{-1}$ ). The blue shift (higher frequency number) of  $30\text{ cm}^{-1}$  with respect to CO gas phase is also found in CO adsorption on other metal oxide surfaces, such as TiO<sub>2</sub>, MgO and NiO [169, 172, 173]. We ascribe the CO vibrational shift toward higher frequencies arises essentially from the repulsion originating when the CO molecule stretches in the presence of the rigid surface (wall effect) [169, 173, 174].

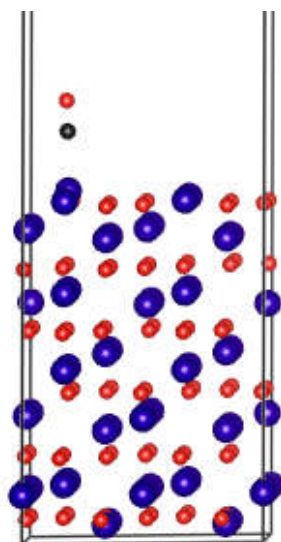


*Figure 5.1.4* CO adsorption geometry on the single-Fe-terminated  $\alpha$ -Fe<sub>2</sub>O<sub>3</sub>(0001) surface

#### 5.1.4 Conclusion

We studied the adsorption of a CO molecule on the  $\alpha$ -Fe<sub>2</sub>O<sub>3</sub>(0001) surface with DFT+U. Our studies reveal that the on-site Coulomb correction on Fe 3d state should be considered, because otherwise the band gap would be underestimated and the magnetic structure could not be properly described. In bulk hematite, there are two types iron interactions, i.e. type A and type B, and type A pairs are coupled anti-ferromagnetically, while type B pairs are coupled ferromagnetically, the whole system shows net magnetic moments. Only the non-polar single Fe-terminated surface is considered in our calculations. On this surface, the CO molecule adsorbs in an upright configuration with adsorption energy of 0.53 eV, which is in line with CO adsorption on other oxide surfaces. The frequency of CO stretching vibration changes from 2124 in gas phase to 2144 cm<sup>-1</sup> on the surface, and it is in good agreement with the experimental values.

## 5.2 Magnetism of inverse spinel copper ferrite: influence of Li intercalation

### 5.2.1 Introduction

Spinel ferrites are commercially attractive and have gained importance due to their high specific capacities [175]. Spinel oxides retain capacity for a large number of cycles due to their robust host structure and show high lithium diffusion rates due to the presence of a three dimensional network of interstitial sites [17]. An interesting feature is that the transition metal centers of these materials can change their oxidations state and magnetic properties during cycling. Thus a reversible control over bulk magnetism via electrochemical processes is proposed with spinel iron oxide, maghemite [19].

In the case of iron oxide spinel, the oxygen atoms are arranged in a face-centered cubic (fcc) sublattice, and tetrahedral hollow sites (A site) and octahedral hollow sites (B site) are occupied by irons with  $\text{Fe}^{2+}$  and  $\text{Fe}^{3+}$  respectively. The Fe ions on A and B sites couple anti-ferromagnetically. It is found that each intercalated Li-ion reduces one of the  $\text{Fe}^{3+}$  cations to  $\text{Fe}^{2+}$  at the octahedral sites, thereby decreasing the total magnetic moment of the system [19]. Since the safe limit of ion-exchange has been found to be around  $1 \mu_B$  per formula unit for intercalated Li-ions, the ideal ferrite systems of interest would be the ones having around one unbalanced/net magnetic moment per formula unit, so that the intercalation of one Li per formula unit may reduce the right number of octahedral  $\text{Fe}^{3+}$  to  $\text{Fe}^{2+}$  to balance the magnetic moments of the anti-ferromagnetically coupled tetrahedral and octahedral sublattices, leading to zero net magnetization. In this way, magnetism control with reversible Li-intercalation can potentially be achieved in a variety of magnetic systems. Necessary requirements would be a) that the material shows a magnetic phase transition near room temperature, so that a complete ferro-to-paramagnetic transition could be induced; b) ferrimagnetic systems with anti-ferromagnetically coupled magnetic sublattices may also possibly be tuned between an anti-ferromagnetic state with zero net magnetization and a ferrimagnetic one with finite magnetization due to Li-intercalation.

In this section, we discuss the influence of reversible Li-intercalation in  $\text{CuFe}_2\text{O}_4$  on the magnetic properties of the material. The systems have been investigated experimentally in the research unit Hahn at the Institute of Nanotechnology at the KIT. Here, the normal and inverse spinel structures of  $\text{CuFe}_2\text{O}_4$  will be investigated based on DFT+U calculations with respect to the exchange coupling constants between the magnetic centers obtained within the broken symmetry approach.

## **5.2.2 Models and Methods**

### **5.2.2.1 Computational details**

All spin polarized density-functional theory (DFT) [28-31] calculations were performed with the Vienna ab initio simulation package (VASP) [77-79]. The generalized gradient approximation with the functional described by Perdew, Burke, and Ernzerhof (GGA-PBE) [35, 131] was used throughout. While the projector augmented wave (PAW) method [42, 43] was applied to describe the wave functions in the core regions, the valence wave functions were expanded as linear combination of plane-waves with a cutoff energy of 500 eV. The unit cell of the spinel lattice contains 56 atoms, the total energy is converged to  $10^{-5}$  eV and the Hellmann-Feynman force on each relaxed atom is smaller than  $0.01 \text{ eV}/\text{\AA}$  in the optimized structures. For optimization of ions positions and unit cell volumes, the Brillouin zone integration is performed using Monkhorst-Pack grids [44]. K-point grids with a  $3 \times 3 \times 3$  mesh for relaxations and a  $6 \times 6 \times 6$  mesh for the calculation of densities of states (DOS) were used.

The on-site Coulomb interactions were included only for the strongly correlated Fe and Cu 3d electrons. The  $U_{\text{eff}}$  value for Fe was kept at 5 eV as in the calculations on  $\text{Fe}_2\text{O}_3$ . For Cu, Feng et al. [176] found that the half-metallic properties (or band gap) of copper ferrite doesn't change if the U value is increased beyond 4 eV, so we set  $U_{\text{eff}}$  for Cu to 4 eV.

### **5.2.2.2 Broken symmetry Approach within DFT**

The magnetic behavior of transition metal oxides can often be described by the interaction of localized spins of the metal d-orbitals referred to as magnetic sites. In

the simplest case, the interaction between two centers with one unpaired electron for each center, the total spin  $S$  is either  $S=0$  for the anti-ferromagnetic coupling or  $S=1$  for a ferromagnetic state. The coupling of the spins can be described by the well-known phenomenological Heisenberg–Dirac–van Vleck (HDvV) Hamiltonian. This Hamiltonian describes the isotropic interaction between two localized magnetic moments  $S_i$  and  $S_j$  as:

$$\hat{H}_{HDvV} = -2J_{ij}S_iS_j$$

where  $J_{ij}$  is exchange coupling constant giving the magnitude and type of interaction between the localized spins  $S_i$  and  $S_j$ . According to the spin Hamiltonian, a positive value of  $J_{ij}$  corresponds to a ferromagnetic interaction, favoring a situation with parallel spins; a negative value represents to an anti-ferromagnetic interaction. The definition of the spin Hamiltonian is not unique, in part of the literature is defined without the factor 2 or even with opposite sign.

The eigenvalues of the Hamiltonian can be obtained as

$$E(S) = -J[S(S + 1) - S_1(S_1 + 1) - S_2(S_2 + 1)].$$

The spin eigenfunctions are given by  $\frac{1}{\sqrt{2}}(|+ -\rangle - |- +\rangle)$  for the singlet state and by  $\frac{1}{\sqrt{2}}(|+ -\rangle + |- +\rangle)$ ,  $|+ +\rangle$  and  $|- -\rangle$  for the three components of the triplet state and yield the eigenvalues to be  $3/2J$  and  $-1/2J$ , respectively. Mapping the  $N$ -electron singlet  $E_S$  and triplet  $E_T$  state energies onto the corresponding eigenvalues in the spin model space leads to the magnetic exchange coupling constant  $J$ . However, sufficient accuracy of singlet and triplet energies are required to map the energies onto the spin model Hamiltonian. Therefore, wave function based multireference methods have to be used to correctly describe the different spin states. For example, the difference dedicated configuration interaction (DDCI) [177, 178] and multiconfigurational second-order perturbation theory (CASPT2) [179, 180] approaches are among the techniques which

can provide the desired degree of accuracy [181, 182] whilst working with spin eigenfunctions. Comparing with time-consuming perturbation theory (PT2) mentioned above, a modified CAS-CI (complete active space configuration interaction) approach is proposed to treat rather large systems [183].

In the solids we can only use DFT to obtain information on the exchange coupling. In the DFT calculations the anti-ferromagnetic state cannot be described. However, the exchange coupling constant can be obtained by the broken symmetry approach [184-186]. In the broken symmetry (BS) approach the magnetic exchange coupling constant is obtained from the energies of two states which can both be represented by a single Slater determinant. In the first state, the high spin state (HS), the unpaired electrons at both magnetic sites are occupied with the same spin. In the second state, the so called broken symmetry state (BS), the unpaired electrons at one of the magnetic sites are flipped to opposite spin. This state is not a real spin state but a linear combination of the real spin states. They can be mapped on the Heisenberg Hamiltonian by the following steps. Formally, the BS state as well as the HS state are eigenstates of the Ising Hamiltonian, given by:

$$\hat{H}_{Ising} = -2J_{ij}S_{i,z}S_{j,z}$$

In Figure 5.2.1 the eigenstates of the Ising Hamiltonian and the HDvV Hamiltonian are compared for the coupling of two electrons. For weak couplings, the energy of the BS state is a 1:1 mixture of the singlet and the triplet state.

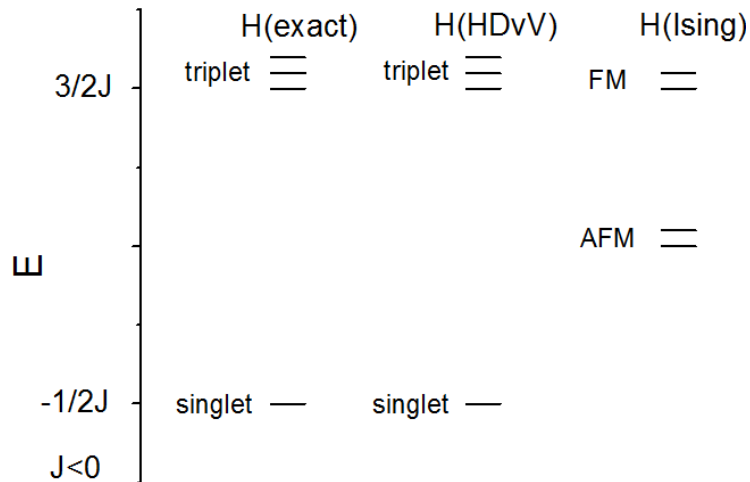


**Figure 5.2.1** Energy diagram for the eigenstates of the different spin models for the interaction of two  $S=1/2$  spins.

In general the exchange coupling can be obtained either by Noodleman's equation [186]

$$J_{ij} = -\frac{E_{HS} - E_{BS}}{4S_i S_j}$$

or by the spin projected approach by Yamaguchi and co-workers [187]

$$J_{ij} = -\frac{E_{HS} - E_{BS}}{\langle S^2 \rangle_{HS} - \langle S^2 \rangle_{BS}}$$

The broken symmetry approach can be used with either spin-unrestricted Hartree-Fock (UHF) or with any of the exchange-correlation potentials within the spin-unrestricted Kohn-Sham approach (UKS). However, it is well known that the size of the coupling is underestimated by UHF while it is significantly overestimated by the GGA functionals [188].



## 5.2.3 Results and Discussion

### 5.2.3.1 Normal and Inverse Spinel structures

Copper ferrite has two crystallographic spinel structures: the high-temperature cubic phase (c-CuFe<sub>2</sub>O<sub>4</sub>), and the low-temperature tetragonal phase (t-CuFe<sub>2</sub>O<sub>4</sub>). We consider here only the first case, because the Neel temperature (728K) [189] of CuFe<sub>2</sub>O<sub>4</sub> is located in the high temperature region. Spinel materials have a general formula of AB<sub>2</sub>O<sub>4</sub>, there are two main structural variants depending on the cations distributions, a normal spinel and an inverse spinel structure. As already mentioned in the introduction to this chapter, a spinel structure is based on an fcc sublattice of oxygen atoms, and 1/8 of tetrahedral hollow sites (A or 8a sites) and 1/2 of the octahedral sites (B or 16d sites) are occupied by cations. There are tetrahedral sites and octahedral sites which are not occupied termed as 8b and 16c sites (Wyckoff notation). The number of occupied octahedral sites is twice as number of tetrahedral sites, also the ratio between two cations in a spinel is 2:1. In a normal spinel structure of CuFe<sub>2</sub>O<sub>4</sub>, the Cu atoms occupy the tetrahedral interstitial sites and iron cations occupy the octahedral sites; In an inverse spinel structure, the iron cations occupy all of the tetrahedral and half of the octahedral sites, while Cu takes the remaining half of the 16d sites. Schematic pictures of normal and inverse spinel structures of CuFe<sub>2</sub>O<sub>4</sub> are shown in Figure 5.2.2.

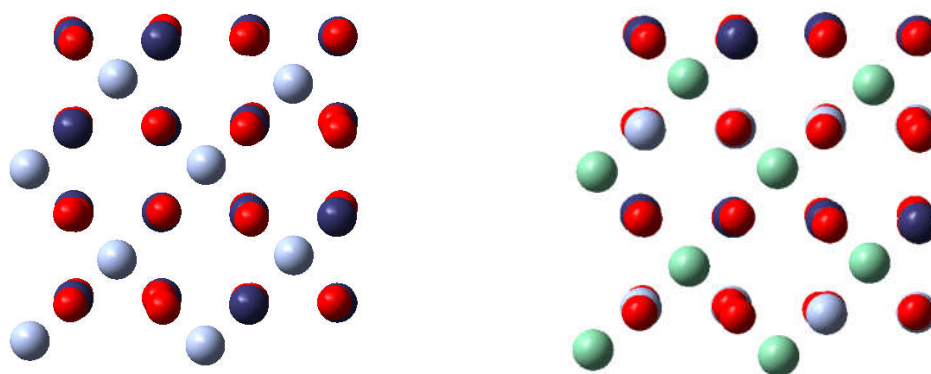


**Figure 5.2.2** Schematic pictures of normal (left) and inverse (right) spinel structures of cubic CuFe<sub>2</sub>O<sub>4</sub>. A site Fe is shown in light green, B site in dark blue and Cu in light blue.

The tetragonal phase of Cu-ferrite has an inverse spinel structure with almost all  $\text{Cu}^{2+}$  ions occupying the octahedral sublattice, whereas the  $\text{Fe}^{3+}$  ions are divided equally between the tetrahedral and octahedral sublattices [190]. Jiang et al. [191] suggested that the ground state of  $\text{CuFe}_2\text{O}_4$  bulk has an inverse spinel structure, which is a magnetic semiconductor by PBE+U calculations. However, PBE gives contrary results, which provides metallic behavior of the material [176]. For the cubic phase, our PBE+U results for lattice parameter and relative energy per unit (total energy divided by eight for our unit cell) of normal and inverse  $\text{CuFe}_2\text{O}_4$  are list in Table 1.

**Table 5.2.1** Lattice constants and relative energy per unit of spinel and inverse spinel structures of  $\text{CuFe}_2\text{O}_4$ .

	Lattice constant ( $\text{\AA}$ )	Relative energy (eV)
Normal Spinel	8.43	0.00
Inverse Spinel	8.48	0.36

The calculated relative energies suggested that the inverse spinel structure is more stable than the normal one with DFT+U method. The total density of states (DOS), and partial DOS (PDOS) projected on Cu, Fe, and O atoms for the inverse cubic  $\text{CuFe}_2\text{O}_4$  structure are shown in Figure 2. The gap between the highest states below the Fermi level and the states with the lowest energy above the F-fermi level is determined to approximately 1.2 eV, which agrees to Feng et al. [176] with  $U=4.5$  eV for Cu and  $U=4$  eV for Fe. Also, the gap and shapes of TDOS and PDOS agree to Jiang et al. [191] for a tetragonal phase inverse spinel structure.

The two  $\text{Fe}^{3+}$  cations in octahedral and tetrahedral environments are formally  $d^5$  and carrying a spin of  $S_{\text{Fe}}=5/2$  in high spin state. From the PDOS of the Fe d bands, the anti-symmetric feature between A and B ion sites indicates that A and B sites are coupled anti-ferromagnetically. Since the spin of the irons at A and B sites are antiparallel, the corresponding magnetization is about  $1 \mu_B$  per chemical formula according to the ionic model. The calculated local magnetic moments of Fe atoms at A and B sites are  $-4.06 \mu_B$  and  $4.17 \mu_B$ , respectively. For the oxygen atoms, the up and down PDOSs are nearly

symmetrical, leading to a small local magnetic moment of  $+0.10 \mu_B$ . Each  $\text{Cu}^{2+}$  ion has one unpaired electron with  $S_{\text{Cu}}=1/2$ , and the unoccupied d orbital of Cu contributes to the low energy edge of the conduction band close to the Fermi level (Figure 5.2.3). The calculated local magnetic moment for copper is  $0.63 \mu_B$ .

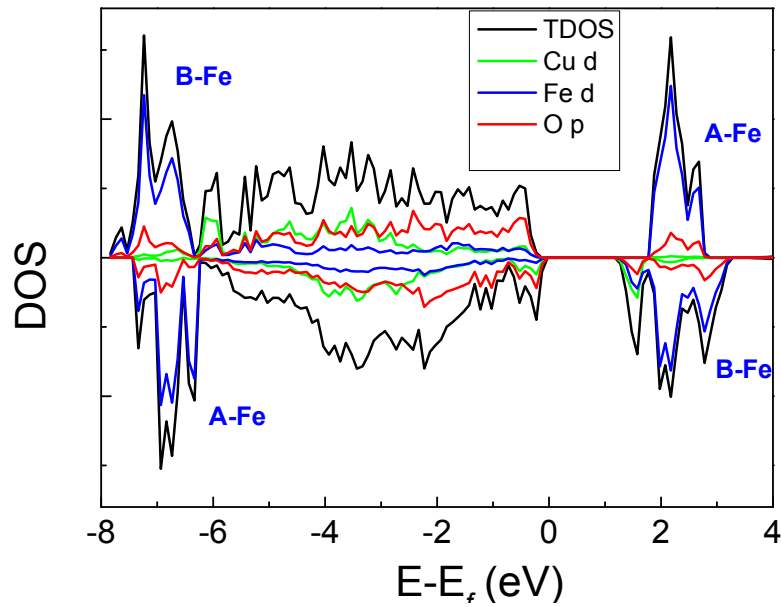


**Figure 5.2.3** Total density of states and projected density of states on Cu, Fe, and O, respectively.

### 5.2.3.2 Li-intercalation

We perform DFT calculations to determine the preferential locations of intercalating Li-ions in the crystal lattice and their effect on the superexchange coupling. The magnetic properties are influenced in two ways. On the one hand, a  $\text{Li}^+$  ion is formed during intercalation while the electron goes to one of the Fe ions. On the other hand, the superexchange interactions are very sensitive to structural changes, in particular on the M-O-M angle [192-194]. One Li ion is added to the unit cell which corresponds to a Li concentration of 12.5%. Hypothetically, an inserted Lithium ion can occupy either an available tetrahedral site (8b-site, Figure 5.2.4a) or an octahedral site (16c-site, Figure 5.2.4b). Local structural changes are present in both cases. At the tetrahedral site, two B site irons are pushed away by around  $0.2 \text{ \AA}$  because of nuclear repulsion. A charge transfer process is noticed from Li to a B site  $\text{Fe}^{3+}$ , the local magnetic moment

of the B site iron reduces from 4.17 to 3.67  $\mu_B$ . In the case of the 16c site, the Li atom is connected to two tetrahedral (8a site) Fe-ions so that the bond length between the two A site Fe-ions changes from 3.63 Å to 4.39 Å, while the angle of the  $\text{Fe}^{3+}\text{-O}^{2-}\text{-Fe}^{3+}$  bridge (angle a in Figure 5.2.4b) decreases by 9.2° (117.2° to 108.0°). The local magnetic moment of the B site decreases to 3.70  $\mu_B$ . Our calculations clearly show that the 16-c site occupation is energetically more favorable.

In both cases, the Li electron transfers to a B-site iron and reduces the local magnetic moment of the B site iron. The total magnetic moments of the system are thus reduced by 1  $\mu_B$  in the unit cell. Alternatively, the Li electron could move to one of the tetrahedral ions (Figure 5.2.4c). To stabilize the structure,  $\text{Fe}^{2+}$  which is bigger in size moves to a near octahedral site, and the Li ions moved away from the 16c site. The relative energy is close to the most stable configuration. The local magnetic moment changes from -4.06  $\mu_B$  to -3.63  $\mu_B$ . In contrast to the electron transfer to the B-site, the total magnetic moment increases by 1  $\mu_B$  in the unit cell.

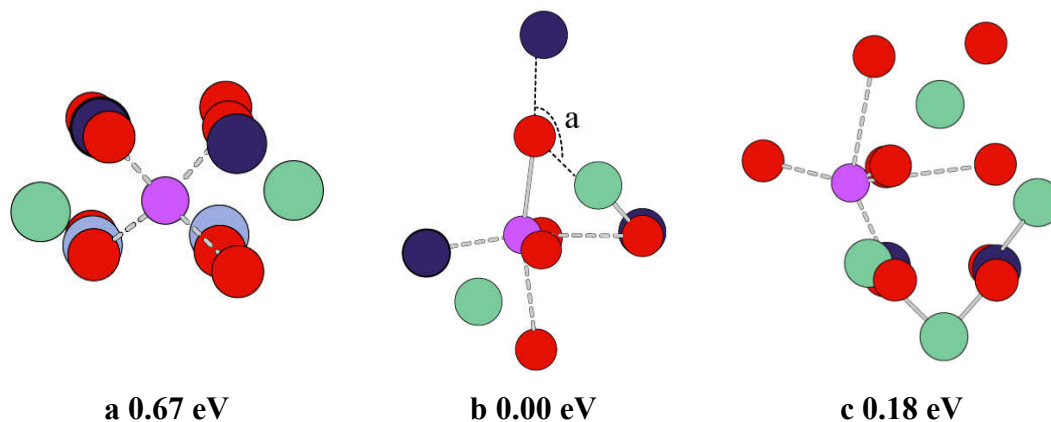


**Figure 5.2.4** lithium addition at a) a tetrahedral site, b) and c) octahedral sites. A site Fe is shown in light green, B site in dark blue, Li in purple, and Cu in light blue.

### 5.2.3.3 Magnetic Properties

The exchange coupling constants are evaluated by spin-polarized DFT calculations using the the Noodleman equation. To simplify the calculation, we focus on few magnetic centers. All metal centers not involved in the coupling constant are substituted

by nonmagnetic ions. Iron atoms are replaced by aluminum and Cu centers by zinc atoms. The results are shown in Table 5.2.2.

In the inverse spinel structure of  $\text{CuFe}_2\text{O}_4$ , we make the assumption that the coupling between A sites are negligible [189]. On another hand, B-O-B has a square angle and the exchange interaction  $J_{\text{BB}}$  ( $\sim 0$  meV) is also negligible due to our calculations. The strong interaction comes from the anti-ferromagnetic coupling between A and B site irons, the angle between A-O-B stays in the range of  $110$ - $140^\circ$ . The exchange constant calculated was calculated to be  $-4.4$  meV. The strength of the coupling is much bigger than the value of  $-1.7$  meV obtained by Bercoff et al. [189] with a two sublattice model. However, we used a GGA functional in the calculations which is known to significantly overestimate the size of the exchange coupling.

As mentioned before, Li-intercalation changes the local structure by pushing two A site irons away and the relevant A-O-B angle varies. When decreasing the angle  $\alpha$  in Figure 5.2.4b by  $9.2^\circ$ , the exchange interaction drops dramatically from  $-4.4$  meV to  $-1.5$  meV. The reduction of a B site Fe by the charge transfer from the Li atom the local spin moment decreases. In this case, the exchange coupling constant is reduced by almost 25 % to  $-3.4$  meV.

**Table 5.2.2** Calculated exchange coupling constants  $J_{AB}$  calculated from energy difference between the high spin state and the broken symmetry states,  $\Delta E_{\text{HS-BS}}$  given in meV.  $S_A$  and  $S_B$  are the tetrahedral and octahedral spins, respectively.

System	$S_A$	$S_B$	$\Delta E_{\text{HS-BS}}$	$J_{AB}$
$\text{CuFe}_2\text{O}_4$	$-5/2$	$5/2$	110	-4.4
Lithiated- $\text{CuFe}_2\text{O}_4$ (change in AOB bond angle)	$-5/2$	$5/2$	37.5	-1.5
Lithiated- $\text{CuFe}_2\text{O}_4$ (effect of cationic reduction)	$-5/2$	2	68	-3.4

## 5.2.4 Conclusion

Normal and inverse spinel structures of cubic  $\text{CuFe}_2\text{O}_4$  have been investigated by DFT+U calculations. The inverse spinel structure tends to be more stable. Li-intercalation at tetrahedral and octahedral sites has been considered, and octahedral sites were more preferable. A charge transfer process is observed from the Li atom to a B site iron. There are two processes that affect the coupling parameters upon lithiation; the first is the reduction of  $\text{Fe}^{3+}$  to  $\text{Fe}^{2+}$ ; the second is the insertion of the lithium ions into the spinel lattice and, in that process, local deformations of the cation-oxygen bonds, which in turn change the exchange coupling constant.

## 5.3 Dispersion Correction in MOCl(M=Fe,Bi) systems

### 5.3.1 Introduction

Rechargeable batteries play a dominant role in energy storage systems because of widely applications in portable electronics. Furthermore they are of fundamental importance for electric vehicles and smart grids [175, 195]. A promising rechargeable battery system should have a high energy density, use abundant material resources, offer high safety, and have environmentally friendly features. The research in rechargeable batteries is mainly focused on the electrochemical systems based on cation transfer, i.e. in Li-ion and Mg-ion batteries [175, 195, 196]. Recently, rechargeable chloride ion batteries based on chloride ion transfer have been proposed [20-22]. Metal oxychlorides such as FeOCl and BiOCl are used as cathode materials for chloride ion batteries, because they show higher stability and lower volumetric changes than metal chlorides during cycling. Besides experimental investigations, first principles calculations play an important role in the development and optimization of new energy storage and conversion materials [197]. To gain insight into the properties of MOCl (M=Fe, Bi) cathode materials, we performed DFT calculations on MOCl (M=Fe,Bi) materials. The onsite Coulomb repulsion for the d orbitals of Fe and Bi was employed. Furthermore, the long range dispersion interactions have to be taken into account within the DFT-D2 approach [198, 199], in particular with respect to the Cl<sup>-</sup> anions. We discuss the influence of the dispersion corrections on geometry and electronic structures. An anode reaction process  $\text{FeOCl} + \text{e}^- = \text{FeO} + \text{Cl}^-$  is simulated with a 2x1x2 super cell.

### 5.3.2 Theory and computational methods

All spin polarized density-functional theory (DFT) calculations [28-31] were performed with the Vienna ab initio Simulation Package (VASP). The generalized gradient approximation with the functional described by Perdew, Burke, and Ernzerhof (GGA-PBE) [35] was used for all calculations. The projector-augmented wave (PAW) method [42, 43] is applied to describe the wavefunctions in the core regions, while the

valence wavefunctions are expanded as linear combination of plane-waves with a cutoff energy of 550 eV. With this value the total energy is converged within 2 meV. Dealing with iron, a) the spin polarized calculation with the observed anti-ferromagnetic (AFM) ground state ordering was performed; b) the on-site Coulomb interactions [47, 152] were included for the strongly correlated Fe 3d orbitals, with an effective U value of 4.6 [200]. Furthermore, the long-range dispersion corrections have been taken into account within a DFT-D2 approach [198, 199, 201], as implemented in the latest version of VASP [202]. In the geometry optimizations, the total energy was converged to  $10^{-5}$  eV and the Hellmann-Feynman force on each relaxed atom was less than 0.01 eV Å<sup>-1</sup>.

Our unit cell for simulating the dissociation process is restrained to Fe<sub>8</sub>O<sub>8</sub>Cl<sub>x</sub> (x = 0-8), the Brillouin zone was sampled with a (3×3×3) Monkhorst-Pack mesh of k-points, which have been tested with respect to the total energy of the system. For the optimization of the lattice constants, we always fixed two lattice constants and optimized the third one; this was done iteratively until the changes were less than 0.02 Å.

The electrostatic potential energy is calculated upon the formula as follow,

$$E_a = k_e \sum_j \frac{q_a q_j}{r_{aj}} \quad (1)$$

where  $k_e$  represents the Coulombic constant,  $j$  is the index for the point charges within a point charge field, which has been constructed from the optimized unit cell and contains 81000 point charges.

### 5.3.3 Results and Discussion

#### 5.3.3.1 Bulk structures of MOCl

The tetragonal BiOCl crystal that belongs to the space group of P4/nmm and has a typical layered structure with an ordered packing of five-atom layers in the sequence –



O–Bi–Cl–Cl–Bi– along the *c*-axis. The layered structure model of the BiOCl unit cell is shown as inset in Figure 5.3.1 (left). The Bi atom is coordinated to a square antiprism with four O atoms in one base and four Cl atoms in the other. The O atom is tetrahedrally coordinated by four Bi atoms. The Cl atom is bound to four Bi atoms in a planar square to form a pyramid and with its nonbonding (lone pair) electrons pointing to the opposite side of the square. FeOCl, on the other hand, belongs to the orthorhombic space group Pmmn and has six-atom layers in the sequence –O–Fe–Cl–Cl–Fe–O– along the *b*-axis direction (Figure 5.3.1 right). Each Fe-ion is coordinated by four oxygen ions and two chloride ions, the O atoms occupy tetrahedral sites of four Fe atoms, and Cl connects to two iron atoms.

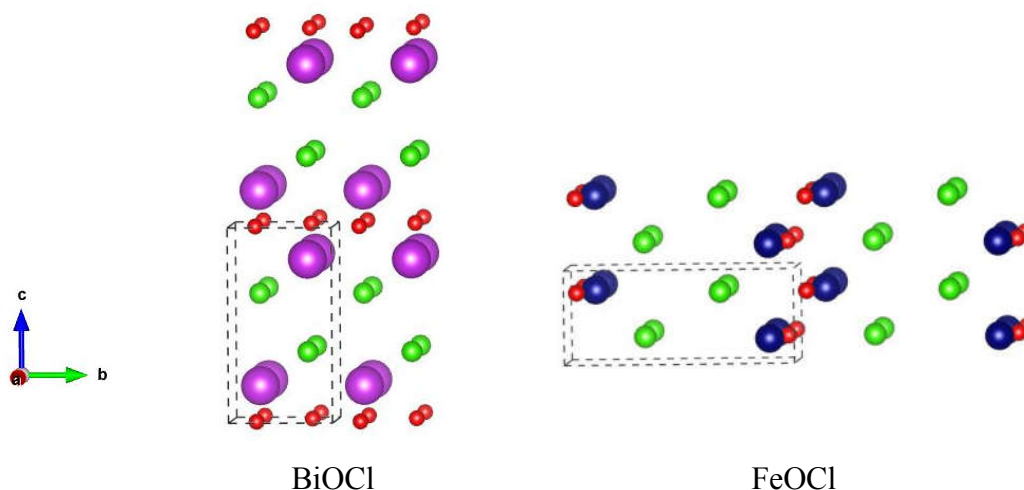


**Figure 5.3.1** Crystal models of BiOCl (left) and FeOCl (right) systems (Bi, purple; Fe, blue; O, red; Cl, green).

Comparison between the DFT/PBE and dispersion corrected PBE+D2 results for the geometric structure and the lattice constants are listed in Table 1. Zhang et al. [203] found that there is a significant error in the *c*-lattice parameter and *c/a* ratio of BiOCl of about 10% when the PBE+U calculations are compared to experiment. We found 7.8 % in our calculations. The error drops to less than 1% when dispersion corrections are taken into account. We noticed that in both compounds, BiOCl and FeOCl, the main difference between normal PBE and PBE+D2 comes from the distance between the two

chloride layers. Normal GGA functionals fail to describe this weak interactions, and the bond distance of Cl-Cl is overestimated by 0.32 and 0.48 Å for BiOCl and FeOCl respectively. Our PBE+U+D2 results, on the contrary, agree to the experimental data very well.

Table 5.3.1 Calculated geometry parameters and lattice constants of MOCl ( $M=Fe,Bi$ ) using PBE and PBE+D2 methods, units are in Å.

	BiOCl			FeOCl		
	PBE	PBE+D2	Exp. [204]	PBE	PBE+D2	Exp. [205]
M-O	2.335	2.303	2.316	2.003	1.982	1.961
M-Cl	3.088	3.079	3.059	2.387	2.376	2.364
Cl-Cl	3.802	3.450	3.487	4.157	3.747	3.681
$a$	3.908	3.894	3.887	3.861	3.815	3.773
$b$	3.908	3.894	3.887	8.563	8.050	7.910
$c$	7.926	7.297	7.354	3.301	3.298	3.301

### 5.3.3.2 FeOCl dechlorination process

Herein we employ DFT+U+D2 calculations to get insight into the chloride ion removal of FeOCl. Each  $Fe^{3+}$  is coordinated by four oxygen ions and two chloride ions, and two neighboring ions are coupled anti-ferromagnetically to form a ground state without magnetism. A  $2 \times 1 \times 2$  super cell  $Fe_8O_8Cl_x$  ( $x = 0-8$ ) was chosen to simulate the dissociation process (Figure 5.3.2).

We start with the removal of chloride ion 1 ( $Cl_1$ ) from  $Fe_8O_8Cl_8$  (perfect FeOCl crystal structure) in Figure 2. The charges of the two iron ions which connect to  $Cl_1$  are decreased by  $0.17e^-$  according to the Bader charge analysis [206-208]. The reduced iron ions then move inward to the oxygen row, resulting in an increase in the lattice parameter  $a$  by about 0.2 Å, while the other two lattice parameters are barely changing. Another consequence is that the interaction between the reduced iron ions and the neighboring chloride ions,  $Cl_5$  for example, is weakened. According to the calculated

electrostatic potential energy based on equation (1), Cl<sub>5</sub> is with E<sub>a</sub>= -5.86 eV, less stable than Cl<sub>2</sub>, Cl<sub>3</sub>, Cl<sub>4</sub>, Cl<sub>6</sub>, Cl<sub>7</sub> and Cl<sub>8</sub> with -8.46, -8.76, -8.01, -7.39, -7.34 and -7.83 eV, respectively. This indicates that in the next step Cl<sub>5</sub> will be removed. In the following all chloride ions in the *c*-row (Cl<sub>1</sub>,Cl<sub>5</sub>) are removed one after the other (25% chloride ion dissociation). Then the neighboring Fe-plane is completely reduced and moved towards to the adjacent oxygen plane. The whole framework of FeOCl (Fe<sub>8</sub>O<sub>8</sub>Cl<sub>6</sub>), however, is almost unchanged; the lattice parameters *b* and *c* stay the same.

We then move another *c*-row of chloride ions from our model system (Fe<sub>8</sub>O<sub>8</sub>Cl<sub>4</sub>, 50% chloride ion dissociation). It worth noticing that the rearrangement of atomic positions after optimization comes to the structure shown in Figure 2 independent of *c*-rows of chloride ions which we chose. The *b*-parameter drops dramatically by about 2 Å (Figure 3); *a* and *c* parameters are slightly changed. -Fe-O- planes tend to be formed, since the reduced iron ions keep moving to oxygen rows. For the Fe<sub>8</sub>O<sub>8</sub>Cl<sub>2</sub> (75% chloride ion dissociation) model, the transformation from FeOCl to FeO is almost finished. The *b*-parameter is decreased further and *a*,*c*-parameters are evidently increased to form Fe<sup>2+</sup>O<sup>2+</sup> planes. In the end, a rock salt type FeO structure is obtained after complete dechlorination. Each iron ion connects to six oxygen ions, occupying an octahedral site. The optimized lattice parameter of FeO is 4.35 Å, which agrees well with the experimental value of 4.30 Å [209].

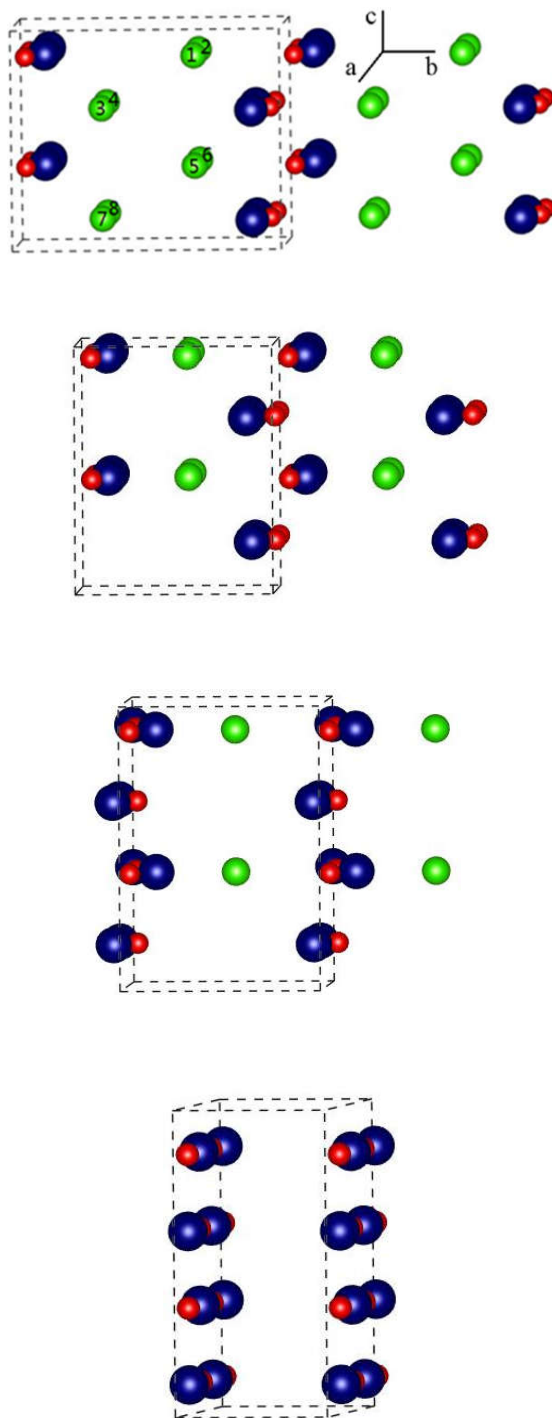


**Figure 5.3.2** Optimized bulk structure of  $Fe_8O_8Cl_x$  ( $x = 0-8$ ; Fe, blue; O, red; Cl, green) by DFT+U+D2. Top:  $Fe_8O_8Cl_8$ ; middle:  $Fe_8O_8Cl_4$  and  $Fe_8O_8Cl_2$ ; bottom:  $Fe_8O_8$ .

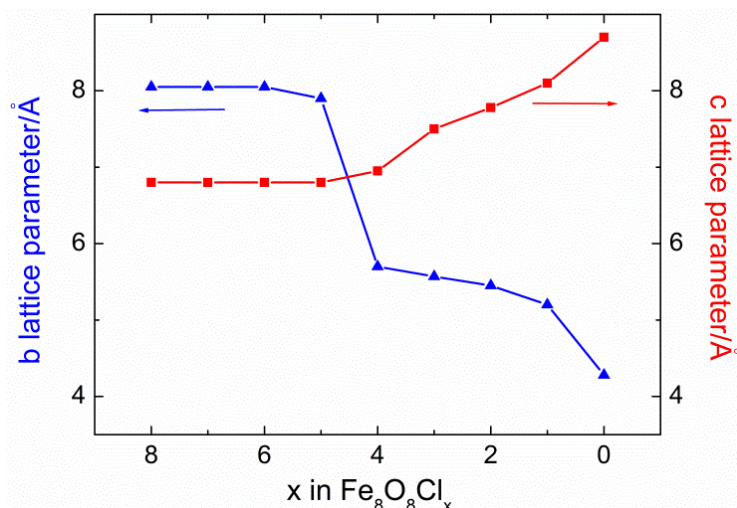


**Figure 5.3.3** Changes in the lattice parameters *b* and *c* upon removal of chloride ions from  $Fe_8O_8Cl_x$ .

### 5.3.3.3 Conclusion

We performed DFT calculations with normal PBE functional and dispersion corrected PBE+D2 on MOCl (M=Fe,Bi) materials. Only after the inclusion of the D2 dispersion correction for the structural parameters the interaction of the Cl<sup>-</sup> anions could be reasonably described. The structural parameters lattice constants of MOCl (M=Fe,Bi) agreed well with the experimental data. The structure optimizations for the removal of different percentages of Cl<sup>-</sup> ions from FeOCl indicate that one of the chlorine layers in FeOCl dissociates first, leading to a drastic decrease in the lattice parameter *b* of FeOCl. Then the loss of the other chlorine layer results in the formation of FeO.

## 6 Summary

In this thesis, different transition metal oxide materials are investigated by quantum chemical calculations. The systems and properties are related to technical relevant processes such as catalysis, solar cells, battery materials, and magnetism. In this context, structural aspects such as surface relaxation, adsorption geometries, and defect structures, the electronic structure and spectroscopic data, as well as magnetic couplings are investigated.

DFT plane wave calculations with periodic boundary conditions (PBC) as well as embedded cluster (EC) calculations have been performed. Apart from the calculations for the different properties, a thorough investigation of the applicability of the two theoretical approaches was performed and their behaviors on technical details investigated. The main results for the different applications can be summarized as follows.

The first application focuses on the adsorption of formic acid on a ZnO (10-10) surface. The results of the theoretical calculations are used to assign different adsorption sites by comparison of the experimental IR data and the calculations. According to the analysis of the frequencies, formic acid adsorbs in a dissociated form, i.e. as formate anion accompanied by a surface OH group on the mixed-terminated ZnO (10-10) surface. Adsorption is possible in two different orientations, which are perpendicular to each other. The bidentate structure which is oriented along the  $[1-210]$  direction is most stable based on the DFT calculations. A quasi-bidentate, oriented along  $[0001]$ , is found at slightly higher energies. If these two orthogonal orientations are considered, the intensities in the IR spectra are comprehensible.

Furthermore, the applicability of plane wave calculations and embedded cluster calculations for the adsorption of formic acid on ZnO (10-10) was investigated. For cluster calculations, we applied the periodic electrostatic embedded cluster method (PEECM) and a point charge field where multipole moments of the unit cell were compensated by an Evjen procedure. The two embedding schemes are giving similar

results on adsorption properties including binding energies and vibrational frequencies. While the structural parameters and binding energies obtained with the embedded cluster calculations with an SVP basis set and the plane wave calculations are rather similar, the deviations in the calculated frequencies can be of the order of  $50 \text{ cm}^{-1}$ . The agreement of PBC and EC calculations became much better when the basis set in the EC calculations was increased. In general, DFT calculations with the PBC method provide reasonable structures, thus surface relaxation can then be considered for the construction of the embedding either by a point charge field with compensation of multipole moments or with PEECM. The adsorption geometries and local structure relaxations are reasonably described in the EC calculations. Here, hybrid functionals or MP2 calculations are easily affordable. The binding energies of the bidentate structure obtained with B3LYP/SVP and MP2/SVP are similar and differ by  $\sim 3 \text{ kcal/mol}$  using the PBE/SVP method; the increased basis set from SVP to TZVP for the MP2 calculation changes the value by  $-1.5 \text{ kcal/mol}$ .

In the second application, DFT plane wave calculations as well as embedded cluster calculations are performed on nitrogen monoxide (NO) adsorption on the rutile  $\text{TiO}_2$  (110) surface. Upon removal of a neutral oxygen atom, two excess electrons remain in the system. It is still under discussion where these electrons are localized in case of rutile  $\text{TiO}_2$ . However, the description of these excess electrons is problematic for normal DFT (LDA/GGA) calculations, which tend to stabilize solutions with delocalization of spin density because of the well-known self-interaction error. Therefore, we performed DFT+U calculations and hybrid functional calculations on the reduced surfaces with periodic and embedded cluster approaches. The NO radical was chosen because we wanted to investigate the coupling of the unpaired electron from NO with the excess electrons of a reduced (bridge oxygen vacancies) surface. In turn, the coupling interactions may provide useful information for locating the excess electrons on the surface. Different localized solutions ( $\text{Ti}^{3+}$  pairs) for the two excess electrons have been considered, including the vacancy site and the neighboring Ti rows on the surface and subsurface. Our PBE+U ( $U=4.2 \text{ eV}$ ) results agree to other super cell calculations with GGA+U and hybrid functionals where the subsurface sites are preferred. However,

other localizations are close in energy and cannot be ruled out. The influence of excess electron localizations on adsorption properties is then taken into account. On a defect free surface, NO prefers to adsorb on the surface at a Ti(5c) site with an N-orientated tilted structure. On a reduced surface, the most active site for NO adsorption is the vacancy site, and the adsorption energy is calculated to be 1.72 eV. The two excess electrons locate at the vacancy site, where one of the electrons is transferred to NO to form a triplet  $\text{NO}^-$  and the other is shared by the two neighboring Ti atoms coupled anti-ferromagnetically with  $\text{NO}^-$ . For this configuration, the NO stretching frequency shows a shift of  $400\text{ cm}^{-1}$  from NO in gas phase. Two local minima structures were found with NO adsorption at the Ti(5c) site. For a first tilted structure, the unpaired electrons are well localized on the Ti atom sites and do not participate in the adsorption process. Accordingly, the adsorption energy and frequency do not change much compared to NO on the defect free surface. In the upright configuration, however, one electron is transferred to NO and the adsorption energy increases by 0.2 eV compared to the tilted structure, also the frequency has a blue shift of  $170\text{ cm}^{-1}$ . We concluded from these results that the coupling interaction between the NO radical and the excess electrons is either so strong (vacancy site) that the electronic configuration is completely changed; or so small (Ti(5c) site) that it has no influence on the NO. Therefore, NO adsorption cannot be used to obtain information on the localization of the excess electrons.

The third part of applications had a focus on iron oxides and related systems. The calculations on these systems have been performed using the plane wave DFT+U approach to account for the on-site Coulomb correction of the Fe 3d states. Otherwise the band gap would be underestimated and the magnetic structure could not be properly described.

First, we studied the adsorption of a CO molecule on the  $\alpha\text{-Fe}_2\text{O}_3(0001)$  surface. In the ground state, the irons within a (0001) plane are coupled ferromagnetically, while the irons between two adjacent (0001) planes are coupled anti-ferromagnetically in a Fe-O3-Fe group. Only the non-polar single Fe-terminated surface is considered in our calculations. On this surface, the CO molecule adsorbs in an upright configuration with an adsorption energy of 0.53 eV, which is in line with CO adsorption on other oxide



surfaces. The frequency of the CO stretching vibration changes from  $2124\text{cm}^{-1}$  in gas phase to  $2144\text{ cm}^{-1}$  on the surface, in good agreement with the experimental values of  $2143\text{ cm}^{-1}$  and  $2173\text{ cm}^{-1}$ .

Next, the change of the magnetic properties of normal and inverse spinel structures of cubic  $\text{CuFe}_2\text{O}_4$  upon Li-intercalation has been investigated. The magnetic exchange coupling constants of different ion pairs were obtained with the broken symmetry approach. The inverse spinel structure, where Cu(II) is found at half of the occupied octahedral sites, tends to be more stable. The dominating magnetic coupling was observed between tetrahedral and octahedral Fe(III) ions.

The intercalating Li atoms occupied empty octahedral sites. A charge transfer process is observed from the Li atom to the octahedrally coordinated Fe(III) ions. There are two processes that affect the coupling parameters upon lithiation; the first is the reduction of  $\text{Fe}^{3+}$  to  $\text{Fe}^{2+}$ , which reduces the total spin as well as the coupling strength, the second is that the insertion of the lithium ions into the spinel lattice induces local deformations of the cation-oxygen bonds, which in turn also change the exchange coupling constant. In the last example structural changes upon reversible dechlorination of  $\text{MOCl}$  ( $\text{M}=\text{Fe}, \text{Bi}$ ) materials has been investigated. These materials are used as cathode materials in battery research. In the crystal structure, the  $\text{Cl}^-$  ions are located in two neighboring planes. Only after inclusion of dispersion corrections, the structural parameters, in particular with respect to the distance of the  $\text{Cl}^-$  layers, could be described reasonably. In agreement with the experimental data, the structure optimizations for  $\text{FeOCl}_x$  show that severe changes in the lattice parameters occur when a complete chlorine layer is removed. When half of the  $\text{Cl}^-$  ions are removed, the lattice parameter  $b$  is reduced by 25%. After full removal of  $\text{Cl}^-$ ,  $\text{FeO}$  is formed.

## 7 Bibliography

[1] H. H. Kung, *Transition Metal Oxides: Surface Chemistry and Catalysis*, **1989**, Elsevier Science

- [2] S. Lee, *Methanol Synthesis Technology*, **1989**, Taylor & Francis
- [3] W. Weisweiler, *Chem. Ing. Tech.*, **2004**, 76, 152.
- [4] L. Tecchio, P. Marín, F. V. Díez, S. Ordóñez, *J. Chem. Technol. Biot.*, **2014**, Online Version of Record published before inclusion in an issue.
- [5] S. M. El-Sheikh, F. A. Harraz, K. S. Abdel-Halim, *J. Alloy. Compd.*, **2009**, 487, 716.
- [6] S. Enthaler, K. Junge, M. Beller, *Angew. Chem. Int. Edit.*, **2008**, 47, 3317.
- [7] S. Royer, D. Duprez, *ChemCatChem*, **2011**, 3, 24.
- [8] J. Schneider, M. Matsuoka, M. Takeuchi, J. Zhang, Y. Horiuchi, M. Anpo, D. W. Bahnemann, *Chem. Rev.*, **2014**, 114, 9919.
- [9] A. Corma, H. Garcia, *Chem. Soc. Rev.*, **2008**, 37, 2096.
- [10] M. Gratzel, *Nature*, **2001**, 414, 338.
- [11] M. Grätzel, *J. Photochem. Photobiol. C: Photochem. Rev.*, **2003**, 4, 145.
- [12] J. A. Anta, E. Guillén, R. Tena-Zaera, *J. Phys. Chem. C*, **2012**, 116, 11413.
- [13] M. D. McCluskey, S. J. Jokela, *J. Appl. Phys.*, **2009**, 106, 071101.
- [14] Y. Zorenko, T. Zorenko, T. Voznyak, A. Mandowski, X. Qi, M. Batentschuk, J. Friedrich, *IOP Conference Series: Materials Science and Engineering*, **2010**, 15, 012060.
- [15] X. Pan, M.-Q. Yang, X. Fu, N. Zhang, Y.-J. Xu, *Nanoscale*, **2013**, 5, 3601.
- [16] C. Julien, Z. Stoyanov, *Materials for Lithium-Ion Batteries*, **2012**, Springer Netherlands
- [17] J. Bhattacharya, A. Van der Ven, *Phys. Rev. B*, **2010**, 81, 104304.
- [18] J. Bhattacharya, C. Wolverton, *Phys. Chem. Chem. Phys.*, **2013**, 15, 6486.
- [19] S. Dasgupta, B. Das, M. Knapp, R. A. Brand, H. Ehrenberg, R. Kruk, H. Hahn, *Adv. Mater.*, **2014**, 26, 4639.
- [20] X. Zhao, S. Ren, M. Bruns, M. Fichtner, *J. Power Sources*, **2014**, 245, 706.
- [21] X. Zhao, Z. Zhao-Karger, D. Wang, M. Fichtner, *Angew. Chem. Int. Edit.*, **2013**, 52, 13621.
- [22] X. Zhao, Q. Li, Z. Zhao-Karger, P. Gao, K. Fink, X. Shen, M. Fichtner, *ACS Appl. Mater. Interface*, **2014**, 6, 10997.
- [23] L. Maschio, D. Usvyat, M. Schütz, B. Civalleri, *J. Chem. Phys.*, **2010**, 132, 134706.

- [24] C. Pisani, M. Schutz, S. Casassa, D. Usvyat, L. Maschio, M. Lorenz, A. Erba, *Phys. Chem. Chem. Phys.*, **2012**, 14, 7615.
- [25] K. Burke, *J. Chem. Phys.*, **2012**, 136, 150901.
- [26] J. Hafner, *J. Comput. Chem.*, **2008**, 29, 2044.
- [27] S. F. Sousa, P. A. Fernandes, M. J. Ramos, *J. Phys. Chem. A*, **2007**, 111, 10439.
- [28] P. Hohenberg, W. Kohn, *Phys. Rev.*, **1964**, 136, B864.
- [29] W. Kohn, L. J. Sham, *Phys. Rev.*, **1965**, 140, A1133.
- [30] O. Gunnarsson, B. I. Lundqvist, *Phys. Rev. B*, **1976**, 13, 4274.
- [31] U. v. Barth, L. Hedin, *J. Phys. C: Solid State Phys.*, **1972**, 5, 1629.
- [32] S. H. Vosko, L. Wilk, M. Nusair, *Can. J. Phys.*, **1980**, 58, 1200.
- [33] I. Levine, *Quantum Chemistry: 5<sup>th</sup> edition*, **1999**, Prentice Hall.
- [34] J. P. Perdew, Y. Wang, *Phys. Rev. B*, **1992**, 45, 13244.
- [35] J. P. Perdew, K. Burke, M. Ernzerhof, *Phys. Rev. Lett.*, **1996**, 77, 3865.
- [36] C. Lee, W. Yang, R. G. Parr, *Phys. Rev. B*, **1988**, 37, 785.
- [37] F. Bloch, *Z. Physik*, **1928**, 52, 555.
- [38] J. C. Phillips, L. Kleinman, *Phys. Rev.*, **1959**, 116, 287.
- [39] H. Hellmann, *J. Chem. Phys.*, **1935**, 3, 61.
- [40] D. R. Hamann, M. Schlüter, C. Chiang, *Phys. Rev. Lett.*, **1979**, 43, 1494.
- [41] D. Vanderbilt, *Phys. Rev. B*, **1990**, 41, 7892.
- [42] P. E. Blöchl, *Phys. Rev. B*, **1994**, 50, 17953.
- [43] G. Kresse, D. Joubert, *Phys. Rev. B*, **1999**, 59, 1758.
- [44] H. J. Monkhorst, J. D. Pack, *Phys. Rev. B*, **1976**, 13, 5188.
- [45] Y. Zhang, W. Yang, *J. Chem. Phys.*, **1998**, 109, 2604.
- [46] M. K. Y. Chan, G. Ceder, *Phys. Rev. Lett.*, **2010**, 105, 196403.
- [47] S. L. Dudarev, G. A. Botton, S. Y. Savrasov, C. J. Humphreys, A. P. Sutton, *Phys. Rev. B*, **1998**, 57, 1505.
- [48] M. Methfessel, A. T. Paxton, *Phys. Rev. B*, **1989**, 40, 3616.
- [49] A. De Vita, *The Energetics of Defects and Impurities in Metals and Ionic Materials from First Principles*, *Ph. D Thesis*, **1992**, Keele University.
- [50] E. H. Teunissen, A. P. J. Jansen, R. A. van Santen, R. Orlando, R. Dovesi, *J. Chem.*

- Phys.*, **1994**, 101, 5865.
- [51] B. Herschend, M. Baudin, K. Hermansson, *J. Chem. Phys.*, **2004**, 120, 4939.
- [52] K. Fink, *Phys. Chem. Chem. Phys.*, **2006**, 8, 1482.
- [53] D. Stodt, C. Hattig, *J. Chem. Phys.*, **2012**, 137, 114705.
- [54] A. M. Burow, M. Sierka, J. Dobler, J. Sauer, *J. Chem. Phys.*, **2009**, 130, 174710.
- [55] C. A. White, M. Head-Gordon, *J. Chem. Phys.*, **1994**, 101, 6593.
- [56] K. N. Kudin, G. E. Scuseria, *J. Chem. Phys.*, **2004**, 121, 2886.
- [57] H. M. Evjen, *Phys. Rev.*, **1932**, 39, 675.
- [58] F. Rittner, R. Fink, B. Boddenberg, V. Staemmler, *Phys. Rev. B*, **1998**, 57, 4160.
- [59] K. N. Kudin, G. E. Scuseria, *Chem. Phys. Lett.*, **1998**, 283, 61.
- [60] L. Z. Stolarczyk, L. Piela, *Int. J. Quantum. Chem.*, **1982**, 22, 911.
- [61] L. Piela, J. L. Brédas, J. M. André, *J. Chem. Phys.*, **1983**, 78, 295.
- [62] S. Pearton, *Prog. Mater. Sci.*, **2005**, 50, 293.
- [63] C. Wöll, *Prog. Surf. Sci.*, **2007**, 82, 55.
- [64] U. Özgür, Y. I. Alivov, C. Liu, A. Teke, M. A. Reshchikov, S. Doğan, V. Avrutin, S. J. Cho, H. Morkoç, *J. Appl. Phys.*, **2005**, 98, 041301.
- [65] B. E. Hayden, A. King, M. A. Newton, *J. Phys. Chem. B*, **1999**, 103, 203.
- [66] A. Mattsson, S. Hu, K. Hermansson, L. Osterlund, *J. Chem. Phys.*, **2014**, 140, 034705.
- [67] H. Nakatsuji, M. Yoshimoto, Y. Umemura, S. Takagi, M. Hada, *J. Phys. Chem.*, **1996**, 100, 694.
- [68] P. Persson, L. Ojamäe, *Chem. Phys. Lett.*, **2000**, 321, 302.
- [69] P. Persson, S. Lunell, L. Ojamäe, *Int. J. Quantum. Chem.*, **2002**, 89, 172.
- [70] S. Crook, H. Dhariwal, G. Thornton, *Surf. Sci.*, **1997**, 382, 19.
- [71] S. T. Teklemichael, M. D. McCluskey, *J. Phys. Chem. C*, **2012**, 116, 17248.
- [72] M. Xu, H. Noei, M. Buchholz, M. Muhler, C. Wöll, Y. Wang, *Catal. Today*, **2012**, 182, 12.
- [73] R. Davis, J. F. Walsh, C. A. Muryn, G. Thornton, V. R. Dhanak, K. C. Prince, *Surf. Sci.*, **1993**, 298, L196.
- [74] A. Lenz, L. Selegård, F. Söderlind, A. Larsson, P. O. Holtz, K. Uvdal, L. Ojamäe,

- P.-O. Käll, *J. Phys. Chem. C*, **2009**, 113, 17332.
- [75] F. Labat, I. Ciofini, C. Adamo, *J. Chem. Phys.*, **2009**, 131, 044708.
- [76] M. Buchholz, Q. Li, H. Noei, A. Nefedov, Y. Wang, M. Muhler, K. Fink, C. Wöll, *Top. Catal.*, **2015**, 58, 174.
- [77] G. Kresse, J. Furthmüller, *Phys. Rev. B*, **1996**, 54, 11169.
- [78] G. Kresse, J. Furthmüller, *Comp. Mater. Sci.*, **1996**, 6, 15.
- [79] G. Kresse, J. Hafner, *Phys. Rev. B*, **1993**, 48, 13115.
- [80] B. Meyer, D. Marx, *Phys. Rev. B*, **2003**, 67, 035403.
- [81] H. Karzel, W. Potzel, M. Köfferlein, W. Schiessl, M. Steiner, U. Hiller, G. M. Kalvius, D. W. Mitchell, T. P. Das, P. Blaha, K. Schwarz, M. P. Pasternak, *Phys. Rev. B*, **1996**, 53, 11425.
- [82] C. B. Duke, R. J. Meyer, A. Paton, P. Mark, *Phys. Rev. B*, **1978**, 18, 4225.
- [83] S. Baroni, S. de Gironcoli, A. Dal Corso, P. Giannozzi, *Rev. Mod. Phys.*, **2001**, 73, 515.
- [84] R. M. Pick, M. H. Cohen, R. M. Martin, *Phys. Rev. B*, **1970**, 1, 910.
- [85] X. Gonze, C. Lee, *Phys. Rev. B*, **1997**, 55, 10355.
- [86] K. David, B. Tomáš, H. Jürgen, *J. Phys.: Condens. Matter*, **2010**, 22, 265006.
- [87] TURBOMOLE, a development of University of Karlsruhe and Forschungszentrum Karlsruhe GmbH, 1989-2007, TURBOMOLE GmbH, since 2007; available from <http://www.turbomole.com>.
- [88] R. Ahlrichs, M. Bär, M. Häser, H. Horn, C. Kölmel, *Chem. Phys. Lett.*, **1989**, 162, 165.
- [89] O. Treutler, R. Ahlrichs, *J. Chem. Phys.*, **1995**, 102, 346.
- [90] F. Schautz, H. J. Flad, M. Dolg, *Theor. Chem. Acc.*, **1998**, 99, 231.
- [91] A. Schäfer, H. Horn, R. Ahlrichs, *J. Chem. Phys.*, **1992**, 97, 2571.
- [92] A. Schäfer, C. Huber, R. Ahlrichs, *J. Chem. Phys.*, **1994**, 100, 5829.
- [93] F. Weigend, M. Häser, H. Patzelt, R. Ahlrichs, *Chem. Phys. Lett.*, **1998**, 294, 143.
- [94] C. Møller, M. S. Plesset, *Phys. Rev.*, **1934**, 46, 618.
- [95] S. F. Boys, F. Bernardi, *Mol. Phys.*, **1970**, 19, 553.
- [96] G. Busca, V. Lorenzelli, *Mater. Chem.*, **1982**, 7, 89.

- [97] K. Nakamoto, *Infrared and Raman Spectra of Inorganic and Coordination Compounds, Applications in Coordination, Organometallic, and Bioinorganic Chemistry*, **2009**, Wiley
- [98] Y. Gao, N. Zhao, W. Wei, Y. Sun, *Comp. Theor. Chem.*, **2012**, 992, 1.
- [99] M. J. S. Spencer, K. W. J. Wong, I. Yarovsky, *Mater. Chem. Phys.*, **2010**, 119, 505.
- [100] W. Göpel, J. Pollmann, I. Ivanov, B. Reihl, *Phys. Rev. B*, **1982**, 26, 3144.
- [101] N. Jedrecy, S. Gallini, M. Sauvage-Simkin, R. Pinchaux, *Surf. Sci.*, **2000**, 460, 136.
- [102] C. T. Vo, L. K. Huynh, J. Y. Hung, J.-C. Jiang, *Appl. Surf. Sci.*, **2013**, 280, 219.
- [103] T. Shimanouchi, *Tables of Molecular Vibrational Frequencies Consolidated Volume I, National Bureau of Standards*, **1972**, 1-160.
- [104] H. K. Gerardi, A. F. DeBlase, X. Su, K. D. Jordan, A. B. McCoy, M. A. Johnson, *J. Phys. Chem. Lett.*, **2011**, 2, 2437.
- [105] M. P. Andersson, P. Uvdal, *J. Phys. Chem. A*, **2005**, 109, 2937.
- [106] J. Tian, Z. Zhao, A. Kumar, R. I. Boughton, H. Liu, *Chem. Soc. Rev.*, **2014**, 43, 6920.
- [107] U. Diebold, *Surf. Sci. Rep.*, **2003**, 48, 53.
- [108] N. A. Deskins, R. Rousseau, M. Dupuis, *J. Phys. Chem. C*, **2010**, 114, 5891.
- [109] M. Xu, H. Noei, K. Fink, M. Muhler, Y. Wang, C. Woll, *Angew. Chem. Int. Edit.*, **2012**, 51, 4731.
- [110] T. Schmidt, E. Kraisler, A. Makmal, L. Kronik, S. Kümmel, *J. Chem. Phys.*, **2014**, 140, 18A510.
- [111] B. J. Morgan, G. W. Watson, *Surf. Sci.*, **2007**, 601, 5034.
- [112] A. I. Liechtenstein, V. I. Anisimov, J. Zaanen, *Phys. Rev. B*, **1995**, 52, R5467.
- [113] E. Finazzi, C. Di Valentin, G. Pacchioni, A. Selloni, *J. Chem. Phys.*, **2008**, 129, 154113.
- [114] T. Bredow, G. Pacchioni, *Chem. Phys. Lett.*, **2002**, 355, 417.
- [115] A. Janotti, J. B. Varley, P. Rinke, N. Umezawa, G. Kresse, C. G. Van de Walle, *Phys. Rev. B*, **2010**, 81,
- [116] S. Chrétien, H. Metiu, *J. Phys. Chem. C*, **2011**, 115, 4696.

- [117] P. Krüger, S. Bourgeois, B. Domenichini, H. Magnan, D. Chandesris, P. Le Fèvre, A. M. Flank, J. Jupille, L. Floreano, A. Cossaro, A. Verdini, A. Morgante, *Phys. Rev. Lett.*, **2008**, 100,
- [118] N. A. Deskins, M. Dupuis, *Phys. Rev. B*, **2007**, 75,
- [119] N. A. Deskins, R. Rousseau, M. Dupuis, *J. Phys. Chem. C*, **2011**, 115, 7562.
- [120] T. Shibuya, K. Yasuoka, S. Mirbt, B. Sanyal, *J. Phys. Condens. Matter*, **2012**, 24, 435504.
- [121] N. A. Deskins, R. Rousseau, M. Dupuis, *J. Phys. Chem. C*, **2009**, 113, 14583.
- [122] P. M. Kowalski, M. F. Camellone, N. N. Nair, B. Meyer, D. Marx, *Phys. Rev. Lett.*, **2010**, 105,
- [123] J. Huusko, V. Lantto, H. Torvela, *Sensors and Actuators B: Chemical*, **1993**, 16, 245.
- [124] D. C. Sorescu, C. N. Rusu, J. T. Yates, *J. Phys. Chem. B*, **2000**, 104, 4408.
- [125] D. Stodt, H. Noei, C. Hattig, Y. Wang, *Phys. Chem. Chem. Phys.*, **2013**, 15, 466.
- [126] M. Xu, Y. Gao, Y. Wang, C. Woll, *Phys. Chem. Chem. Phys.*, **2010**, 12, 3649.
- [127] M. Xu, Y. Wang, S. Hu, R. Xu, Y. Cao, S. Yan, *Phys. Chem. Chem. Phys.*, **2014**, 16, 14682.
- [128] M. Arndt, S. Murali, T. Klüner, *Chem. Phys. Lett.*, **2013**, 556, 98.
- [129] D. C. Sorescu, J. T. Yates, *J. Phys. Chem. B*, **2002**, 106, 6184.
- [130] U. Wedig, M. Dolg, H. Stoll, H. Preuss, in: *Quantum Chemistry: The Challenge of Transition Metals and Coordination Chemistry*, A. Veillard, Reidel, *Dordrecht*, **1986**, p79.
- [131] J. P. Perdew, K. Burke, M. Ernzerhof, *Phys. Rev. Lett.*, **1997**, 78, 1396.
- [132] P. Deglmann, F. Furche, R. Ahlrichs, *Chem. Phys. Lett.*, **2002**, 362, 511.
- [133] W. C. Mackrodt, E. A. Simson, N. M. Harrison, *Surf. Sci.*, **1997**, 384, 192.
- [134] T. S. Bjørheim, A. Kuwabara, T. Norby, *J. Phys. Chem. C*, **2013**, 117, 5919.
- [135] A. Amtout, R. Leonelli, *Phys. Rev. B*, **1995**, 51, 6842.
- [136] S. C. Ammal, A. Heyden, *J. Chem. Phys.*, **2010**, 133, 164703.
- [137] S.-C. Li, P. Jacobson, S.-L. Zhao, X.-Q. Gong, U. Diebold, *J. Phys. Chem. C*, **2012**, 116, 1887.

- [138] S. Rahim Pouran, A. A. Abdul Raman, W. M. A. Wan Daud, *J. Clean. Prod.*, **2014**, 64, 24.
- [139] J. Kašpar, P. Fornasiero, N. Hickey, *Catal. Today*, **2003**, 77, 419.
- [140] K. Liu, A. Wang, T. Zhang, *ACS Catalysis*, **2012**, 2, 1165.
- [141] J. M. D. Coey, G. A. Sawatzky, *J. Phys. C: Solid State Phys.*, **1971**, 4, 2386.
- [142] E. Krén, P. Szabó, G. Konczos, *Phys. Lett.*, **1965**, 19, 103.
- [143] C. W. Searle, G. W. Dean, *Phys. Rev. B*, **1970**, 1, 4337.
- [144] L. M. Levinson, *Phys. Rev. B*, **1971**, 3, 3965.
- [145] L. M. Sandratskii, J. Kübler, *EPL (Europhysics Letters)*, **1996**, 33, 447.
- [146] F. Tran, P. Blaha, K. Schwarz, P. Novák, *Phys. Rev. B*, **2006**, 74, 155108.
- [147] M. Marsman, J. Paier, A. Stroppa, G. Kresse, *J. Phys.: Condens. Matter*, **2008**, 20, 064201.
- [148] A. Rohrbach, J. Hafner, G. Kresse, *Phys. Rev. B*, **2004**, 70,
- [149] G. Rollmann, A. Rohrbach, P. Entel, J. Hafner, *Phys. Rev. B*, **2004**, 69,
- [150] N. Dzade, A. Roldan, N. de Leeuw, *Minerals*, **2014**, 4, 89.
- [151] Z. D. Pozun, G. Henkelman, *J. Chem. Phys.*, **2011**, 134, 224706.
- [152] A. Rohrbach, J. Hafner, G. Kresse, *J. Phys.: Condens. Matter*, **2003**, 15, 979.
- [153] L. W. Finger, R. M. Hazen, *J. Appl. Phys.*, **1980**, 51, 5362.
- [154] A. Kiejna, T. Pabisiak, *J. Phys. Condens. Matter*, **2012**, 24, 095003.
- [155] M. Catti, G. Valerio, R. Dovesi, *Phys. Rev. B*, **1995**, 51, 7441.
- [156] L. M. Sandratskii, M. Uhl, J. Kübler, *J. Phys.: Condens. Matter*, **1996**, 8, 983.
- [157] P. Canepa, E. Schofield, A. V. Chadwick, M. Alfredsson, *Phys. Chem. Chem. Phys.*, **2011**, 13, 12826.
- [158] L. Pauling, S. B. Hendricks, *J. Am. Chem. Soc.*, **1925**, 47, 781.
- [159] T. P. Trainor, A. M. Chaka, P. J. Eng, M. Newville, G. A. Waychunas, J. G. Catalano, G. E. Brown Jr, *Surf. Sci.*, **2004**, 573, 204.
- [160] W. Bergermayer, H. Schweiger, E. Wimmer, *Phys. Rev. B*, **2004**, 69,
- [161] A. Kiejna, T. Pabisiak, *J. Phys. Chem. C*, **2013**, 117, 24339.
- [162] X. G. Wang, W. Weiss, S. K. Shaikhutdinov, M. Ritter, M. Petersen, F. Wagner, R. Schlögl, M. Scheffler, *Phys. Rev. Lett.*, **1998**, 81, 1038.



- [163] L. Maïke, M. Wolfgang, *J. Phys.: Condens. Matter*, **2009**, 21, 134010.
- [164] S. Thevuthasan, Y. J. Kim, S. I. Yi, S. A. Chambers, J. Morais, R. Denecke, C. S. Fadley, P. Liu, T. Kendelewicz, G. E. Brown Jr, *Surf. Sci.*, **1999**, 425, 276.
- [165] G. Marek, E. Andreas, H. Jürgen, *J. Phys.: Condens. Matter*, **2004**, 16, 1141.
- [166] K. Termentzidis, Adsorption of small molecules on metal surfaces, *Ph. D thesis*, **2007**, Universität Wien.
- [167] G. Blyholder, *J. Phys. Chem.*, **1964**, 68, 2772.
- [168] A. Föhlisch, M. Nyberg, P. Bennich, L. Triguero, J. Hasselström, O. Karis, L. G. M. Pettersson, A. Nilsson, *J. Chem. Phys.*, **2000**, 112, 1946.
- [169] G. Pacchioni, G. Cogliandro, P. S. Bagus, *Surf. Sci.*, **1991**, 255, 344.
- [170] J. Blomqvist, L. Lehman, P. Salo, *physica status solidi (b)*, **2012**, 249, 1046.
- [171] B. Meyer, D. Marx, *J. Phys.: Condens. Matter*, **2003**, 15, L89.
- [172] M. Kunat, F. Traeger, D. Silber, H. Qiu, Y. Wang, A. C. van Veen, C. Wöll, P. M. Kowalski, B. Meyer, C. Hättig, D. Marx, *J. Chem. Phys.*, **2009**, 130, 144703.
- [173] G. Pacchioni, A. M. Ferrari, P. S. Bagus, *Surf. Sci.*, **1996**, 350, 159.
- [174] F. Illas, S. Zurita, J. Rubio, A. M. Márquez, *Phys. Rev. B*, **1995**, 52, 12372.
- [175] M. S. Whittingham, *Chem. Rev.*, **2004**, 104, 4271.
- [176] M. Feng, A. Yang, X. Zuo, C. Vittoria, V. G. Harris, *J. Appl. Phys.*, **2010**, 107, 09A521.
- [177] J. Miralles, O. Castell, R. Caballol, J.-P. Malrieu, *Chem. Phys.*, **1993**, 172, 33.
- [178] J. Miralles, J.-P. Daudey, R. Caballol, *Chem. Phys. Lett.*, **1992**, 198, 555.
- [179] K. Andersson, P. Å. Malmqvist, B. O. Roos, *J. Chem. Phys.*, **1992**, 96, 1218.
- [180] K. Andersson, P. A. Malmqvist, B. O. Roos, A. J. Sadlej, K. Wolinski, *J. Phys. Chem.*, **1990**, 94, 5483.
- [181] F. Illas, I. P. R. Moreira, C. de Graaf, V. Barone, *Theor. Chem. Acc.*, **2000**, 104, 265.
- [182] I. d. P. R. Moreira, F. Illas, *Phys. Chem. Chem. Phys.*, **2006**, 8, 1645.
- [183] K. Fink, V. Staemmler, *Mol. Phys.*, **2013**, 111, 2594.
- [184] F. Illas, I. de P. R. Moreira, J. M. Bofill, M. Filatov, *Phys. Rev. B*, **2004**, 70,
- [185] F. Neese, *J. Phys. Chem. Solids*, **2004**, 65, 781.

- [186] L. Noodleman, *J. Chem. Phys.*, **1981**, 74, 5737.
- [187] T. Soda, Y. Kitagawa, T. Onishi, Y. Takano, Y. Shigeta, H. Nagao, Y. Yoshioka, K. Yamaguchi, *Chem. Phys. Lett.*, **2000**, 319, 223.
- [188] K. D. Vogiatzis, W. Klopper, A. Mavrandonakis, K. Fink, *Chem. Phys. Chem.*, **2011**, 12, 3307.
- [189] P. G. Bercoff, H. R. Bertorello, *J. Magn. Magn. Mater.*, **1997**, 169, 314.
- [190] M. Sultan, R. Singh, *Mater. Lett.*, **2009**, 63, 1764.
- [191] Z. Jiang, W. Zhang, W. Shangguan, X. Wu, Y. Teraoka, *J. Phys. Chem. C*, **2011**, 115, 13035.
- [192] K. Fink, C. Wang, V. Staemmler, *Int. J. Quantum. Chem.*, **1997**, 65, 633.
- [193] H. Fliegl, K. Fink, W. Klopper, C. E. Anson, A. K. Powell, R. Clerac, *Phys. Chem. Chem. Phys.*, **2009**, 11, 3900.
- [194] V. Meded, A. Bagrets, K. Fink, R. Chandrasekar, M. Ruben, F. Evers, A. Bernard-Mantel, J. S. Seldenthuis, A. Beukman, H. S. J. van der Zant, *Phys. Rev. B*, **2011**, 83, 245415.
- [195] J. B. Goodenough, K. S. Park, *J. Am. Chem. Soc.*, **2013**, 135, 1167.
- [196] T. J. Carter, R. Mohtadi, T. S. Arthur, F. Mizuno, R. Zhang, S. Shirai, J. W. Kampf, *Angew. Chem. Int. Edit.*, **2014**, 53, 3173.
- [197] Y. S. Meng, M. E. Arroyo-de Dompablo, *Energy Environ. Sci.*, **2009**, 2, 589.
- [198] S. Grimme, *J. Comput. Chem.*, **2006**, 27, 1787.
- [199] S. Grimme, J. Antony, S. Ehrlich, H. Krieg, *J. Chem. Phys.*, **2010**, 132, 154104.
- [200] N. J. Mosey, P. Liao, E. A. Carter, *J. Chem. Phys.*, **2008**, 129, 014103.
- [201] X. Wu, M. C. Vargas, S. Nayak, V. Lotrich, G. Scoles, *J. Chem. Phys.*, **2001**, 115, 8748.
- [202] T. Bučko, J. Hafner, S. Lebègue, J. G. Ángyán, *J. Phys. Chem. A*, **2010**, 114, 11814.
- [203] X. Zhang, C. Fan, Y. Wang, Y. Wang, Z. Liang, P. Han, *Comput. Mater. Sci.*, **2013**, 71, 135.
- [204] K. G. Keramidas, G. P. Voutsas, P. I. Rentzeperis, *Zeitschrift für Kristallographie*, **1993**, Part-1, 35.

- [205] S. M. Kauzlarich, J. L. Stanton, J. Faber, B. A. Averill, *J. Am. Chem. Soc.*, **1986**, 108, 7946.
- [206] G. Henkelman, A. Arnaldsson, H. Jónsson, *Comp. Mater. Sci.*, **2006**, 36, 354.
- [207] E. Sanville, S. D. Kenny, R. Smith, G. Henkelman, *J. Comput. Chem.*, **2007**, 28, 899.
- [208] W. Tang, E. Sanville, G. Henkelman, *J. Phys. Condens. Matter*, **2009**, 21, 084204.
- [209] A. Yamamoto, *Acta Crystallogr. Sec. B*, **1982**, 38, 1451.

## 8 COPYRIGHT PERMISSIONS

The Chapter 3 contains in part material that has already been published in peer-reviewed journal of *Topic in Catalysis*. The copyright permissions for published material are granted from **Springer Science+Business Media**.

Results, Table 3.1-3.3 and Figure 3.1-3.4 from Chapter 3 are reproduced in part with permissions from:

M. Buchholz, Q. Li, H. Noei, A. Nefedov, Y. Wang, M. Muhler, K. Fink, C. Wöll, The Interaction of Formic Acid with Zinc Oxide: A Combined Experimental and Theoretical Study on Single Crystal and Powder Samples, *Top. Catal.*, **2015**, 58 174. Copyright Springer Science+Business Media New York 2014.



## 9 ACKNOWLEDGEMENTS

Three years have gone so fast, and the time I have been in Karlsruhe is wonderful and unforgettable. First of all, I would like to sincerely thank my advisor, PD Dr. Karin Fink, for her guidance, advice and encouragement on both science and life, and for being the most patient person I know (it is not quoted from Adam).

I would like to thank for financial support from the Helmholtz Research School “Energy-related catalysis”. I also thank all the group members of “Energy-related catalysis” for sharing ideas and useful discussions, I benefit a lot from the summer schools, winter schools and soft skill courses that I attended.

I am grateful to be one member of Prof. Dr. Willem Klopper’s group. Many thanks to all former and present members, both from campus north and campus south, for many fruitful discussions and much fun (Kicker) time together.

I would also like to thank all my collaborators, Prof. Dr. Christof Wöll, Dr. Maria Buchholz and Chengwu Yang from IFG, Dr. Robert Kruk and Dr. Subho Dasgupta from INT, for bringing so many interesting scientific topics, parts of which are presented in this thesis. Special thanks goes to Dr. Xiangyu Zhao for not only being a collaborator, also being a good teacher, a close friend.

Most of the VASP calculations were done on the computational resource HC3 cluster and bwUniCluster funded by the Ministry of Science, Research and Arts and the Universities of the State of Baden-Württemberg, Germany. Furthermore, I am thankful to Dr. Peter Thissen for providing some computation time from Texas Advanced Computing Center (TACC).

This thesis is dedicated to the memory of my grandfather, who always had faith in me,

and I miss him dearly. I give thanks to my parents for their care and encouragement. Finally, I thank my wife for her love and support. Without her patience and sacrifice, I could not have completed this thesis.

## List of Publications

1. Maria Buchholz, **Qiang Li**, Heshmat Noei, Alexei Nefedov, Yuemin Wang, Martin Muhler, Karin Fink and Christof Woell, The Interaction of Formic Acid with Zinc Oxide: A Combined Experimental and Theoretical Study on Single Crystal and Powder Samples, *Top Catal*, 2015, 58, 174–183
2. Xiangyu Zhao, **Qiang Li**, Zhirong Zhao-Karger, Ping Gao, Karin Fink, Xiaodong Shen and Maximilian Fichtner, *ACS Appl. Mater. Interfaces*, 2014, 6 (14), 10997–11000
3. Xiangyu Zhao, **Qiang Li**, Tingting Yu, Meng Yang, Karin Fink, and Xiaodong Shen, Carbon incorporation effects and reaction mechanism of FeOCl cathode materials for chloride ion batteries, submitted
4. Zhigang Gu, Lars Heinke, Christof Wöll, Tobias Neumann, Wolfgang Wenzel, **Qiang Li**, Karin Fink, Ovidiu D. Gordan, and Dietrich R.T. Zahn, Experimental and Theoretical Investigations of the Electronic Band Structure of Metal-Organic Frameworks of HKUST-1 Type, submitted
5. Subho Dasgupta, Bijoy Das, Tessy Theres Baby, **Qiang Li**, Karin Fink, Sylvio Indris, Michael Knapp, Helmut Ehrenberg, Robert Kruk, Horst Hahn, Towards on-and-off magnetism: reversible electrochemistry to control magnetic transition in spinel ferrites, submitted
6. **Qiang Li**, Yi-Xiang Qiu, Xian-Yang Chen, W.H.Eugen Schwarz and Shu-Guang Wang, Investigation of Spin-Flip Reactions of Nb + CH<sub>3</sub>CN by Relativistic Density Functional Theory, *Phys. Chem. Chem. Phys.* 2012, 14, 6833-6841
7. **Qiang Li**, Xian-Yang Chen, Yi-Xiang Qiu, and Shu-Guang Wang, Investigation of Spin-Flip Reactions of Zr + CH<sub>3</sub>CN by Relativistic Density Functional Theory, *J. Phys. Chem. A.* 2012, 116, 5019–5025
8. Yu-He Kan, **Qiang Li**, DFT Studies on the Structure and Electronic Spectra of C(62) and Its Pyridinyl Derivatives, *Chemical Journal of Chinese Universities-Chinese*, 2009, 30, 174-177
9. Yu-He Kan, **Qiang Li**, Theoretical Investigation on Electronic Spectra of Fullerene Polypyridyl Ruthenium(II) Complexes by Density Functional Theory, *Acta Chimica Sinica*, 2008, 66, 2585-2591